TU Graz

Dipl.-Ing. Martin Kleindienst, BSc

Control Concepts for Silicon Wafer Stripping and Cleaning Equipment

DOCTORAL THESIS

to achieve the university degree of
Doktor der Technischen Wissenschaften

submitted to

Graz University of Technology

Supervisor
Univ.-Prof. Dipl.-Ing. Dr.techn. Martin Horn

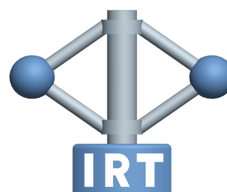

Institute of Automation and Control

Graz, April 2019

AFFIDAVIT

I declare that I have authored this thesis independently, that I have not used other than the declared sources/resources, and that I have explicitly indicated all material which has been quoted either literally or by content from the sources used. The text document uploaded to TUGRAZonline is identical to the present doctoral thesis.

Graz, ______________________________ ____________________________________

Date Signature

TO MY LATE MOTHER

Foreword

The present work was created in cooperation with the company Lam Research AG. In this context, I would like to thank in particular Dipl.-Ing. Dr.techn. Felix Staudegger, who was able to inspire me for the tasks in the company and who supported me during my dissertation on the part of the company.

Especially I would like to thank Ass.Prof. Dipl.-Ing. Dr.techn. Markus Reichhartinger, who supported me as project manager for the whole duration of the project. Above all, his ideas and suggestions for improvement have contributed significantly to the success of the work. Furthermore, my special thanks go to my supervisor Univ.-Prof. Dipl.-Ing. Dr.techn. Martin Horn. Through goal-oriented discussions and ongoing support, he accompanied and supported me during all phases of my dissertation. Furthermore, I thank Prof. Dr.-Ing. Frank Allgöwer for the review of my work.

I am very grateful to all colleagues at the Institute of Automation and Control at Graz University of Technology for the technical discussions and the constructive and pleasant cooperation. I also thank my company colleagues for the good cooperation and the great working atmosphere, as well as the friendships that have been made.

Finally, my thanks go to my entire family, who have always accompanied me. Especially I would like to thank my wife Anita, as well as our children Niklas and Elias for their support and their love.

Abstract

Shrinking geometries at integrated circuits require a higher precision and an increased flexibility of silicon wafer fabrication equipment. In this work, novel control concepts for so-called spin wet clean tools are proposed. The work was carried out in cooperation with Lam Research AG, who also provided the laboratory equipment to perform the experimental investigations.

The first part of the thesis discusses a specific approach for semiconductor rapid thermal processing (RTP), where silicon wafers are heated to desired temperatures. Here, the key issue is to ensure uniform wafer temperature profiles. This guarantees that the manufactured integrated circuits, which are spread over the entire wafer, can be processed equally. In this thesis, a mathematical model capturing the dynamic behavior of the heating-up process is presented. It relies mainly on the well-known partial differential heat equation, governing the temperature distribution in a given region of a given material. Based on this, different observer types as also control laws are proposed, which in combination turned out to be superior to conventional RTP strategies.

The second part of the thesis deals with the design of a novel chemistry supply system to treat the surface of the rotating wafer with well-defined chemical solutions. In contrast to state of the art supply systems, which are using large tanks in combination with a recirculation system, the novel approach allows mixing a solution of defined ratio and temperature online. An approach to control the corresponding flow rates is presented and an overlain controller is designed to adjust the temperature of the mixture.

The proposed approaches are implemented and validated using laboratory setups.

Contents

Abstract ix

1 Introduction 1
1.1 Functionality of a single-wafer spin clean tool 1
1.2 State of the art photoresist removal process 5
1.3 Novel photoresist stripping process using ozone gas 5
1.4 Post-clean step with SC-1/SC-2 6
1.5 Structure of the thesis and scope of work 6
1.6 Contribution of the thesis 7

2 Observer-based temperature control of an LED heated wafer 9
2.1 Plant description and problem formulation 9
2.2 Plant model 9
2.2.1 Heat transfer equation 10
2.2.2 Spatial discretization - vertical method of lines 12
2.2.3 Boundary conditions 14
2.2.4 Heat input due to light absorption 15
2.2.5 Heat losses 19
2.2.6 State space representation 19
2.2.7 Plant model validation 23
2.3 Wafer sensitivity 26
2.4 Observer design based on classical approaches 27
2.4.1 Additional estimate for the total emissivity 28
2.4.2 Observability check 29
2.4.3 Linearization around the estimated state vector 30
2.4.4 System discretization 31
2.4.5 Luenberger observer design based on LQR approach 32
2.4.6 Numerical simulation 34
2.4.7 Laboratory experiments 34
2.4.8 Comparison with Kalman filter 36
2.4.8.1 Covariance matrix of the process noise 40
2.4.8.2 Variance of the measurement noise 42
2.4.8.3 Initial covariance matrix of the a priori estimation error 43
2.4.8.4 Laboratory experiments 43

2.5 Observers based on the late-lumping approach . . . 45
2.5.1 Late-lumping approach . . . 46
2.5.1.1 Proof of convergence . . . 47
2.5.2 Late-lumping approach with measurement injection . . . 51
2.5.2.1 Remarks on the stability . . . 52
2.5.3 Extension to estimate the wafer's total emissivity . . . 53
2.5.3.1 Estimation of Δ_{max} and choice of η_{i_ζ} . . . 54
2.5.4 Laboratory experiment . . . 55
2.5.5 Conclusion . . . 57
2.6 Controller design . . . 58
2.6.1 PI state feedback controller . . . 60
2.6.1.1 Prevention of controller windup . . . 65
2.6.2 Extended observer-based control approach . . . 68
2.6.2.1 Numerical simulation and laboratory experiments . . . 72
2.7 Conclusion . . . 77

3 Post-clean step - design of a point of use mixing system 79
3.1 Problem formulation . . . 79
3.2 Plant description and mathematical model . . . 81
3.2.1 Blending of constituents . . . 81
3.2.2 Liquid flow controller . . . 83
3.2.3 Temperature sensor dynamics . . . 88
3.2.4 Transport delay . . . 89
3.3 Temperature control . . . 89
3.4 Laboratory experiment and conclusion . . . 92

4 Summary and outlook 95

A Heat transfer equation 98

B Circle-circle intersection 99

C Derivative of a matrix-vector-product by a vector 100

D Taylor series expansion 103

E Standard deviation of a uniformly distributed random variable 106

F Eigenvalues of linear differential operators 108

G Controllability inheritance for PI state feedback controller 117

Bibliography 119

List of Figures

1.1 Wafer fabrication process steps 2
1.2 EOS 3
1.3 Chemistry supply system 4
1.4 Photo resist stripping with ozone gas 6

2.1 Schematic representation of the hardware setup 10
2.2 Rotational symmetry 12
2.3 Equidistant spatial grid 12
2.4 Improved grid 14
2.5 Radiation characteristics of an LED 16
2.6 Annuli division 17
2.7 Light absorption 18
2.8 Heating plate 21
2.9 Temperature sensors 23
2.10 Input signals 24
2.11 Plant model validation 25
2.12 Wafer sensitivity 26
2.13 Total emissivity and light absorption 27
2.14 Relationship between total emissivity and standard deviation 28
2.15 Numerical observability check 30
2.16 Simulated and estimated zone temperatures 35
2.17 Estimation error 35
2.18 Emissivity estimate 36
2.19 Measured and estimated output, “highly doped” wafer 37
2.20 Estimated emissivity, “highly doped” wafer 37
2.21 Input noise due to digital to analogue converter 41
2.22 Gaussian distribution, D/A converter 42
2.23 Measured and estimated output, “highly doped” wafer, Kalman filter . . 44
2.24 Estimated emissivity, “highly doped” wafer, Kalman filter 44
2.25 Measured and estimated zone temperatures 56
2.26 Estimated emissivity, “highly doped” wafer, late-lumping observer 56
2.27 Estimation error 57
2.28 PI state feedback controller 61
2.29 Simulated heat-up of a “highly doped” wafer 64

2.30 Simulated heat-up of a “highly doped” wafer 66
2.31 PI state feedback controller 67
2.32 Simulated heat-up of a “highly doped” wafer 69
2.33 Simulated heat-up of a “highly doped” wafer 73
2.34 Simulated heat-up of a “bare silicon” wafer 74
2.35 Heat-up experiment with a “highly doped” wafer 75
2.36 Heat-up experiment with a “bare silicon” wafer 76

3.1 Schematic representation of the point of use mixing system 80
3.2 Hardware setup of an LFC 80
3.3 Lookup tables of constituent LFC measured at two different main stream conditions 84
3.4 LFC simulation with improper lookup table 84
3.5 Fuzzy-PI controller 85
3.6 Fuzzification 86
3.7 Point of use mixing system with LFCs based on a Fuzzy-PI controller . . 87
3.8 Mathematical model of temperature sensor 89
3.9 Dead time schematic 90
3.10 Overall plant model with inversion of mixing formula 90
3.11 Constituent LFC 91
3.12 Hardware design of the point of use mixing system 92
3.13 Point of use mixing including temperature control 93

B.1 Circle-circle intersection 99

E.1 Uniform distribution 107

F.1 Modified Bessel functions of the first and second kind 110
F.2 Bessel functions of the first and second kind 111
F.3 Eigenvalue calculation of the operator $\mathcal{A}_1$ using the MATLAB® function `bvp4c`, numerical solution 113
F.4 Eigenvalue calculation of the operator $\mathcal{A}_2$ using the MATLAB® function `bvp4c`, numerical solution 116

1 Introduction

Although Moore's law, stating that the number of transistors on an integrated circuit doubles approximately every two years, seems to start stuttering [Williams, 2017], the demands for the semiconductor industry are still increasing rapidly. This can be attributed to a great extent to the revolution on the consumer electronics market as well as the progresses in the field of electromobility within the last couple of years. The corresponding new technologies require high-tech innovations in particular to provide secure and power-efficient applications. To account for the increasingly complex devices and shrinking dimensions, the suppliers of silicon wafer fabrication equipment are required to provide innovative products.

During the fabrication of a wafer, various process steps like film deposition, lithography, plasma etch, photoresist strip and wafer cleaning are repeated multiple times. This is illustrated in Figure 1.1. For the stripping of photoresist as well as for removing residues and chemical impurities from the wafer, so-called "spin wet clean" products are commonly used. In the course of this thesis, the development of model-based control schemes for such systems is under investigation.

1.1 Functionality of a single-wafer spin clean tool

Before the early 1990s, backside layers on the wafer had to be etched off by using so-called "wet benches". Therein the whole cassette of wafers was put into a chemical bath. In order to protect the front side of the wafer, it was coated either by hard-baked photoresists or plastic foils, which had to be removed later on. To overcome this tedious procedure, the first single-wafer spin clean tool was launched around 1990. This so-called "spin etcher" was able to treat the backside of the wafer without etching its topside containing the devices. The idea behind a spin clean tool was to rotate the wafer upside down. The chemical was dispensed onto the wafer and spun off.

Through the years, the field of application for single-wafer spin tools has been expanded significantly. Nowadays, wafer cleaning and stripping of photoresists with various chemicals belong to the most frequently operated processes during the fabrication of an integrated circuit. Every fourth to fifth process step belongs to these categories. The requirements for cleaning and stripping processes are increasing continuously due to new materials,

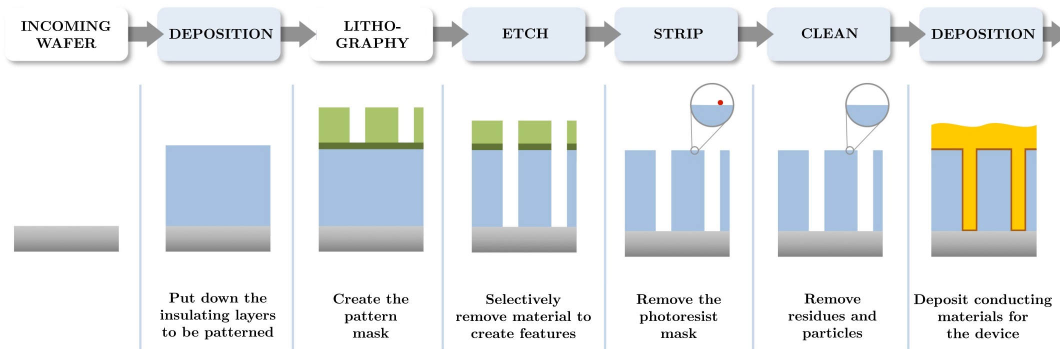

Figure 1.1: Wafer fabrication process steps [Lam Research Corporation, 2017]: The mostly operated process steps belong to the key areas deposition, lithography, etch, strip and clean. This example shows how a conducting path is created. Firstly, a deposition process can be used to produce a thin film of an insulating material on the wafer. With the help of the lithography it is possible to create a desired pattern mask by resist coating, exposure and development. The unprotected areas of the insulating layer can then be etched off. In a next step, the remaining photoresist is stripped and the wafer is cleaned to remove residues. With the help of a second deposition process, the created trenches can be filled with a conducting material.

smaller structures on the wafer and lower defect requirements. This forces newly launched applications to ensure a precise control of physical process parameters like flow rates, temperatures and so forth.

For cleaning applications, the so-called RCA[1] (Radio Corporation of America) standard defines solutions to remove particles and impurities on the wafer. More precisely, SC-1 (Standard Clean One), which is a mixture of deionized water, ammonium hydroxide (NH_4OH) and hydrogen peroxide (H_2O_2) is applied to slightly etch the silicon surface to undercut particles in order to lift them off. A solution composed out of deionized water, hydrochloric acid (HCl) and hydrogen peroxide (referred to as SC-2) is widely used to oxidize and remove metals. For the stripping of photoresist, usually mixtures containing sulfuric acid (H_2SO_4) are utilized to break the carbon network in resist polymers. Solutions containing hydrofluoric acid (HF) are often used to remove etch polymers by dissolution and undercut. In summary, a variety of chemicals has been established in the past to remove unwanted substances from the wafer.

One of the latest "spin wet clean" products available on the market is depicted in Figure 1.2. The chemistry supply together with the process modules form the core of the spin clean tool. To supply the process modules with desired liquids, a tank-based

[1] Kern, 1990.

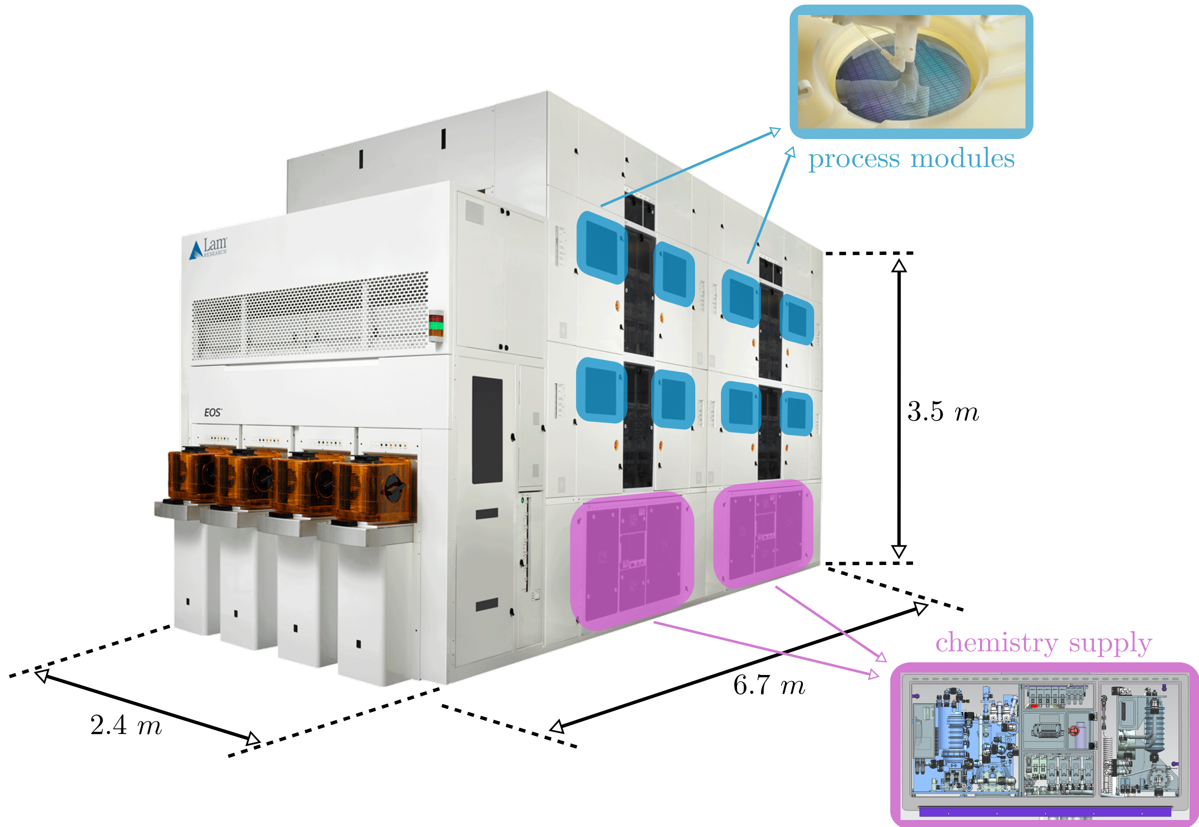

Figure 1.2: Lam EOS [Lam Research Corporation, 2017]: The latest Lam wet clean product, called EOS, can be configured with either 8 or 16 process chambers/modules. Within these chambers, the wafer is processed by either using reactive gasses or by treating its surface with liquid chemicals.
For the treatment with gasses, the wafer is usually heated to temperatures above 300 $°C$ (573.15 K). This work proposes a novel approach in order to control the temperature of the wafer's surface. For so-called "wet clean steps", the internal fluid delivery system provides the process modules with the liquid chemicals at a desired temperature and flow rate. The current configuration is based on using several large tanks together with a recirculation system to prepare the needed chemicals. Novel concepts proposed in this work allow mixing the requested chemical online without needing tanks and a recirculation system. This saves space and increases the flexibility of the equipment since process parameters like flow rate, mixing ratio and temperature can be adjusted easily.

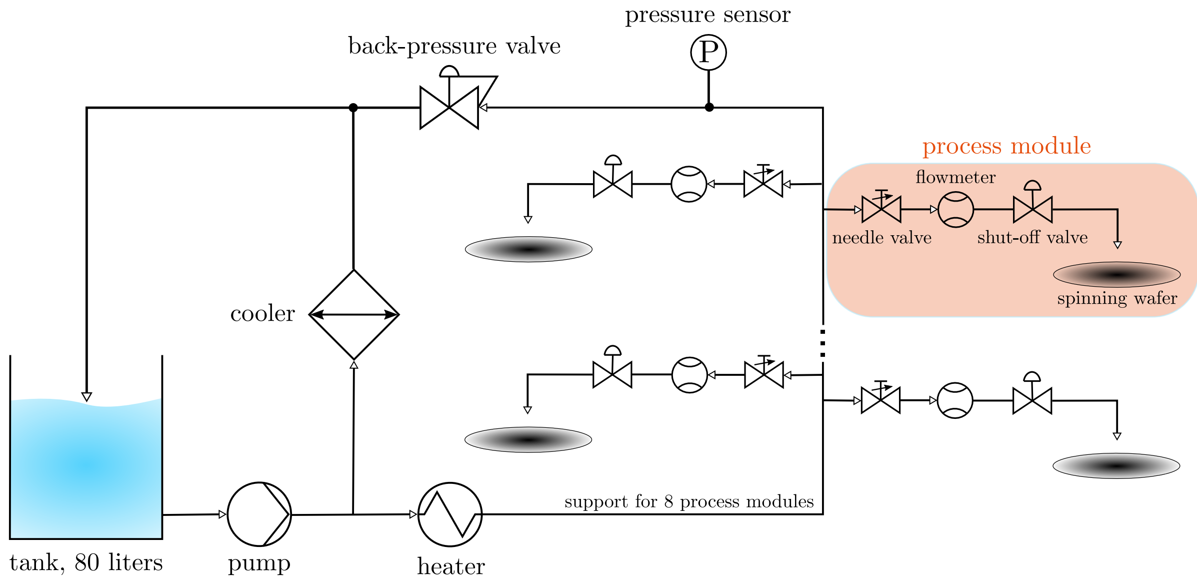

Figure 1.3: Chemistry supply system: The tank-based state of the art fluid delivery system recirculates the chemical with the help of a centrifugal pump. A heater and a cooler are used to set up a desired temperature. The pressure in the recirculation line is adjusted by means of a back-pressure valve in combination with a pressure sensor.

recirculation system is used. As the schematic representation of the state of the art supply system shown in Figure 1.3 points out, the pre-mixed chemical is filled into a tank and permanently circulated with the help of a centrifugal pump. The rotational speed of the pump is set manually in order to achieve a desired, almost constant flow rate through the recirculation system. To set up a required temperature of the mixture in the range of 20 to 130 $°C$ (293.15 to 403.15 K), a PI controller is used to adjust the power of the heater. A cooler in a bypass line can be utilized in case low temperatures are requested. The pressure sensor in combination with the pneumatically actuated back-pressure valve is used to control the pressure at the measuring point. For this, a PI controller is implemented again. Due to the large cross section of the recirculation line in relation to the used flow rates, the pressure can be kept almost constant at the branch connections to the process modules. Finally, the flow rate to the wafer is set manually with the help of a needle valve by adjusting its aperture. A flowmeter, measuring the actual flow rate, serves as a monitoring device. The shut-off valve is used to start and stop the liquid flow to the wafer.

This chemistry supply concept has proven itself for the last couple of years. Due to the permanent recirculation, it is easy to control, reliable and shows a good wafer to wafer repeatability. It also has some disadvantages which become more and more significant as the demanded flexibility for the processes rises. For example, with the state of the art system it is not possible to quickly change the mixing ratio of the solution, which

is one of the three main process parameters. Also its temperature and the flow rate of the chemical to the wafer may change more dynamically than in the past. For that either the tank has to be refilled, the temperature of the mixture has to be changed via a long-lasting period of time, or the needle valve has to be readjusted manually. Of course, this procedures are associated with a great effort and costly downtime of the tool. This turns out to be a problem for novel processes, which already request to change the process parameters online, i.e. during the process of one single wafer.

1.2 State of the art photoresist removal process

One critical application of a spin clean tool is the removal of hard-baked photoresist films after ion implantation. This is usually carried out with solutions containing sulfuric acid (H_2SO_4). They are dispensed onto the wafer by means of a chemistry supply described in Section 1.1. A widely used mixture, referred to as "sulfuric peroxide mixture", is composed of sulfuric acid (H_2SO_4) and hydrogen peroxide (H_2O_2) in a ratio of usually ranging from 2:1 to 4:1 at temperatures of 100 to 130 $°C$ [Reinhardt and Kern, 2008; Philit et al., 2003]. The hydrogen peroxide is often replaced by ozone. This chemical is then called "sulfuric ozone mixture". The process step with solutions containing sulfuric acid is mostly followed by a treatment with SC-1 or diluted hydrofluoric acid.

The extensive usage of sulfuric acid for wafer manufacturing has become subject of criticism in recent years. In particular, its harm to the environment is significant. Some governments, especially those located in Asia, already limit the quantity of sulfuric acid for companies. Therefore, novel processes with different chemicals to remove hard-baked photoresist are sought pressingly [Patil et al., 2017].

1.3 Novel photoresist stripping process using ozone gas

A novel process to remove hard-baked photoresist without using solutions containing sulfuric acid was developed recently. Instead of using liquid chemicals, the wafer is flushed with ozone gas within an environmental controlled chamber. The ozone gas O_3 splits into O_2 and oxygen radicals O above the wafer. These radicals then strip the photoresist on the wafer surface in order to lift it off. To achieve desired process results, the wafer has to be heated uniformly to temperatures above 300 $°C$ (573.15 K). Figure 1.4 schematically illustrates the stripping process. The main advantages of using ozone lie in its easy production with an ozone generator, and its environmental friendliness. Excessive ozone, which is not dissipated within the chamber, can be easily converted into O_2 by applying heat in a so-called "ozone destructor".

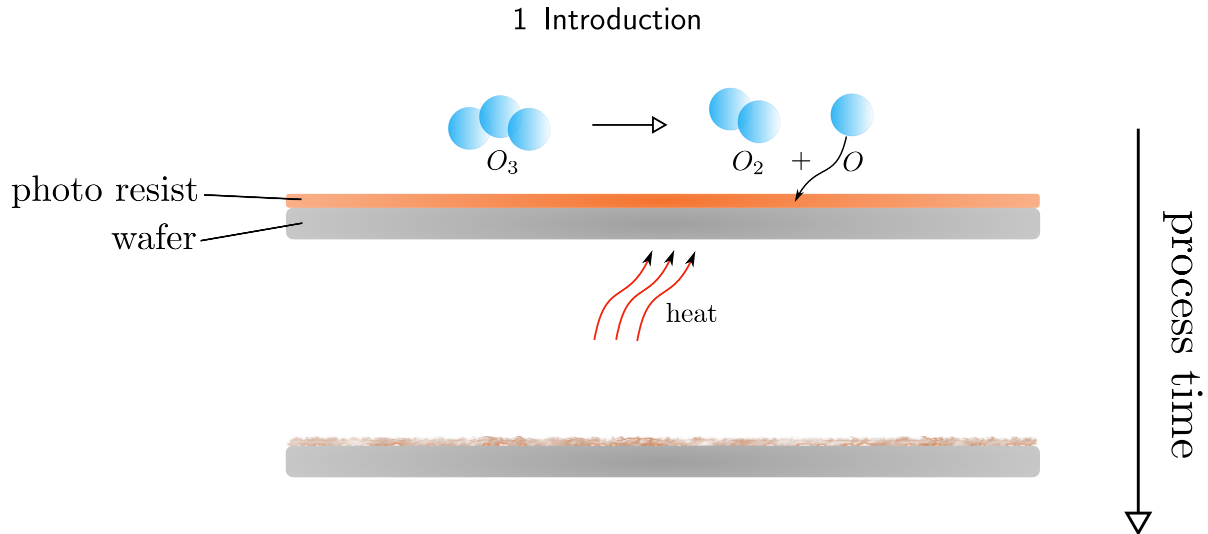

Figure 1.4: Photo resist stripping with ozone gas: The heated wafer is flushed with ozone gas in order to remove hard-baked photo resist.

1.4 Post-clean step with SC-1/SC-2

In order to remove remaining photoresist particles, the stripping process is followed by a wet clean step using SC-1 or SC-2. Instead of using the state of the art chemistry supply system outlined in Section 1.1, a novel so-called "point of use" (POU) blending system is intended to be used. In contrast to a tank-based recirculation system, a POU blending system is capable of mixing a solution with a well defined temperature composed of deionized water, hydrogen peroxide, ammonium hydroxide and/or hydrochloric acid online in a defined ratio. As this system mixes the chemical online, its composition can be varied from wafer to wafer or even during one process step.

1.5 Structure of the thesis and scope of work

This thesis is divided into two main parts.

The first part deals with the heating process of the wafer within the environmental controlled chamber. A mathematical model capturing the dynamical behavior of the heat-up process is derived. Based on that, different observer types to estimate the wafer's temperature profile are designed and evaluated. Control laws are proposed, which in combination with the observer can be used to set up desired temperature profiles on the wafer's surface. The approaches are validated at a real world heating system with different wafer types.

The second chapter deals with the design of the POU mixing system. Mathematical models are derived and used to design control approaches to adjust the involved process

parameters, which are flow rates, temperature and mixing ratio of the solution. The theoretical results are reinforced with the help of experiments at laboratory tools.

1.6 Contribution of the thesis

The temperature control of silicon wafers, which is often referred to as "rapid thermal processing", is widely used in semiconductor industries [J. Y. Choi, Do, and H. S. Choi, 2003; Ching-An and Yaw-Kuen, 2001; Lin and Chu, 2001]. In the majority of the cases, the wafer is heated up to desired temperatures to activate dopants or to repair damages after ion implantation. Among these areas of use, the heating of the wafer still opens a wide range of applications within the field of chip manufacturing.

To achieve desired process results, it is essential to set up uniform temperature profiles on the wafer's surface. Proposed algorithms to control the wafer's temperature assume the temperature profile to be known [Ebert et al., 2004]. In fact, measuring the latter without contacting the wafer is still a problem in semiconductor industries. Devices based on the principle of pyrometry are available to measure the temperature at one single point on the wafer's surface. Some approaches use multiple sensors to get an estimate of the wafer's temperature profile. The main drawback of this approach is the limited space in the process chamber and the restricted resolution of the obtained temperature profile. Other techniques combine the measurement of the wafer reflectivity and the use of infrared cameras to obtain the wafer's temperature profile [Maxwell, Yan, and Howell, 2007]. Again, this approach suffers from the integration of the camera in the process chamber.

The novel approach presented in this thesis is based on measuring the temperature at one single point of the wafer and estimating the remaining temperature profile by using a state observer. A detailed mathematical model, which allows to design model-based estimators and controllers for the considered systems, is presented for the first time. It relies mainly on the well-known heat equation. By discretizing this partial differential equation in space, a set of nonlinear ordinary differential equations can be obtained. Apart from applying different observer approaches to this high-order finite-dimensional system, estimator schemes designed directly for the partial differential equation are discussed. A recently published approach [Schaum, Moreno, Alvarez, and Meurer, 2015] is extended in such a manner that the observer dynamics can be improved significantly by introducing a so-called measurement injection.

Based on the estimated wafer's temperature profile, different control strategies are proposed for setting up desired wafer temperatures in order to enable the novel photoresist stripping process outlined in Section 1.3.

In order to remove residual impurities from the wafer after this photoresist stripping process, a novel mixing system for post-clean applications is proposed. This system allows to control the mixing ratio, the outlet flow rates and the temperature of the solution. Such a system entails a significant increase in flexibility compared to state of the art tank-based chemistry supply systems.

2 Observer-based temperature control of an LED heated wafer

To enable the outlined photoresist stripping process using ozone gas, the wafer has to be heated up to temperatures in the range of 300 to 400 $°C$ (573.15 to 673.15 K). The wafer heat-up process is carried out with the help of a large number of high-power LEDs. In the following, the hardware setup is described. Subsequently, a mathematical model is derived, which is then used to design different observer types and control laws.

2.1 Plant description and problem formulation

The hardware setup (see Figure 2.1) considered in this section consists of a heating plate, a rotating chuck carrying the wafer and a pyrometer to measure the wafer's temperature at one single position. The heating plate is equipped with more than 1000 high-power LEDs, each emitting blue light with a wavelength of approximately 450 nm. Due to the high spectral absorptivity and a transmissivity close to zero of silicon at this wavelength, a setup of this kind is particularly suitable for heating. The wafer with a radius of R = 150 mm rotates above the heating plate with an angular velocity of approximately 10 revolutions per minute. The closed process chamber is continuously flushed with ozone gas to treat the surface of the silicon wafer. A pyrometer is integrated in the heating plate and measures the temperature of the wafer at a distance of 40 mm from the wafer center.

Based on a plant model, a state observer is designed to estimate the wafer's temperature profile by taking into account the input power to the LEDs as well as the temperature measured by the pyrometer. The estimated temperature profile is finally used as a feedback for a control law to set up desired wafer temperatures.

2.2 Plant model

The wafer heating process mainly relies on three physical effects: the heat transfer within the wafer, the heat input caused by absorption of the emitted light and heat losses due

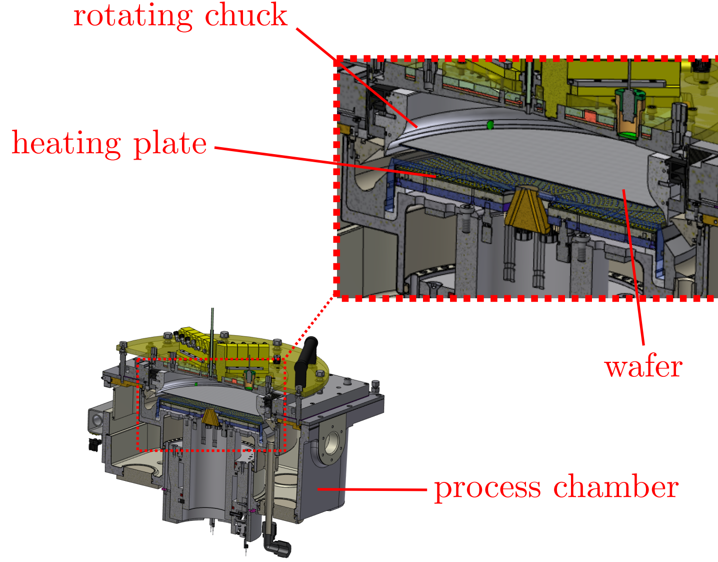

Figure 2.1: Schematic representation of the hardware setup: The wafer is rotating above the heating plate, which is equipped with a large number of high-power LEDs. A pyrometer is measuring the temperature at one point of the wafer from the bottom side through an aperture in the heating plate. The closed chamber is flushed with ozone gas through multiple nozzles in the top lid.

to convection and radiation. The partial differential heat equation is studied as a means of describing the heat transfer in the wafer. Semi-discretization techniques are applied to derive a set of ordinary differential equations. Based on the obtained equations, the heat input and the heat losses can be included in the model by considering geometric properties of the system.

2.2.1 Heat transfer equation

The heat transfer equation with heat sources and losses reads as [Baehr and Stephan, 2011]

$$\rho c_p(T)\frac{\partial T(\boldsymbol{\xi},t)}{\partial t} = \text{div}\left\{\lambda_c(T)\text{grad}\left[T(\boldsymbol{\xi},t)\right]\right\} + q(\boldsymbol{\xi},t), \tag{2.1}$$

where the vector $\boldsymbol{\xi}$ is the three-dimensional space coordinate and $T(\boldsymbol{\xi},t)$ is the wafer's temperature given in Kelvin as a function of $\boldsymbol{\xi}$ and time t. The temperature-dependent coefficient $\lambda_c(T)$ denotes the heat conductivity, $c_p(T)$ the heat capacity and ρ the density[1]

[1] The density of silicon can be treated as constant within the considered temperature range of 0 to 400 $°C$ (273.15 to 673.15 K).

of the silicon wafer. Volumetric heat sources and losses are denoted by $q(\boldsymbol{\xi}, t)$. With[2]

$$\begin{aligned} &\operatorname{div}\{\lambda_c(T)\operatorname{grad}[T(\boldsymbol{\xi},t)]\} = \\ &\quad \lambda_c(T)\operatorname{div}\{\operatorname{grad}[T(\boldsymbol{\xi},t)]\} + \frac{\partial \lambda_c(T)}{\partial T(\boldsymbol{\xi},t)} \|\operatorname{grad}[T(\boldsymbol{\xi},t)]\|_2^2 \end{aligned} \tag{2.2}$$

and assuming that $\lambda_c(T)$ changes slowly with temperature, i.e.

$$\frac{\partial \lambda_c(T)}{\partial T(\boldsymbol{\xi},t)} \approx 0, \tag{2.3}$$

equation (2.1) reduces to

$$\frac{\partial T(\boldsymbol{\xi},t)}{\partial t} = \kappa(T)\operatorname{div}\{\operatorname{grad}[T(\boldsymbol{\xi},t)]\} + \frac{q(\boldsymbol{\xi},t)}{\rho c_p(T)}, \tag{2.4}$$

where

$$\kappa(T) = \frac{\lambda_c(T)}{\rho c_p(T)}. \tag{2.5}$$

Rewriting (2.4) in cylindrical coordinates, i.e. the radial distance r, the angular coordinate φ and the height z, leads to

$$\begin{aligned} \frac{\partial T(r,\varphi,z,t)}{\partial t} = \kappa(T)\Bigg[&\frac{\partial^2 T(r,\varphi,z,t)}{\partial r^2} + \frac{1}{r}\frac{\partial T(r,\varphi,z,t)}{\partial r} \\ &+\frac{1}{r^2}\frac{\partial^2 T(r,\varphi,z,t)}{\partial \varphi^2} + \frac{\partial^2 T(r,\varphi,z,t)}{\partial z^2}\Bigg] + \frac{q(r,\varphi,z,t)}{\rho c_p(T)}. \end{aligned} \tag{2.6}$$

Due to the fact that the system is rotationally symmetrical (see Figure 2.2), i.e.

$$\frac{\partial T(r,\varphi,z,t)}{\partial \varphi} = 0 \tag{2.7}$$

and the temperature distribution in z direction is uniform[3], i.e.

$$\frac{\partial T(r,\varphi,z,t)}{\partial z} = 0, \tag{2.8}$$

equation (2.6) reduces to the one-dimensional heat equation

$$\frac{\partial T(r,t)}{\partial t} = \kappa(T)\left[\frac{\partial^2 T(r,t)}{\partial r^2} + \frac{1}{r}\frac{\partial T(r,t)}{\partial r}\right] + \frac{q(r,t)}{\rho c_p(T)}. \tag{2.9}$$

[2] $\|\operatorname{grad}[T(\boldsymbol{\xi},t)]\|_2^2$ denotes the scalar product of $\operatorname{grad}[T(\boldsymbol{\xi},t)]$ with itself (see Appendix A).

[3] The temperature distribution in z direction can be treated as uniform since the thickness of the wafer is up to a thousand times smaller than its diameter.

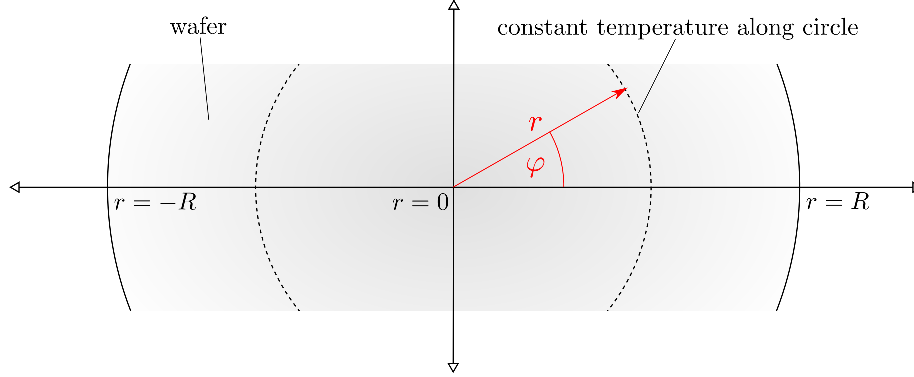

Figure 2.2: Rotational symmetry: The temperature along a circle is assumed to be constant.

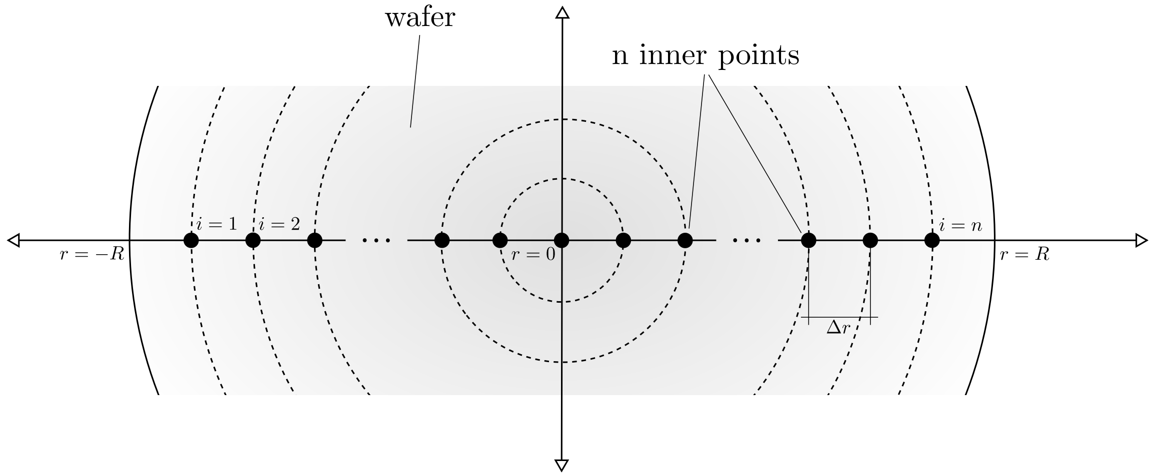

Figure 2.3: Equidistant spatial grid: The wafer diameter is divided into $n + 1$ equidistant intervals. If n is chosen odd, an inner point is located directly in the origin, which leads to a division by zero in the mathematical model.

2.2.2 Spatial discretization - vertical method of lines

The so-called vertical method of lines [Schiesser and Griffiths, 2009] is applied to (2.9) in order to approximate the spatial derivatives by difference equations, i.e. a set of ordinary differential equations can be derived out of the partial differential equation. The wafer diameter is thus divided into $n+1$ equally spaced distances, see Figure 2.3. The resulting equidistant spatial grid with n inner points reads as

$$\Omega_{\Delta 1} = \{r_i : r_i = -R + i\Delta r;\ i = 1,\ \ldots\ n\}\,, \tag{2.10}$$

where the distance between two points is computed as

$$\Delta r = \frac{2R}{n+1}. \tag{2.11}$$

To replace the spatial derivatives in (2.9) by algebraic approximations, Taylor series of $T(r+\Delta r,t)$ and $T(r-\Delta r,t)$ are expanded at r which leads to

$$T(r+\Delta r,t) = T(r,t) + \frac{\partial T(r,t)}{\partial r}\Delta r + \frac{1}{2}\frac{\partial^2 T(r,t)}{\partial r^2}(\Delta r)^2 + \dots \tag{2.12}$$

and

$$T(r-\Delta r,t) = T(r,t) - \frac{\partial T(r,t)}{\partial r}\Delta r + \frac{1}{2}\frac{\partial^2 T(r,t)}{\partial r^2}(\Delta r)^2 + \dots\ . \tag{2.13}$$

Neglecting higher-order terms and subtracting (2.13) from (2.12) yields an approximation for the first derivative of $T(r,t)$ with respect to r, i.e.

$$\frac{\partial T(r,t)}{\partial r} \approx \frac{T(r+\Delta r,t) - T(r-\Delta r,t)}{2\Delta r}. \tag{2.14}$$

Summing up equations (2.12) and (2.13) yields an approximation for the second derivative of $T(r,t)$ with respect to r, i.e.[4]

$$\frac{\partial^2 T(r,t)}{\partial r^2} \approx \frac{T(r+\Delta r,t) - 2T(r,t) + T(r-\Delta r,t)}{(\Delta r)^2}. \tag{2.15}$$

By introducing the abbreviations $T_i = T(r_i,t)$ and $q_i = q(r_i,t)$ and exploiting approximations (2.14), (2.15), a set of n coupled ordinary differential equations can be obtained:

$$\frac{dT_i}{dt} = \kappa(T_i)\left[\frac{T_{i+1} - 2T_i + T_{i-1}}{(\Delta r)^2} + \frac{1}{r_i}\frac{T_{i+1} - T_{i-1}}{2\Delta r}\right] + \frac{q_i}{\rho c_p(T_i)} \tag{2.16}$$

Expressing r_i as a multiple of Δr, i.e.

$$r_i := \chi_i \Delta r \quad \text{with} \quad \chi_i = \frac{2i-n-1}{2}, \tag{2.17}$$

leads to

$$\begin{aligned}\frac{dT_i}{dt} &= \kappa(T_i)\left[\frac{T_{i+1} - 2T_i + T_{i-1}}{(\Delta r)^2} + \frac{1}{\chi_i \Delta r}\frac{T_{i+1} - T_{i-1}}{2\Delta r}\right] + \frac{q_i}{\rho c_p(T_i)} \\ &= \frac{\kappa(T_i)}{(\Delta r)^2}\left[\left(1 + \frac{1}{2\chi_i}\right)T_{i+1} - 2T_i + \left(1 - \frac{1}{2\chi_i}\right)T_{i-1}\right] + \frac{q_i}{\rho c_p(T_i)}.\end{aligned} \tag{2.18}$$

One can easily check that a division by zero occurs in (2.18), i.e. $\chi_i = 0$, in case that n is chosen odd and $i = \frac{n+1}{2}$. Furthermore, T_i equals T_{n-i+1} due to symmetry, or in other words, it is sufficient to evaluate the heat equation for only one half of the wafer. To overcome these problems, an offset grid is used, see Figure 2.4. Accordingly, Δr of the

[4]Equations (2.14) and (2.15) are also known as "central difference approximations".

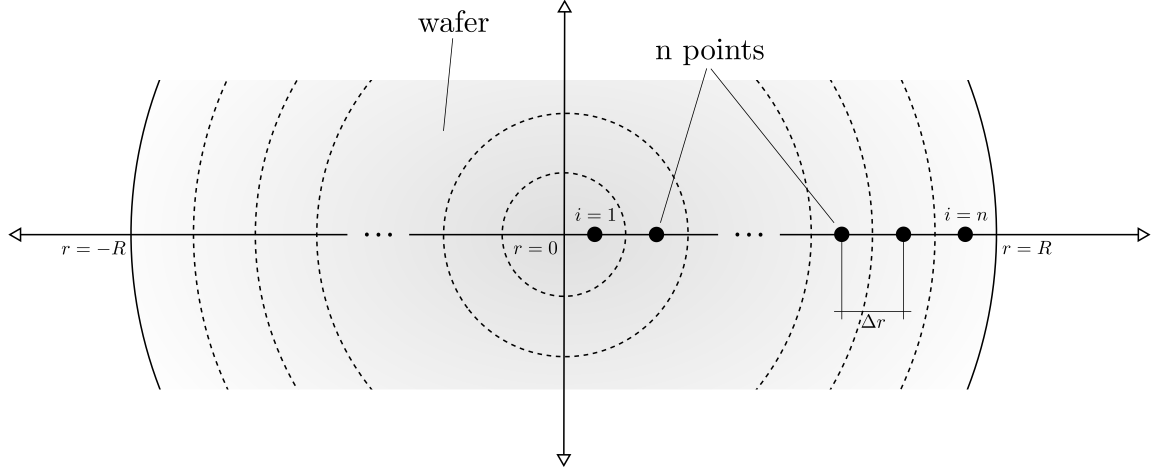

Figure 2.4: Improved grid: An offset grid is used to prevent from a division by zero in the mathematical model.

improved grid computes as

$$\Delta r = \frac{R}{n} \tag{2.19}$$

and the equidistant spatial grid changes to

$$\Omega_{\Delta 2} = \left\{ r_i : r_i = \left(\frac{2i-1}{2} \right) \Delta r;\ i = 1,\ \dots\ n \right\}. \tag{2.20}$$

The final set of ordinary differential equations to approximate the one-dimensional partial differential heat equation in cylindrical coordinates (2.9) can therefore be obtained by exploiting (2.18) with

$$\chi_i = \frac{2i-1}{2}. \tag{2.21}$$

In the following sections, the volumetric heat sources and losses are subdivided into three parts, i.e.

$$q_i = q_{1,i} + q_{2,i} + q_{3,i}, \tag{2.22}$$

where $q_{1,i}$ corresponds to the heat input due to light absorption (see Section 2.2.4). The heat losses due to convection and radiation are denoted by $q_{2,i}$ and $q_{3,i}$ respectively (see Section 2.2.5).

2.2.3 Boundary conditions

To solve (2.9) and (2.18) respectively, suitable initial conditions as well as boundary conditions are required. The initial conditions are given by the wafer's temperature profile

at time instance $t = 0$. Due to the thinness of the wafer and the associated small surface at the edge of the wafer, heat losses in radial direction are negligible[5], i.e. a Neumann boundary condition

$$\left.\frac{\partial T(r,t)}{\partial r}\right|_{r=R} = 0 \tag{2.23}$$

is suitable.

Approximating (2.23) with the forward difference equation yields

$$\frac{\partial T(R,t)}{\partial r} \approx \frac{T_{n+1} - T_n}{\Delta r} = 0 \tag{2.24}$$

and accordingly

$$T_{n+1} = T_n. \tag{2.25}$$

The second boundary condition at the wafer's center results from symmetry and can also be interpreted as a Neumann boundary condition, i.e.

$$T_0 = T_1. \tag{2.26}$$

2.2.4 Heat input due to light absorption

This section discusses the heating-up of the wafer caused by absorption of the light emitted by the LEDs. The LEDs that are used can be treated as Lambertian emitters, i.e. they show a maximum light intensity at an angular displacement of 0° and a falling intensity as the angular displacement increases. Based on this assumption and taking into account reflections between the wafer and components mounted in the process chamber (e.g. the heating plate), the absorption of light can be modelled with the help of a Gaussian distribution with zero mean and a standard deviation σ_l. The considered density function with respect to the distance from the LED denoted by δ therefore reads as

$$D(\delta) = \frac{1}{\sigma_l\sqrt{2\pi}} \exp\left(-\frac{1}{2}\frac{\delta^2}{\sigma_l^2}\right). \tag{2.27}$$

Figure 2.5 schematically depicts the absorption of light emitted by a LED. In order to combine the light absorption with the discretized heat transfer equation, the density function (2.27) is also discretized with a spacing of Δr and the abbreviation

$$D_\mu := D(\mu\Delta r) \tag{2.28}$$

[5]The heat losses at the upper and lower surfaces of the wafer are discussed in Section 2.2.5.

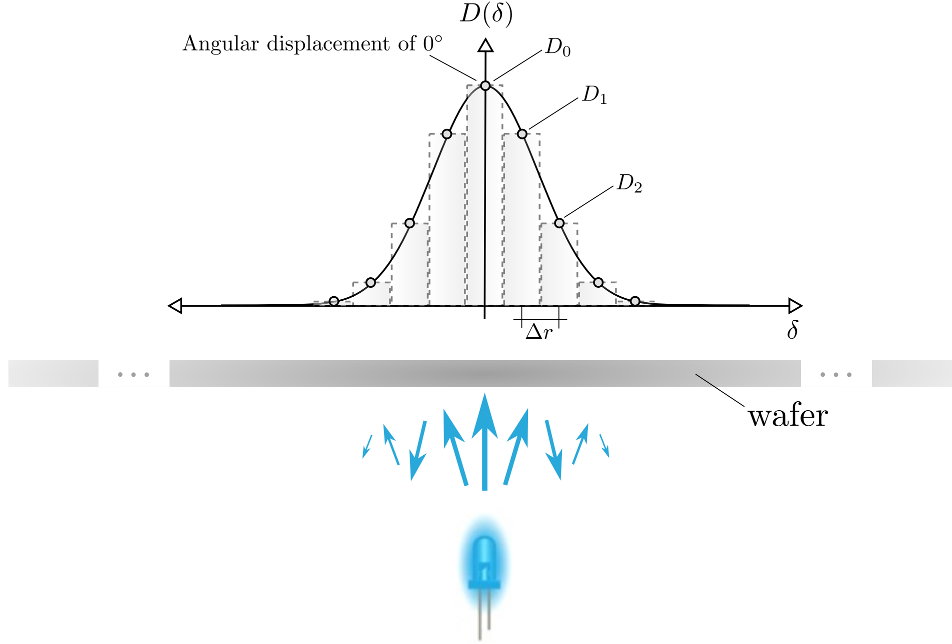

Figure 2.5: Radiation characteristics of an LED: The radiation is modelled with the help of a Gaussian distribution, meaning that the highest light intensity is at an angular displacement of 0°.

for $\mu = 0,\ 1,\ 2,\ \dots\ \infty$ is introduced. In addition, the factors $D_0,\ D_1,\ D_2,\ \dots\ D_\infty$ are scaled such that

$$\sum_{\mu=0}^{\infty} D_\mu = 1. \tag{2.29}$$

The single LEDs mounted on the heating plate are related to one of the n wafer annuli, see Figure 2.6. The average heat input over time due to absorption in ring i with area S_i computes as

$$q_{1,i} = \frac{P_i^t}{hS_i}, \tag{2.30}$$

where P_i^t denotes the total amount of power which is absorbed in ring i and h is the thickness of the wafer. The area of ring i can be computed as

$$S_i = (2i-1)(\Delta r)^2 \pi. \tag{2.31}$$

Note that an LED, which is located at a specific position below the wafer, radiates to all annuli, but with different intensities. Figure 2.7 depicts exemplarily how a lamp located in ring 3 radiates to the individual annuli of the wafer with an intensity factor of D_2. In general, the power in form of light emitted by a LED located in ring μ, which is

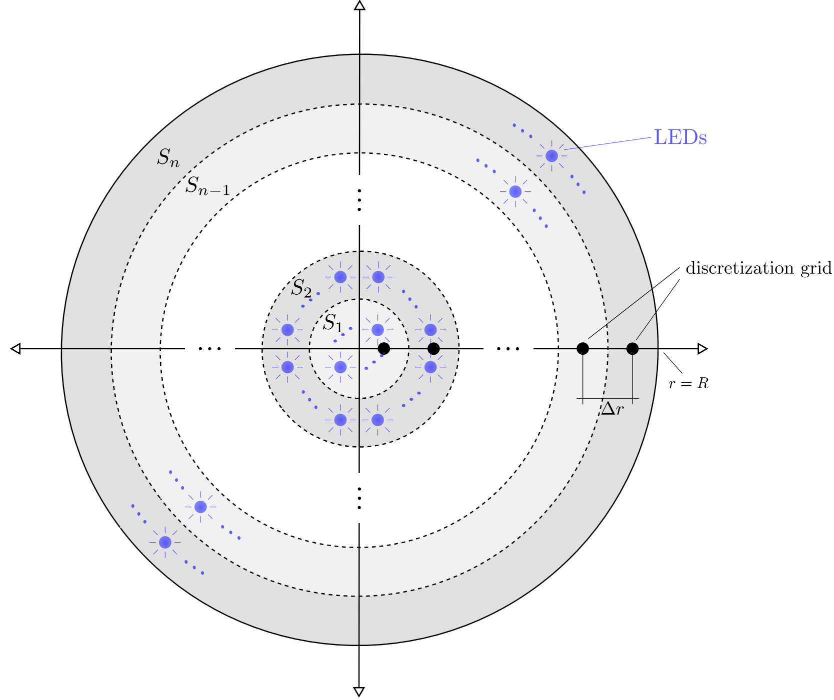

Figure 2.6: Annuli division: A specific number of LEDs can be attributed to each annulus.

absorbed in ring i, can be calculated based on the given area ratios[6]. Thus, considering the radiation of all LEDs, the total amount of power absorbed in ring i computes as

$$P_i^t = \eta \sum_{\mu=1}^{n} \sum_{\nu=1}^{2n} N_\mu P_\mu^e D_{\nu-1} \frac{S_{i,\mu,\nu}}{\sum\limits_{\tau=1}^{n} S_{\tau,\mu,\nu}}, \tag{2.32}$$

where N_μ is the number of LEDs located in ring μ, P_μ^e is the electrical input power per LED in ring μ, $S_{i,\mu,\nu}$ is the area of ring i which is irradiated by a LED in ring μ with an outer radius

$$\overline{r} = \frac{2\nu - 1}{2} \Delta r \tag{2.33}$$

and an inner radius of

$$\underline{r} = \begin{cases} 0 & for \quad \nu = 1 \\ \overline{r} - \Delta r & else \end{cases}. \tag{2.34}$$

The efficiency factor $\eta \in [0, 1]$ describes how much of the applied electrical power is absorbed by the wafer in the form of light and converted to heat. The value of η is typically in the range of 0.5 and mainly characterizes ohmic heat losses of the LEDs.

[6]To calculate the desired area ratios, a formula to compute circle-circle intersections is used, see Appendix B.

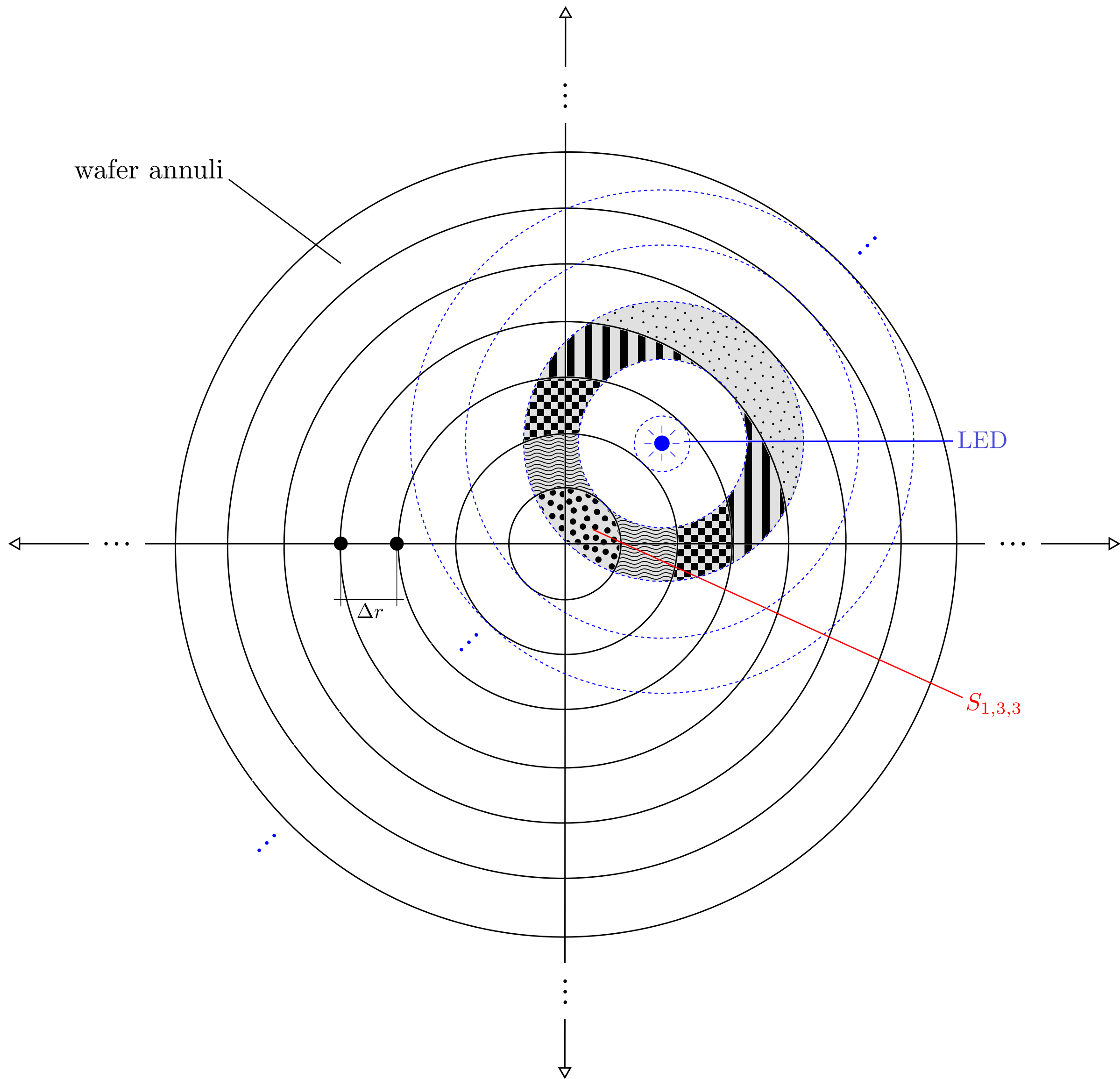

Figure 2.7: Light absorption: The amount of power received in one ring is related to the summation of the absorbed light emitted by the LEDs spread all over the entire heating plate. The intensity of the emitted light decreases as the radial distance to the LED increases.
This sketch exemplary shows, how a LED located in ring 3 radiates with an intensity factor of D_2 to different rings of the discretized system. The irradiated areas are calculated based on geometric considerations.

Inserting (2.32) into (2.30) finally leads to a equation to describe the heat input over time in ring i due to light absorption, i.e.

$$q_{1,i} = \frac{\eta}{hS_i} \sum_{\mu=1}^{n} \sum_{\nu=1}^{2n} N_\mu P_\mu^e D_{\nu-1} \frac{S_{i,\mu,\nu}}{\sum\limits_{\tau=1}^{n} S_{\tau,\mu,\nu}}. \tag{2.35}$$

2.2.5 Heat losses

Heat losses of the wafer are mainly caused by thermal convection and radiation. The heat loss due to convection at radius r_i is proportional to the difference between the wafer's temperature T_i and the ambient temperature T_e, where the latter is assumed to be constant across the wafer. Thus, the heat loss over time due to convection is given as

$$\begin{aligned} q_{2,i} &= \frac{\alpha_i}{h}(T_e - T_i) \\ &= -\frac{\alpha_i}{h}T_i + \frac{\alpha_i}{h}T_e, \end{aligned} \tag{2.36}$$

where α_i denotes the heat transfer coefficient at radius r_i. Note that α_i depends on the gas flow conditions in the chamber as well as the rotational speed of the wafer.

The heat loss due to radiation can be described with the help of the Stefan-Boltzmann law, i.e.

$$q_{3,i} = -2\frac{\varepsilon\sigma_{sb}}{h}T_i^4, \tag{2.37}$$

where ε is the total emissivity of the wafer and σ_{sb} is the Stefan-Boltzmann constant. The factor 2 results from considering heat losses at the upper as well as the lower surface of the wafer. Since the emissivity is very sensitive to the dopant level of the wafer, ε is associated with a high degree of uncertainty [Vandenabeele and Maex, 1991; Sato, 1967]. The process chamber is cooled down to a value close to room temperature. Thus, heat inputs caused by radiation of the environment to the wafer are negligible.

2.2.6 State space representation

By combining heat equation (2.18), the boundary conditions (2.25), (2.26), the heat input (2.35) and heat losses (2.36), (2.37), a set of n ordinary differential equations can

be obtained as

$$\begin{aligned}
\frac{dT_1}{dt} &= \frac{\kappa(T_1)}{(\Delta r)^2}\left[\left(1+\frac{1}{2\chi_1}\right)T_2 + \left(-1-\frac{1}{2\chi_1}\right)T_1\right] + \frac{q_{1,1}+q_{2,1}+q_{3,1}}{\rho c_p(T_1)} \\
\frac{dT_2}{dt} &= \frac{\kappa(T_2)}{(\Delta r)^2}\left[\left(1+\frac{1}{2\chi_2}\right)T_3 - 2T_2 + \left(1-\frac{1}{2\chi_2}\right)T_1\right] + \frac{q_{1,2}+q_{2,2}+q_{3,2}}{\rho c_p(T_2)} \\
&\vdots \\
\frac{dT_n}{dt} &= \frac{\kappa(T_n)}{(\Delta r)^2}\left[\left(-1+\frac{1}{2\chi_n}\right)T_n + \left(1-\frac{1}{2\chi_n}\right)T_{n-1}\right] + \frac{q_{1,n}+q_{2,n}+q_{3,n}}{\rho c_p(T_n)}.
\end{aligned} \tag{2.38}$$

The choice of the system order n is clearly related to the accuracy of the introduced spatial approximations, i.e. the accuracy increases with an increasing system order. On the other hand, a high system order affects the computational effort in solving the obtained set of ordinary differential equations adversely. Depending on the type of the implemented observers and controllers, it can happen that the system has to be discretized in space and time frequently during processing. Furthermore, it might be the case that an optimization problem has to be solved online for the discretized system (see e.g. Section 2.4). Taking into account these considerations as well as the geometry of the system, a suitable choice for the system order is 30. This means that the outermost zone consists of two rings. A system order of 15 would also be feasible, meaning that the outermost zone contains one ring, but in this case the accuracy of the spatial approximations turned out to be insufficient.

The derived set of ordinary differential equations (2.38) can be written in state space representation, where the state vector consists of the wafer's temperatures evaluated on the discretization grid, i.e.

$$\boldsymbol{x} = \begin{bmatrix} x_1 & x_2 & \dots & x_n \end{bmatrix}^T = \begin{bmatrix} T_1 & T_2 & \dots & T_n \end{bmatrix}^T. \tag{2.39}$$

The heating plate is subdivided into four concentric zones as depicted in Figure 2.8, where all LEDs in a zone receive the same electrical power, i.e. the same electrical current flows through all LEDs in a zone. The assignment of the rings to the corresponding zones for a system order of $n = 30$ is summarized in Table 2.1. The inputs to the system are

Zone	**Rings**
1	1 - 16
2	17 - 24
3	25 - 28
4	29 - 30

Table 2.1: Zone division

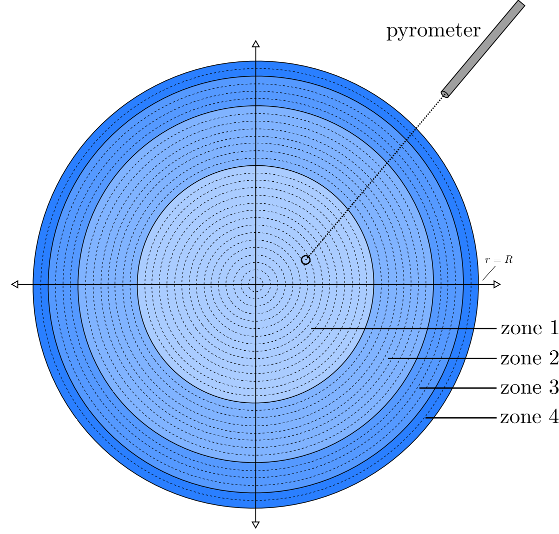

Figure 2.8: Heating plate: The heating plate is divided into four zones, whereas all LEDs in a heating zone must be turned on together with the same amount of electrical power.

the electrical power to the LEDs in each zone as also the ambient temperature, i.e.

$$\boldsymbol{u} = \begin{bmatrix} P^e_{z1} & P^e_{z2} & P^e_{z3} & P^e_{z4} & T_e \end{bmatrix}^T. \tag{2.40}$$

The derived nonlinear, affine-input system then reads as

$$\dot{\boldsymbol{x}} = \boldsymbol{f}(\boldsymbol{x}, \boldsymbol{u}) = \boldsymbol{A}_1(\boldsymbol{x})\boldsymbol{x} - \varepsilon \boldsymbol{A}_2(\boldsymbol{x}) \begin{bmatrix} x_1^4 \\ x_2^4 \\ \vdots \\ x_n^4 \end{bmatrix} + \boldsymbol{B}(\boldsymbol{x})\boldsymbol{u}, \tag{2.41}$$

with the state-dependent matrices $\boldsymbol{A}_1(\boldsymbol{x})$, $\boldsymbol{A}_2(\boldsymbol{x})$ and $\boldsymbol{B}(\boldsymbol{x})$. Matrix $\boldsymbol{A}_1(\boldsymbol{x})$ involves heat conduction as well as heat losses due to convection, i.e.

$$\boldsymbol{A}_1(\boldsymbol{x}) = \ \mathbf{diag}\left(\frac{\kappa(x_i)}{(\Delta r)^2}\right) \begin{bmatrix} \frac{-1-2\chi_1}{2\chi_1} & \frac{1+2\chi_1}{2\chi_1} & & & 0 \\ \frac{-1+2\chi_2}{2\chi_2} & -2 & & & \\ & \ddots & \ddots & & \\ & & -2 & \frac{1+2\chi_{n-1}}{2\chi_{n-1}} & \\ 0 & & \frac{-1+2\chi_n}{2\chi_n} & \frac{1-2\chi_n}{2\chi_n} & \end{bmatrix} - \mathbf{diag}\left(\frac{\alpha_i}{\rho h c_p(x_i)}\right). \tag{2.42}$$

Matrix $\boldsymbol{A}_2(\boldsymbol{x})$ results from evaluating heat losses due to radiation, i.e.

$$\boldsymbol{A}_2(\boldsymbol{x}) = \ \mathbf{diag}\left(\frac{2\sigma_{sb}}{\rho h c_p(x_i)}\right). \tag{2.43}$$

Please note that the uncertain parameter ε is extracted from $\boldsymbol{A}_2(\boldsymbol{x})$ to account for it during the observer design. The input matrix $\boldsymbol{B}(\boldsymbol{x})$ reads as

$$\boldsymbol{B}(\boldsymbol{x}) = \frac{1}{\rho h}\begin{bmatrix} \frac{\eta N_1}{c_p(x_1)S_1}\sum\limits_{\nu=1}^{2n} D_{\nu-1}\frac{S_{1,1,\nu}}{\sum\limits_{\tau=1}^{n} S_{\tau,1,\nu}} & \cdots & \frac{\eta N_n}{c_p(x_1)S_1}\sum\limits_{\nu=1}^{2n} D_{\nu-1}\frac{S_{1,n,\nu}}{\sum\limits_{\tau=1}^{n} S_{\tau,n,\nu}} & \frac{\alpha_1}{c_p(x_1)} \\ \frac{\eta N_1}{c_p(x_2)S_2}\sum\limits_{\nu=1}^{2n} D_{\nu-1}\frac{S_{2,1,\nu}}{\sum\limits_{\tau=1}^{n} S_{\tau,1,\nu}} & \cdots & \frac{\eta N_n}{c_p(x_2)S_2}\sum\limits_{\nu=1}^{2n} D_{\nu-1}\frac{S_{2,n,\nu}}{\sum\limits_{\tau=1}^{n} S_{\tau,n,\nu}} & \frac{\alpha_2}{c_p(x_2)} \\ \vdots & & \vdots & \\ \frac{\eta N_1}{c_p(x_n)S_n}\sum\limits_{\nu=1}^{2n} D_{\nu-1}\frac{S_{n,1,\nu}}{\sum\limits_{\tau=1}^{n} S_{\tau,1,\nu}} & \cdots & \frac{\eta N_n}{c_p(x_n)S_n}\sum\limits_{\nu=1}^{2n} D_{\nu-1}\frac{S_{n,n,\nu}}{\sum\limits_{\tau=1}^{n} S_{\tau,n,\nu}} & \frac{\alpha_n}{c_p(x_n)} \end{bmatrix}\boldsymbol{Z} \tag{2.44}$$

with

$$\boldsymbol{Z} = \begin{bmatrix} 1 & & & & 0 \\ \vdots & & & & \\ 1 & & & & \\ & 1 & & & \\ & \vdots & & & \\ & 1 & & & \\ & & 1 & & \\ & & \vdots & & \\ & & 1 & & \\ & & & 1 & \\ & & & 1 & \\ 0 & & & & 1 \end{bmatrix} \begin{matrix} \left.\vphantom{\begin{matrix}1\\1\\1\end{matrix}}\right\} \text{related to el. power supplied to LEDs in zone 1} \\ \left.\vphantom{\begin{matrix}1\\1\\1\end{matrix}}\right\} \text{related to el. power supplied to LEDs in zone 2} \\ \left.\vphantom{\begin{matrix}1\\1\\1\end{matrix}}\right\} \text{related to el. power supplied to LEDs in zone 3} \\ \left.\vphantom{\begin{matrix}1\\1\end{matrix}}\right\} \text{related to el. power supplied to LEDs in zone 4} \\ \left.\vphantom{1}\right\} \text{related to ambient temperature.} \end{matrix}$$

The output of the introduced system is defined as the temperatures measured at the radial midpoint of each of the four zones as illustrated in Figure 2.9. Accordingly, the output equation is expressed as

$$\boldsymbol{y} = \begin{bmatrix} y_1 & y_2 & y_3 & y_4 \end{bmatrix}^T = \boldsymbol{C}\boldsymbol{x}, \tag{2.45}$$

where the output matrix for test rigs reads as

$$\boldsymbol{C} = \begin{bmatrix} \boldsymbol{c}_1^T \\ \boldsymbol{c}_2^T \\ \boldsymbol{c}_3^T \\ \boldsymbol{c}_4^T \end{bmatrix} = \begin{bmatrix} \boldsymbol{0}^T & 1 & \boldsymbol{0}^T & 0 & \boldsymbol{0}^T & 0 & \boldsymbol{0}^T & 0 & \boldsymbol{0}^T \\ \boldsymbol{0}^T & 0 & \boldsymbol{0}^T & 1 & \boldsymbol{0}^T & 0 & \boldsymbol{0}^T & 0 & \boldsymbol{0}^T \\ \boldsymbol{0}^T & 0 & \boldsymbol{0}^T & 0 & \boldsymbol{0}^T & 1 & \boldsymbol{0}^T & 0 & \boldsymbol{0}^T \\ \boldsymbol{0}^T & 0 & \boldsymbol{0}^T & 0 & \boldsymbol{0}^T & 0 & \boldsymbol{0}^T & 1 & \boldsymbol{0}^T \end{bmatrix}. \tag{2.46}$$

It mainly consists of zeros, aside a single one in each row at column indices $\lfloor \frac{0.04}{\Delta r} + \frac{1}{2} \rfloor$, $\lfloor \frac{0.1}{\Delta r} + \frac{1}{2} \rfloor$, $\lfloor \frac{0.13}{\Delta r} + \frac{1}{2} \rfloor$ and $\lfloor \frac{0.145}{\Delta r} + \frac{1}{2} \rfloor$ respectively. Please notice that only pyrometer 1, which

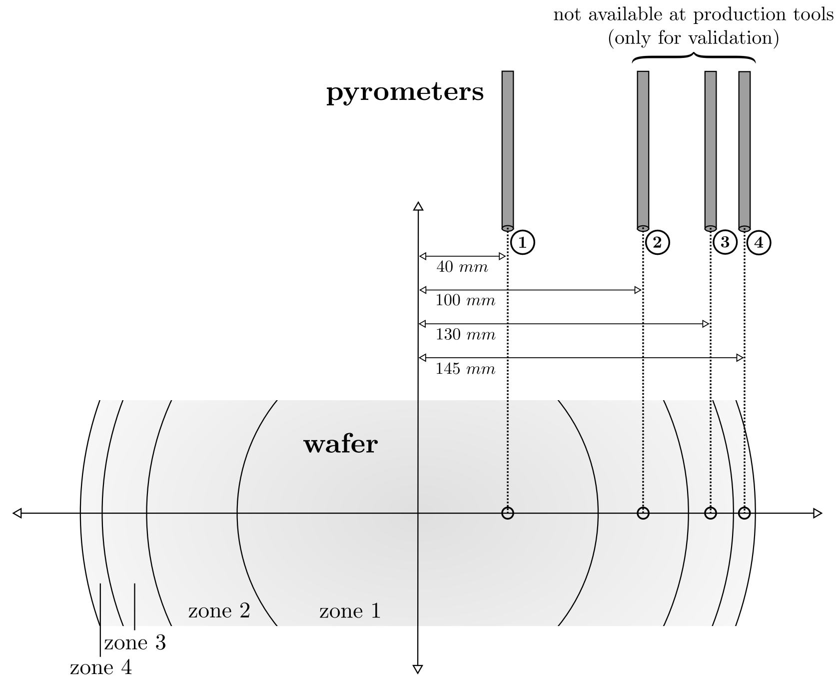

Figure 2.9: Temperature sensors: Four pyrometers are used to measure the temperature at the radial midpoint of each heating zone. Only pyrometer 1 is available at production systems, the others are just used for validation purposes at the test rig.

is measuring the temperature of the wafer at a distance of 40 mm from the wafer center, is available at production tools. This means that the output equation for production tools is just

$$y_1 = \boldsymbol{c}_1^T \boldsymbol{x}. \tag{2.47}$$

Pyrometers 2 to 4 are only available at the test rigs for validation purposes.

2.2.7 Plant model validation

To validate the mathematical model, a heating-up experiment with a so-called "highly doped" wafer is carried out on a test rig, which is built up as described in Section 2.1. The wafer, which is at room temperature before starting the experiment, is rotating with 10 revolutions per minute. The chamber is continuously flushed with gasses supplied at room temperature and a flow of 10 liters per minute. Thus, the ambient temperature T_e is assumed to be 25 $°C$ (298.15 K). The used model parameters are listed in Table 2.2. Due to the small air flow and the low rotational speed, the heat loss due to convection is assumed to be uniformly distributed across the wafer, i.e. all heat transfer coefficients are chosen equally.

The plant is excited with a power setting as depicted in Figure 2.10. The temperatures in

Parameter	Description	Value	Unit
ρ	density	2336	$\frac{kg}{m^3}$
$\lambda_c(T)$	heat conductivity	$150\left(\frac{T}{300}\right)^{-1.3}$	$\frac{W}{mK}$
$c_p(T)$	heat capacity	$703 + \frac{255\left[\left(\frac{T}{300}\right)^{1.85}-1\right]}{\left(\frac{T}{300}\right)^{1.85}+\frac{255}{703}}$	$\frac{J}{kgK}$
h	thickness of wafer	$775 \cdot 10^{-6}$	m
η	efficiency/absorptivity factor	0.5	-
σ_l	standard deviation	0.11	m
ε	total emissivity	0.65	-
$\alpha_1, \alpha_2, \ \ldots \ \alpha_{30}$	heat transfer coefficients	1	$\frac{W}{m^2K}$
σ_{sb}	Stefan-Boltzmann constant	$5.6704 \cdot 10^{-8}$	$\frac{W}{m^2K^4}$

Table 2.2: Experiment, model parameters

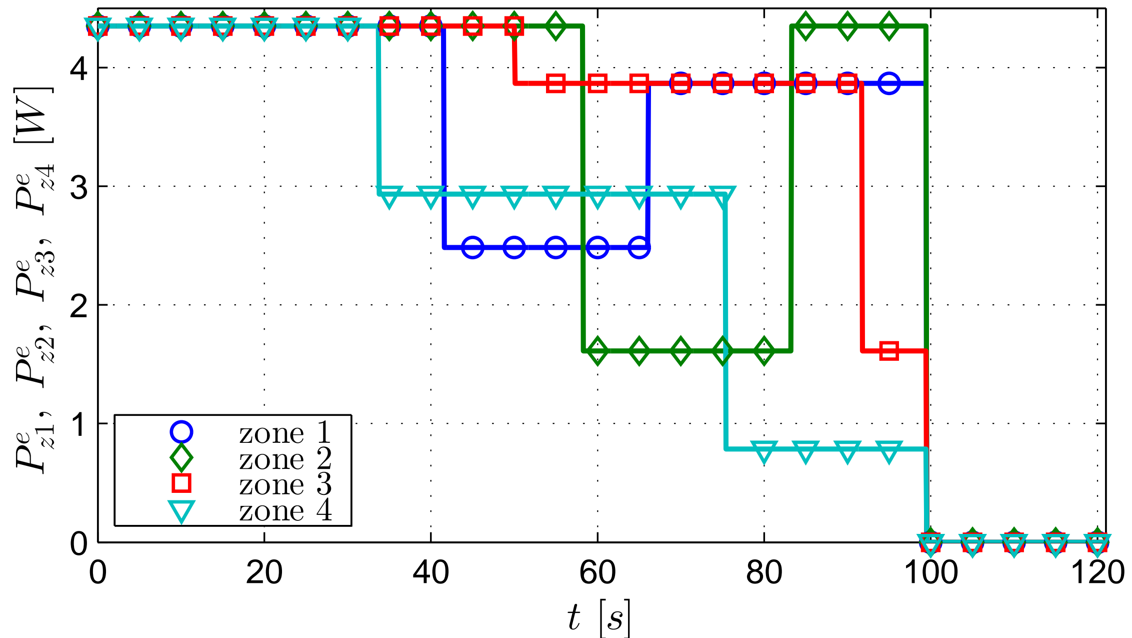

Figure 2.10: Input signals: The electrical power to the four heating zones is varied in order to verify the accuracy of the mathematical model.

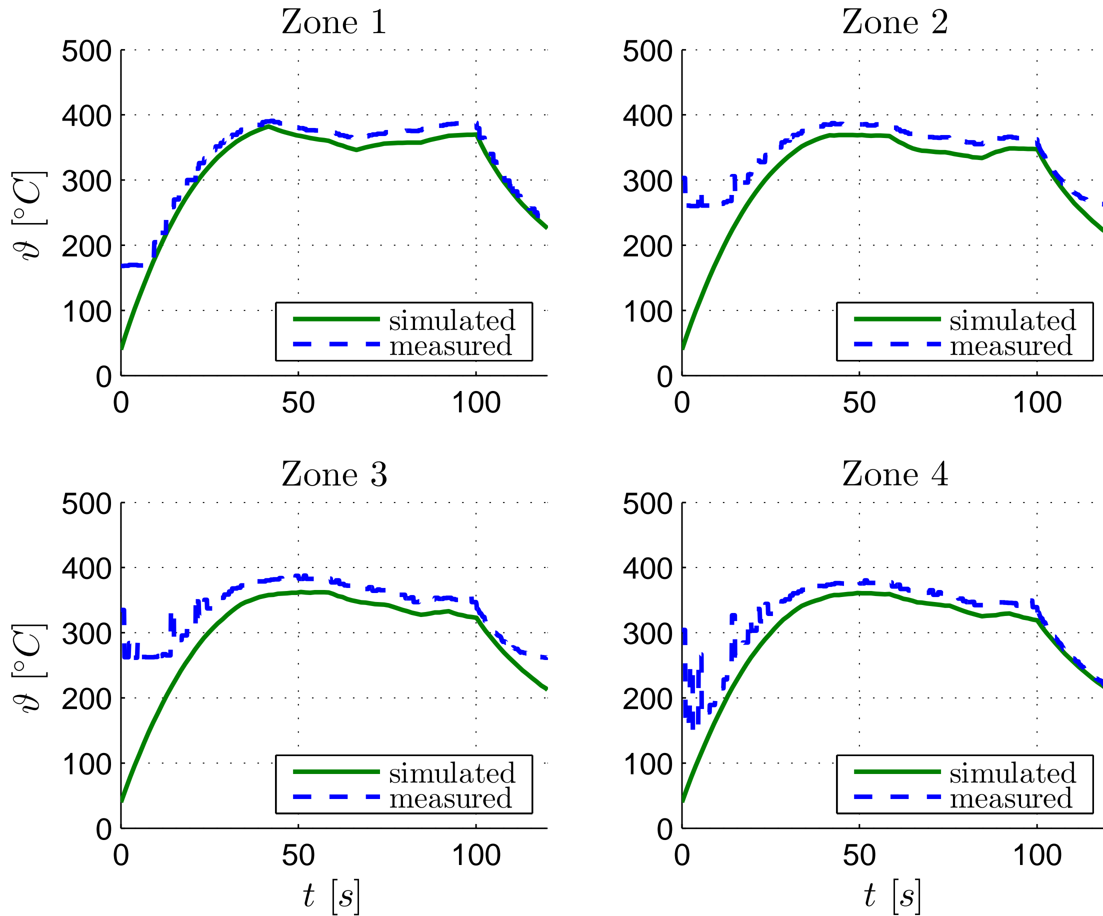

Figure 2.11: Plant model validation: The wafer's temperature measured in the four zones is compared to the simulated output of the plant model. The "highly doped" wafer is heated starting at room temperature. Since the pyrometers cannot be used to measure low temperatures, the initial measurements are incorrect.

the four zones are measured with pyrometers as shown in Figure 2.9. As Figure 2.11 shows and referring to the technical data sheet of the pyrometers, the temperature readings are not reliable at low temperatures. This does not pose a problem for the process which requires temperatures above 300 $°C$ (573.15 K). Apart from that, it can be seen that the derived mathematical model captures the dynamics of the system sufficiently well in order to design model-based observers and controllers.

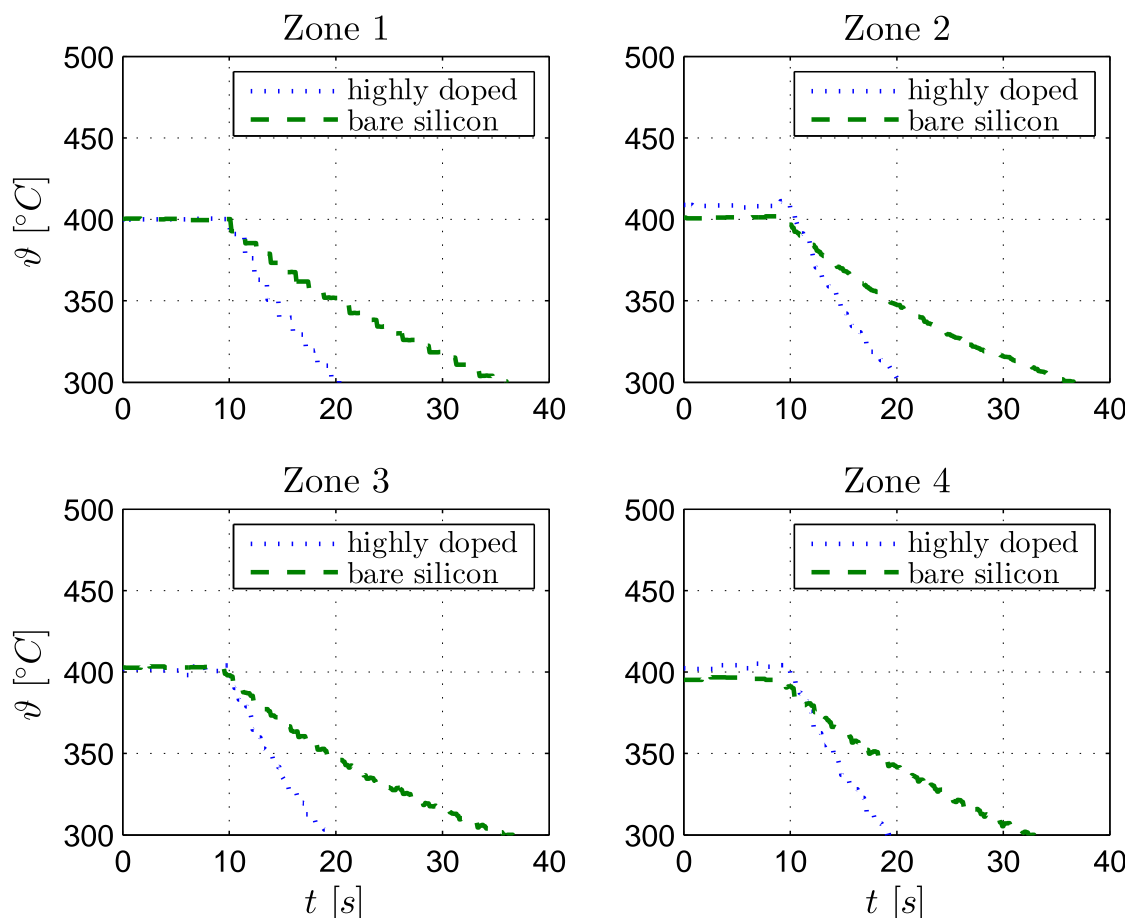

Figure 2.12: Wafer sensitivity: An experiment points out different cooling down characteristics of wafers with diverse values for their total emissivity.

2.3 Wafer sensitivity

As indicated in Section 2.2, the total emissivity ε heavily depends on the wafer type, in particular on its dopant level and coating. The total emissivity can vary from 0.2 to 0.9. To demonstrate this dependency, an experiment[7] is carried out where two contrary wafer types, namely a "highly doped" wafer and a "bare silicon" wafer are heated to approximately 400 $°C$. Accordingly, the cooling down of the two wafer types is analyzed. A comparison is depicted in Figure 2.12. Referring to the experiment it can be concluded that a "highly doped" wafer cools down much faster than a "bare silicon" wafer, i.e. the total emissivity rises with an increasing dopant level.

To cope with the unknown total emissivity of the processed wafer, an appropriate observer

[7]The measurement setup remains unchanged, i.e. like described in Section 2.2.7.

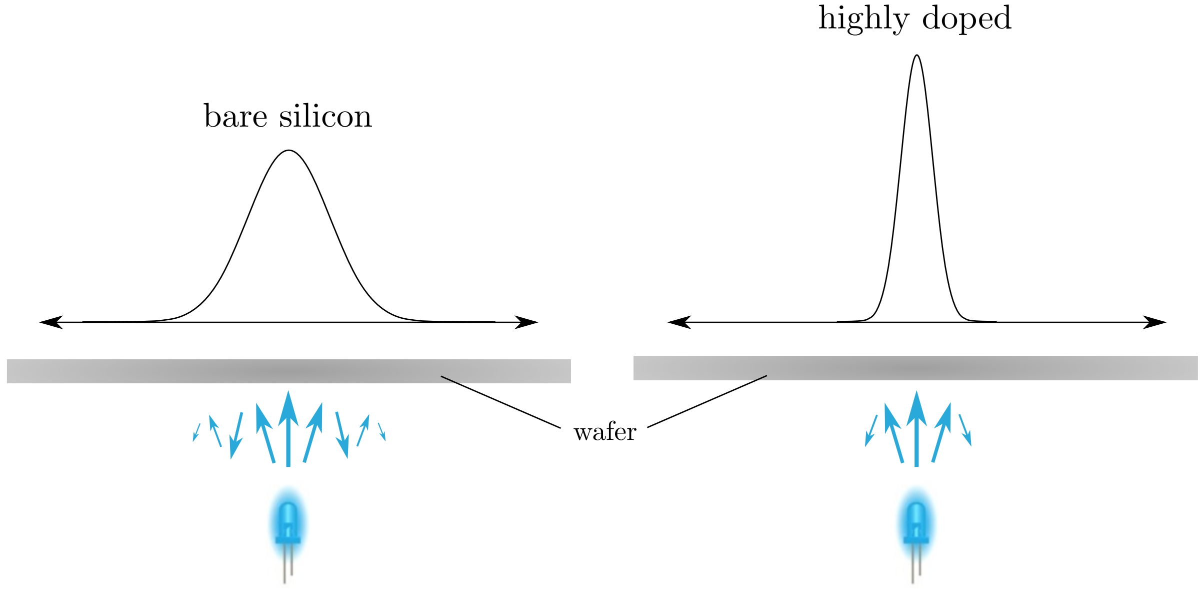

Figure 2.13: Total emissivity and light absorption: The dopand level of the wafer has an impact on its reflectivity. This in turn affects the standard deviation of the Gaussian distribution used to model the light absorption. Highly doped wafers show a narrower light absorption than less doped wafer due to its lower reflectivity.

approach is used later on. In addition to the emissivity, it turned out that the standard deviation of the Gaussian distribution introduced to model the light absorption is also dependent on the wafer type. This dependency can be mainly attributed to the reflectivity of different wafer types which is dependent on the dopant level and coating. For example, the standard deviation to model the light absorption of a bare silicon wafer is higher than those for a "highly doped" wafer (see illustration in Figure 2.13). Thus, the question arises if it is possible to conclude from the emissivity on the value of the standard deviation. Therefor, the emissivity as well as the standard deviation of the model are adjusted for a variety of heating up experiments with different wafer types. Figure 2.14 depicts the determined relation between the total emissivity and standard deviation. Thus, with the help of a nonlinear regression, the standard deviation can be expressed as a function of the total emissivity, i.e.

$$\sigma_l = 0.01656\,\varepsilon^{-1.475} + 0.07674. \tag{2.48}$$

Since the standard deviation is dependent on the total emissivity, in fact also the input matrix depends on ε, i.e. the latter reads as $\boldsymbol{B}(\boldsymbol{x}, \varepsilon)$ instead of $\boldsymbol{B}(\boldsymbol{x})$ subsequently.

2.4 Observer design based on classical approaches

As outlined, an observer for (2.41) with the output $y_1 = \boldsymbol{c}_1^T \boldsymbol{x}$ is designed.

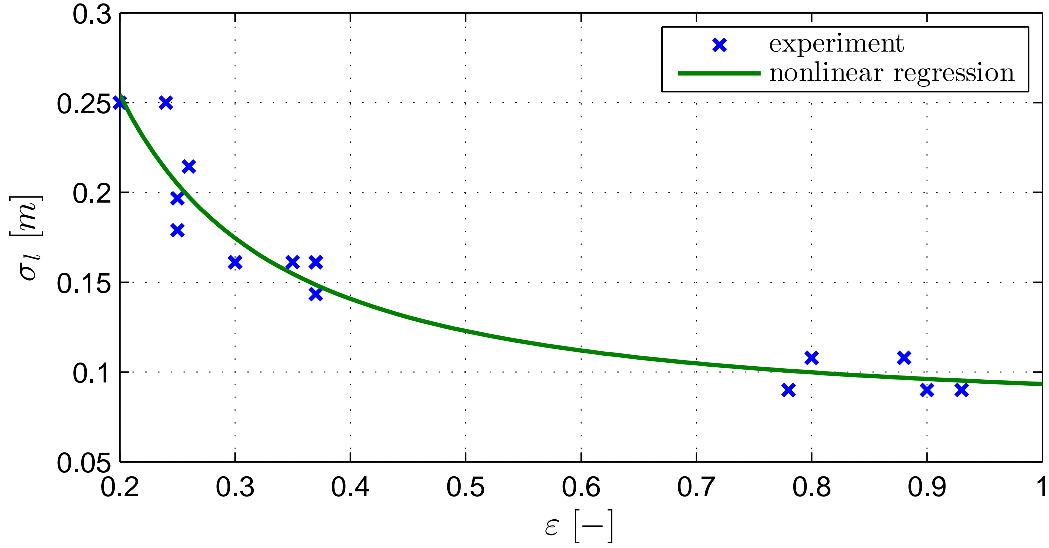

Figure 2.14: Relationship between total emissivity and standard deviation: A mathematical relation between the total emissivity of the wafer and the standard deviation used to model the light absorption is found with the help of a nonlinear regression.

2.4.1 Additional estimate for the total emissivity

To account for the uncertain parameter ε, the latter is considered as an additional state variable, i.e. the augmented state vector is defined as

$$\tilde{\boldsymbol{x}} := \begin{bmatrix} \boldsymbol{x} \\ \varepsilon \end{bmatrix}. \tag{2.49}$$

The additional estimation of system parameters generally leads to nonlinear models. Since the derived plant model (2.41) is in any case nonlinear, this does not represent additional effort, except that the system order of the augmented system is increased by one. Under the assumption that ε is constant or at most changes slowly over time, the augmented nonlinear system can be written as

$$\dot{\tilde{\boldsymbol{x}}} = \tilde{\boldsymbol{f}}(\tilde{\boldsymbol{x}}, \boldsymbol{u}) = \begin{bmatrix} \boldsymbol{A}_1(\boldsymbol{x})\boldsymbol{x} - \varepsilon \boldsymbol{A}_2(\boldsymbol{x}) \begin{bmatrix} x_1^4 \\ x_2^4 \\ \vdots \\ x_n^4 \end{bmatrix} + \boldsymbol{B}(\boldsymbol{x}, \varepsilon)\boldsymbol{u} \\ \hdashline 0 \end{bmatrix}. \tag{2.50}$$

By introducing the state vector $\tilde{\boldsymbol{x}}$, the output equation also needs to be adapted, i.e.

$$y_1 = \begin{bmatrix} \boldsymbol{c}_1^T & 0 \end{bmatrix} \tilde{\boldsymbol{x}} = \tilde{\boldsymbol{c}}_1^T \tilde{\boldsymbol{x}}. \tag{2.51}$$

2.4.2 Observability check

Prior to the design of the observer, the observability of the augmented system needs to be checked. An approach discussed in [Banks, Lewis, and Tran, 2007] is thus applied, which deals with the determination of the observability for a class of nonlinear systems, namely systems in state-dependent coefficient form.

Rewriting (2.50) and (2.51) in such a form yields

$$\begin{aligned}\dot{\tilde{\boldsymbol{x}}} &= \tilde{\boldsymbol{A}}(\tilde{\boldsymbol{x}})\tilde{\boldsymbol{x}} + \tilde{\boldsymbol{B}}(\tilde{\boldsymbol{x}})\boldsymbol{u}, \\ y_1 &= \tilde{\boldsymbol{c}}_1^T\tilde{\boldsymbol{x}},\end{aligned} \tag{2.52}$$

with

$$\tilde{\boldsymbol{A}}(\tilde{\boldsymbol{x}}) = \left[\begin{array}{c:c} \boldsymbol{A}_1(\boldsymbol{x}) & -\boldsymbol{A}_2(\boldsymbol{x})\begin{bmatrix} x_1^4 \\ x_2^4 \\ \vdots \\ x_n^4 \end{bmatrix} \\ \hdashline \boldsymbol{0}^T & 0 \end{array}\right] \quad \text{and} \quad \tilde{\boldsymbol{B}}(\tilde{\boldsymbol{x}}) = \begin{bmatrix} \boldsymbol{B}(\boldsymbol{x}, \varepsilon) \\ \boldsymbol{0}^T \end{bmatrix}. \tag{2.53}$$

As outlined in the paper, system (2.52) with system order $\tilde{n} = n + 1$ is observable if the state-dependent observability matrix

$$\tilde{\boldsymbol{B}}_y(\tilde{\boldsymbol{x}}) = \begin{bmatrix} \tilde{\boldsymbol{c}}_1^T \\ \tilde{\boldsymbol{c}}_1^T\tilde{\boldsymbol{A}}(\tilde{\boldsymbol{x}}) \\ \vdots \\ \tilde{\boldsymbol{c}}_1^T\tilde{\boldsymbol{A}}^{(\tilde{n}-1)}(\tilde{\boldsymbol{x}}) \end{bmatrix} \tag{2.54}$$

has full rank for all $\tilde{\boldsymbol{x}}$. Clearly, instead of checking the rank of the observability matrix, it is also possible to check if every right eigenvector $\tilde{\boldsymbol{w}}(\tilde{\boldsymbol{x}})$ of $\tilde{\boldsymbol{A}}(\tilde{\boldsymbol{x}})$ with respect to the eigenvalue $\tilde{\lambda}(\tilde{\boldsymbol{x}})$, i.e. $\tilde{\boldsymbol{A}}(\tilde{\boldsymbol{x}})\tilde{\boldsymbol{w}}(\tilde{\boldsymbol{x}}) = \tilde{\lambda}(\tilde{\boldsymbol{x}})\tilde{\boldsymbol{w}}(\tilde{\boldsymbol{x}})$, satisfies

$$\tilde{\boldsymbol{c}}_1^T\tilde{\boldsymbol{w}}(\tilde{\boldsymbol{x}}) \neq 0. \tag{2.55}$$

This condition is not verified analytically for all possible values of $\tilde{\boldsymbol{x}}$ within the scope of this thesis. However, it is illustrated at least numerically that (2.55) is fulfilled for a large number of randomly chosen vectors $\tilde{\boldsymbol{x}}$, whose first n temperature elements are within the considered range of 0 to 400 $°C$ (273.15 to 673.15 K)[8]. Figure 2.15 plots the minimum absolute value of $\tilde{\boldsymbol{c}}^T\tilde{\boldsymbol{w}}(\tilde{\boldsymbol{x}})$ on a logarithmic scale over the number of iterations. It points out that $\min\left(\left|\tilde{\boldsymbol{c}}^T\tilde{\boldsymbol{w}}(\tilde{\boldsymbol{x}})\right|\right)$ is in all cases unequal to zero. Thus, it can be concluded that also the remaining right eigenvectors fulfill condition (2.55) and hence, system (2.41) with output (2.45) is assumed to be observable in the considered temperature range.

[8] Note that the last element of $\tilde{\boldsymbol{x}}$, namely the total emissivity, does not effect $\tilde{\boldsymbol{A}}(\tilde{\boldsymbol{x}})$.

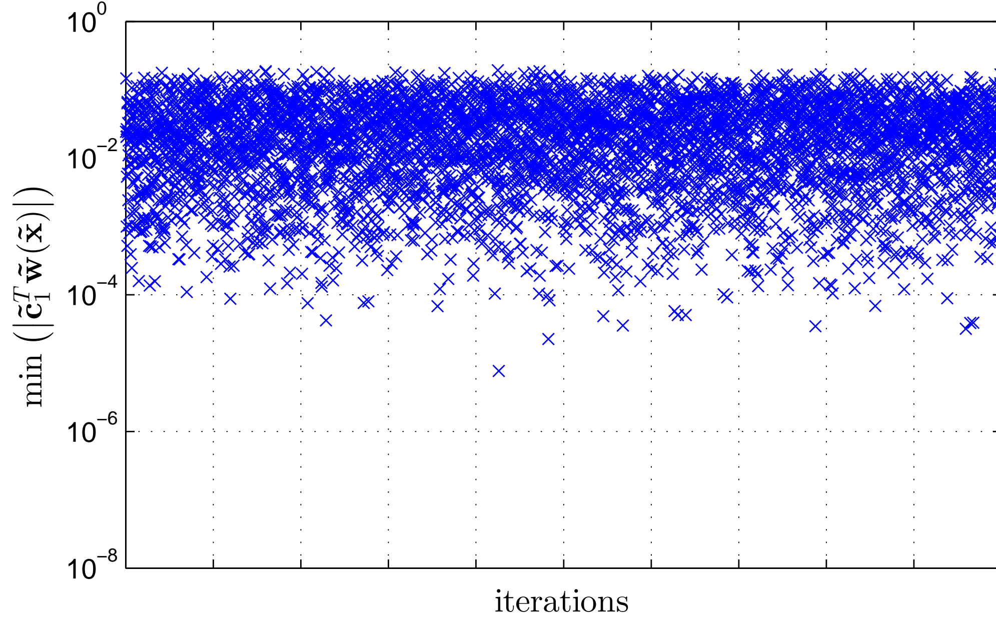

Figure 2.15: Numerical observability check: The observability of the introduced system in state-dependent coefficient form is analyzed numerically by carrying out a large number of simulations and checking if any right eigenvector of the system matrix $\tilde{\boldsymbol{A}}(\tilde{\boldsymbol{x}})$ is orthogonal to the output vector $\tilde{\boldsymbol{c}}^T$.

2.4.3 Linearization around the estimated state vector

Similar to the extended Kalman filter, the nonlinear system (2.50) is linearized by means of a Taylor series of $\tilde{\boldsymbol{f}}(\tilde{\boldsymbol{x}}, \boldsymbol{u})$ at the estimated state vector

$$\hat{\tilde{\boldsymbol{x}}} = \begin{bmatrix} \hat{\boldsymbol{x}} & \hat{\varepsilon} \end{bmatrix}^T. \tag{2.56}$$

Truncating the latter after the linear term leads to

$$\tilde{\boldsymbol{f}}(\tilde{\boldsymbol{x}}, \boldsymbol{u}) \approx \tilde{\boldsymbol{f}}(\hat{\tilde{\boldsymbol{x}}}, \boldsymbol{u}) + \left.\frac{\partial \tilde{\boldsymbol{f}}(\tilde{\boldsymbol{x}}, \boldsymbol{u})}{\partial \tilde{\boldsymbol{x}}}\right|_{\tilde{\boldsymbol{x}}=\hat{\tilde{\boldsymbol{x}}}} (\tilde{\boldsymbol{x}} - \hat{\tilde{\boldsymbol{x}}}). \tag{2.57}$$

Since the heat conductivity λ_c as also the heat capacity c_p change slowly with temperature and the factors D_μ used to model the light absorption change slowly with the emissivity, the derivatives of the elements in the state-dependent matrices $\boldsymbol{A}_1(\boldsymbol{x})$, $\boldsymbol{A}_2(\boldsymbol{x})$ and $\boldsymbol{B}(\boldsymbol{x}, \varepsilon)$ with respect to the elements in $\tilde{\boldsymbol{x}}$ can be treated as zero. This allows to obtain a linearized

system (for detailed calculations see Appendices C and D)

$$\dot{\tilde{\boldsymbol{x}}} \approx \underbrace{\left[\begin{array}{c:c} \boldsymbol{A}_1(\hat{\boldsymbol{x}}) - 4\hat{\varepsilon}\boldsymbol{A}_2(\hat{\boldsymbol{x}}) \begin{bmatrix} \hat{x}_1^3 & & & 0 \\ & \hat{x}_2^3 & & \\ & & \ddots & \\ 0 & & & \hat{x}_n^3 \end{bmatrix} & -\boldsymbol{A}_2(\hat{\boldsymbol{x}}) \begin{bmatrix} \hat{x}_1^4 \\ \hat{x}_2^4 \\ \vdots \\ \hat{x}_n^4 \end{bmatrix} \\ \hdashline \boldsymbol{0}^T & 0 \end{array}\right]}_{=:\,\bar{\boldsymbol{A}}} \begin{bmatrix} \boldsymbol{x} \\ \varepsilon \end{bmatrix}$$

$$+ \underbrace{\begin{bmatrix} \boldsymbol{B}(\hat{\boldsymbol{x}}, \hat{\varepsilon}) \\ \boldsymbol{0}^T \end{bmatrix}}_{=:\,\bar{\boldsymbol{B}}} \boldsymbol{u} + \underbrace{\left[\begin{array}{c} 4\hat{\varepsilon}\boldsymbol{A}_2(\hat{\boldsymbol{x}}) \begin{bmatrix} \hat{x}_1^4 \\ \hat{x}_2^4 \\ \vdots \\ \hat{x}_n^4 \end{bmatrix} \\ \hdashline 0 \end{array}\right]}_{=:\,\bar{\boldsymbol{f}}} . \tag{2.58}$$

The output equation remains unchanged. Please note that the observability within the considered temperature range of the linearized pair $(\tilde{\boldsymbol{c}}_1^T, \bar{\boldsymbol{A}})$ can be shown in a manner similar to that in Section 2.4.2.

2.4.4 System discretization

It is intended to implement the observer at a programmable logic controller. Thus, the design is carried out in discrete time. Note that the discretization must be carried out in each sampling instance, since $\bar{\boldsymbol{A}}$, $\bar{\boldsymbol{B}}$ and $\bar{\boldsymbol{f}}$ depend on the estimated state $\hat{\tilde{\boldsymbol{x}}}$. Thus, the discretized system

$$\begin{aligned} \tilde{\boldsymbol{x}}_{k+1} &= \boldsymbol{\Phi}_k(T_s)\tilde{\boldsymbol{x}}_k + \boldsymbol{H}_k\boldsymbol{u}_k + \boldsymbol{h}_k, \\ y_{1,k} &= \tilde{\boldsymbol{c}}_1^T\tilde{\boldsymbol{x}}_k \end{aligned} \tag{2.59}$$

is treated as a time-variant.

The matrix $\boldsymbol{\Phi}_k(T_s)$ is the state transition matrix of (2.58) evaluated at the sampling time T_s and $\boldsymbol{H}_k$, $\boldsymbol{h}_k$ calculate as

$$\begin{aligned} \boldsymbol{H}_k &= \int_0^{T_s} \boldsymbol{\Phi}_k(\tau)\bar{\boldsymbol{B}}\mathrm{d}\tau, \\ \boldsymbol{h}_k &= \int_0^{T_s} \boldsymbol{\Phi}_k(\tau)\bar{\boldsymbol{f}}\mathrm{d}\tau. \end{aligned} \tag{2.60}$$

To calculate $\boldsymbol{\Phi}_k(T_s)$, $\boldsymbol{H}_k$ and $\boldsymbol{h}_k$ efficiently, the matrix exponential

$$\boldsymbol{\Phi}_k(t) = \exp\left(\bar{\boldsymbol{A}}t\right) = \boldsymbol{I} + \bar{\boldsymbol{A}}t + \frac{\bar{\boldsymbol{A}}^2 t^2}{2!} + \dots \tag{2.61}$$

is utilized [Franklin, Workman, and Powell, 1997], i.e. the state transition matrix evaluated at T_s computes as

$$\boldsymbol{\Phi}_k(T_s) = \boldsymbol{I} + \bar{\boldsymbol{A}}T_s + \frac{\bar{\boldsymbol{A}}^2 T_s^2}{2!} + \dots \;. \tag{2.62}$$

Furthermore, inserting (2.61) into (2.60) leads to

$$\begin{aligned}\boldsymbol{H}_k &= \int_0^{T_s} \left(\boldsymbol{I} + \bar{\boldsymbol{A}}\tau + \frac{\bar{\boldsymbol{A}}^2\tau^2}{2!} + \dots\right)\bar{\boldsymbol{B}}\mathrm{d}\tau \\ &= \left(\bar{\boldsymbol{B}}\tau + \frac{\bar{\boldsymbol{A}}\bar{\boldsymbol{B}}\tau^2}{2!} + \frac{\bar{\boldsymbol{A}}^2\bar{\boldsymbol{B}}\tau^3}{3!} + \dots\right)\Bigg|_0^{T_s} = \bar{\boldsymbol{B}}T_s + \frac{\bar{\boldsymbol{A}}\bar{\boldsymbol{B}}T_s^2}{2!} + \frac{\bar{\boldsymbol{A}}^2\bar{\boldsymbol{B}}T_s^3}{3!} + \dots\end{aligned} \tag{2.63}$$

and

$$\boldsymbol{h}_k = \bar{\boldsymbol{f}}T_s + \frac{\bar{\boldsymbol{A}}\bar{\boldsymbol{f}}T_s^2}{2!} + \frac{\bar{\boldsymbol{A}}^2\bar{\boldsymbol{f}}T_s^3}{3!} + \dots \tag{2.64}$$

respectively. One can easily check that the matrix exponential

$$\exp\left(\begin{bmatrix}\bar{\boldsymbol{A}} & \bar{\boldsymbol{B}} & \bar{\boldsymbol{f}}\\ \boldsymbol{0} & \boldsymbol{0} & \boldsymbol{0}\\ \boldsymbol{0} & \boldsymbol{0} & 0\end{bmatrix}T_s\right) = \begin{bmatrix}\boldsymbol{I} & \boldsymbol{0} & \boldsymbol{0}\\ \boldsymbol{0} & \boldsymbol{I} & \boldsymbol{0}\\ \boldsymbol{0} & \boldsymbol{0} & 1\end{bmatrix} + \begin{bmatrix}\bar{\boldsymbol{A}}T_s & \bar{\boldsymbol{B}}T_s & \bar{\boldsymbol{f}}T_s\\ \boldsymbol{0} & \boldsymbol{0} & \boldsymbol{0}\\ \boldsymbol{0} & \boldsymbol{0} & 0\end{bmatrix} + \dots \tag{2.65}$$

can be used to compute the discretized matrices as

$$\begin{bmatrix}\boldsymbol{\Phi}_k(T_s) & \boldsymbol{H}_k & \boldsymbol{h}_k\\ \boldsymbol{0} & \boldsymbol{I} & \boldsymbol{0}\\ \boldsymbol{0} & \boldsymbol{0} & 1\end{bmatrix} = \exp\left(\begin{bmatrix}\bar{\boldsymbol{A}} & \bar{\boldsymbol{B}} & \bar{\boldsymbol{f}}\\ \boldsymbol{0} & \boldsymbol{0} & \boldsymbol{0}\\ \boldsymbol{0} & \boldsymbol{0} & 0\end{bmatrix}T_s\right). \tag{2.66}$$

It can numerically be shown that $\bar{\boldsymbol{A}}$ has distinct real eigenvalues. Thus, properties such as controllability and observability are preserved after discretization [Horn and Dourdoumas, 2004].

2.4.5 Luenberger observer design based on LQR approach

A Luenberger observer for the system (2.59) is designed[9], i.e.

$$\hat{\tilde{\boldsymbol{x}}}_{k+1} = \boldsymbol{\Phi}_k\hat{\tilde{\boldsymbol{x}}}_k + \boldsymbol{H}_k\boldsymbol{u}_k + \boldsymbol{h}_k + \hat{\boldsymbol{l}}_k\left(y_{1,k} - \hat{y}_{1,k}\right), \tag{2.67}$$

[9] For the sake of readability, the argument of $\boldsymbol{\Phi}_k(T_s)$ is omitted subsequently.

where $\hat{\boldsymbol{l}}_k$ denotes the observer gain. The estimation error is defined as

$$\tilde{\boldsymbol{e}}_k := \tilde{\boldsymbol{x}}_k - \hat{\tilde{\boldsymbol{x}}}_k. \tag{2.68}$$

Consequently, the error dynamics compute as

$$\begin{aligned}\tilde{\boldsymbol{e}}_{k+1} &= \tilde{\boldsymbol{x}}_{k+1} - \hat{\tilde{\boldsymbol{x}}}_{k+1}\\ &= \boldsymbol{\Phi}_k\tilde{\boldsymbol{x}}_k + \boldsymbol{H}_k\boldsymbol{u}_k + \boldsymbol{h}_k - \boldsymbol{\Phi}_k\hat{\tilde{\boldsymbol{x}}}_k - \boldsymbol{H}_k\boldsymbol{u}_k - \boldsymbol{h}_k - \hat{\boldsymbol{l}}_k\tilde{\boldsymbol{c}}_1^T\tilde{\boldsymbol{x}}_k + \hat{\boldsymbol{l}}_k\tilde{\boldsymbol{c}}_1^T\hat{\tilde{\boldsymbol{x}}}_k\\ &= \left(\boldsymbol{\Phi}_k - \hat{\boldsymbol{l}}_k\tilde{\boldsymbol{c}}_1^T\right)\underbrace{\left(\tilde{\boldsymbol{x}}_k - \hat{\tilde{\boldsymbol{x}}}_k\right)}_{\tilde{\boldsymbol{e}}_k}.\end{aligned}$$

Thus, the goal is to establish $\hat{\boldsymbol{l}}_k$ in such a manner that the estimation error converges to zero as k tends to infinity.

Since $\left(\boldsymbol{\Phi}_k - \hat{\boldsymbol{l}}_k\tilde{\boldsymbol{c}}_1^T\right)$ has the same eigenvalues as its transpose $\left(\boldsymbol{\Phi}_k^T - \tilde{\boldsymbol{c}}_1\hat{\boldsymbol{l}}_k^T\right)$, designing a Luenberger observer for (2.59) equals the design of a state feedback controller

$$\bar{u}_k = -\hat{\boldsymbol{l}}_k^T\boldsymbol{z}_k \tag{2.69}$$

for its so-called "dual system"

$$\boldsymbol{z}_{k+1} = \boldsymbol{\Phi}_k^T\boldsymbol{z}_k + \tilde{\boldsymbol{c}}_1\bar{u}_k. \tag{2.70}$$

In order to find an appropriate observer gain, the LQR (linear–quadratic regulator) approach is applied, i.e. the latter calculates as

$$\hat{\boldsymbol{l}}_k^T = \frac{1}{v_o + \tilde{\boldsymbol{c}}_1^T\boldsymbol{Y}_k\tilde{\boldsymbol{c}}_1}\tilde{\boldsymbol{c}}_1^T\boldsymbol{Y}_k\boldsymbol{\Phi}_k^T. \tag{2.71}$$

The matrix $\boldsymbol{Y}_k$ is computed by evaluating the discrete Riccati equation for time-varying systems

$$\boldsymbol{Y}_{k+1} = \boldsymbol{W}_o + \boldsymbol{\Phi}_k\boldsymbol{Y}_k\boldsymbol{\Phi}_k^T - \frac{1}{v_o + \tilde{\boldsymbol{c}}_1^T\boldsymbol{Y}_k\tilde{\boldsymbol{c}}_1}\boldsymbol{\Phi}_k\boldsymbol{Y}_k\tilde{\boldsymbol{c}}_1\tilde{\boldsymbol{c}}_1^T\boldsymbol{Y}_k\boldsymbol{\Phi}_k^T \tag{2.72}$$

with the constant weighting factors $\boldsymbol{W}_o \succcurlyeq 0$ and $v_o > 0$. Please note that the convergence of the Riccati equation is ensured if the matrix $\boldsymbol{W}_o$ is chosen in such a manner that the pair $(\boldsymbol{\Phi}_k, \boldsymbol{W}_o)$ is stabilizable and the pair $(\tilde{\boldsymbol{c}}_1^T, \boldsymbol{\Phi}_k)$ is observable [Franklin, Workman, and Powell, 1997; Phillips and Nagle, 2015].

Zone	Power per LED [W]
1	3.0
2	2.5
3	2.0
4	1.0

Table 2.3: Power setting

2.4.6 Numerical simulation

A numerical simulation is carried out to verify the designed observer. Therefor, a heat-up scenario of a wafer with a total emissivity of 0.7 is realized by means of the constant power setting listed in Table 2.3. The sampling time is chosen in accordance with the update rate of the used power supply for the LED heater, which is 1.3 s. The model parameters listed in Table 2.2 are used for the simulation model as well as for the observer. In contrast to the open-loop experiment, the standard deviation σ_l to model the light absorption is now depending on the emissivity like described in Section 2.3. The weighting matrix $\boldsymbol{W}_o$ is chosen as

$$\boldsymbol{W}_o = \begin{bmatrix} 10 & & & 0 \\ & \ddots & & \\ & & 10 & \\ 0 & & & 0.01 \end{bmatrix}, \tag{2.73}$$

v_o is set to 1 and $\boldsymbol{Y}_0 = \boldsymbol{W}_o$. The initial wafer's temperature of the simulation model is set to $25°C$ (298.15 K) and the initial wafer's temperature of the observer is set to $200°C$ (473.15 K). The estimate for the total emissivity is bounded according to its physical limits, i.e. between 0.2 and 0.9. Its initial value is set to 0.9.

Figure 2.16 shows the simulated and estimated zone temperatures and Figure 2.17 depicts the corresponding estimation errors over time. It can be seen that the estimation errors with respect to temperature tend to zero. Moreover, Figure 2.18 demonstrates that the estimated total emissivity converges to the nominal value used in the simulation model.

2.4.7 Laboratory experiments

The designed observer is applied to the laboratory plant introduced in Section 2.1. As control unit, a programmable logic controller from Bernecker and Rainer[10] is used. The

[10]www.br-automation.com

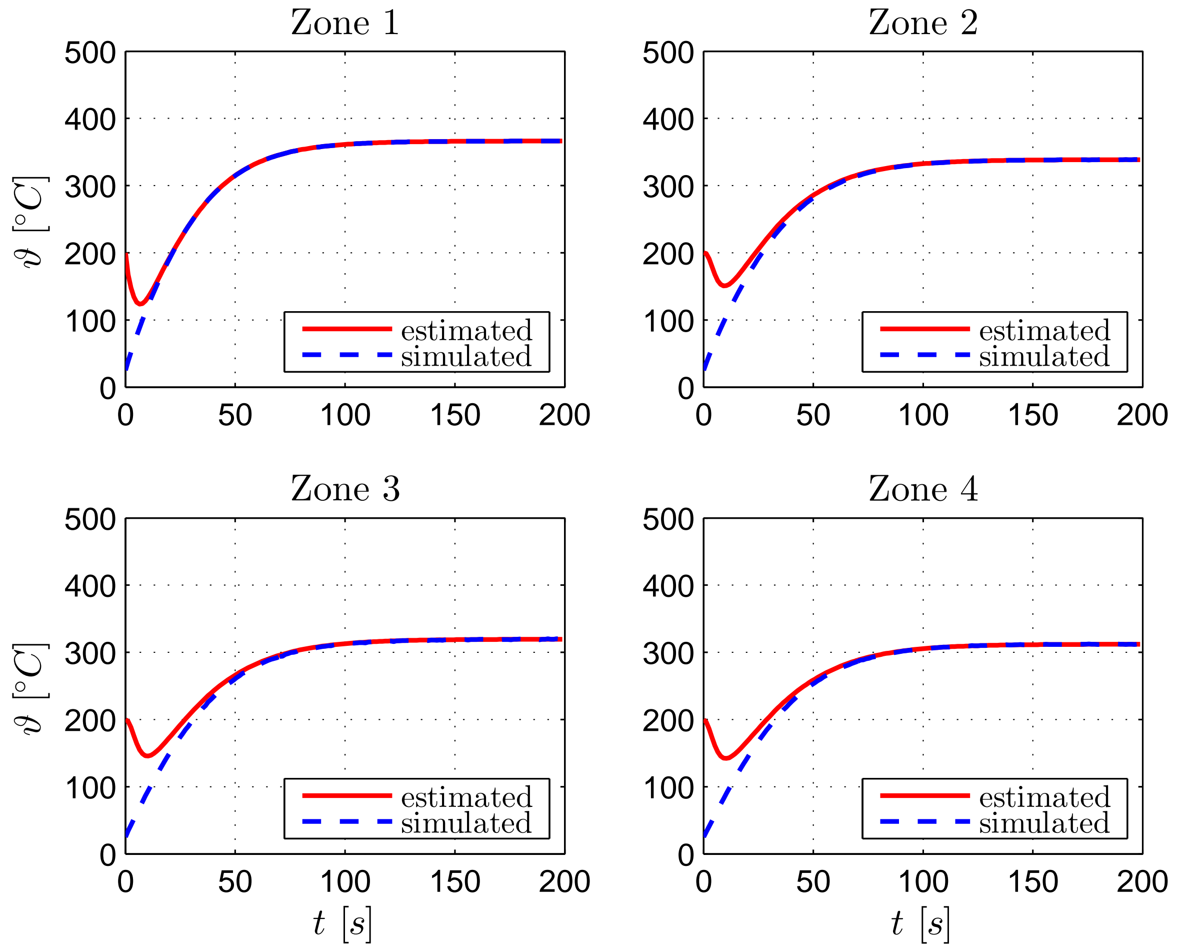

Figure 2.16: Simulated and estimated zone temperatures: The simulation points out that the estimated wafer temperature converges to the simulated one.

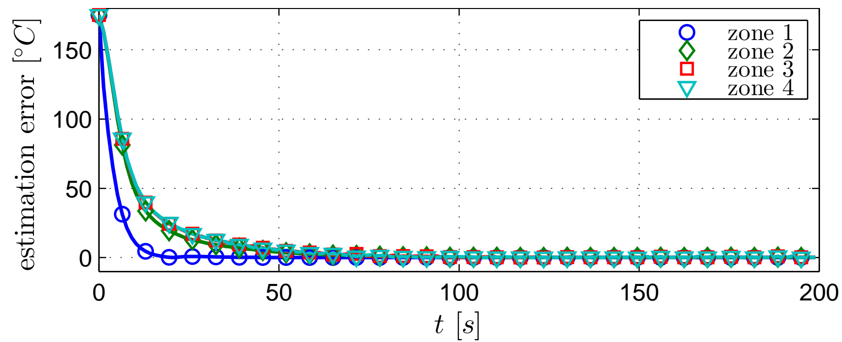

Figure 2.17: Estimation error: The estimation error with respect to temperature tends to zero.

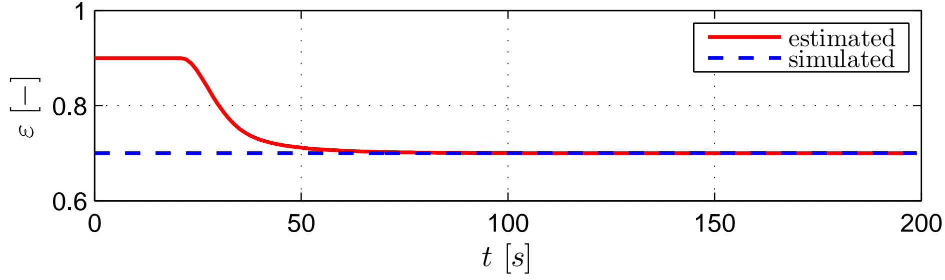

Figure 2.18: Emissivity estimate: The unknown total emissivity of the wafer can be reconstructed by the observer.

sampling period is set to $T_s = 1.3\ s$ and the model parameters as well as the weighting matrices are chosen as in Section 2.4.6. The initial values[11] of the observer are set to

$$\hat{\tilde{\boldsymbol{x}}}_0 = \begin{bmatrix} 473.15 & \dots & 473.15 & 0.2 \end{bmatrix}^T .$$

The same power setting as depicted in Figure 2.10 is applied to the test rig to heat up a "highly doped" wafer. Four pyrometers are used to measure the wafer's temperature in the four zones. These temperatures are compared to the estimated ones in Figure 2.19. As the comparison shows, it is possible to estimate the wafer's temperature profile with the help of the designed observer. From Figure 2.20 it can also be seen that the estimated total emissivity tends to a value of approximately 0.8, which is feasible for a "highly doped" wafer.

2.4.8 Comparison with Kalman filter

The calculation of the observer gain for the Luenberger observer designed in Section 2.4.5 is motivated by means of the LQR approach. There, the choice of the weighting matrices is not straightforward and relies to a large extend on the experience of the designer.

On the other hand, the derivation of the Kalman filter, is motivated by stochastic properties of the considered process. In the following, a Kalman filter for the derived discrete-time system (2.59) is designed. Therefore, the latter is formally extended with process noise $\boldsymbol{\omega}_{d,k}$ as well as measurement noise $\omega_{n,k}$, i.e.

$$\begin{aligned} \tilde{\boldsymbol{x}}_{k+1} &= \boldsymbol{\Phi}_k \tilde{\boldsymbol{x}}_k + \boldsymbol{H}_k \boldsymbol{u}_k + \boldsymbol{h}_k + \boldsymbol{\omega}_{d,k}, \\ y_{1,k} &= \tilde{\boldsymbol{c}}_1^T \tilde{\boldsymbol{x}}_k + \omega_{n,k}. \end{aligned} \tag{2.74}$$

[11]The wafer is primarily heated up from room temperature, i.e. 25°C (298.15 K), but since the used pyrometer cannot measure low temperatures, the initial temperature values are chosen as 200°C (473.15 K).

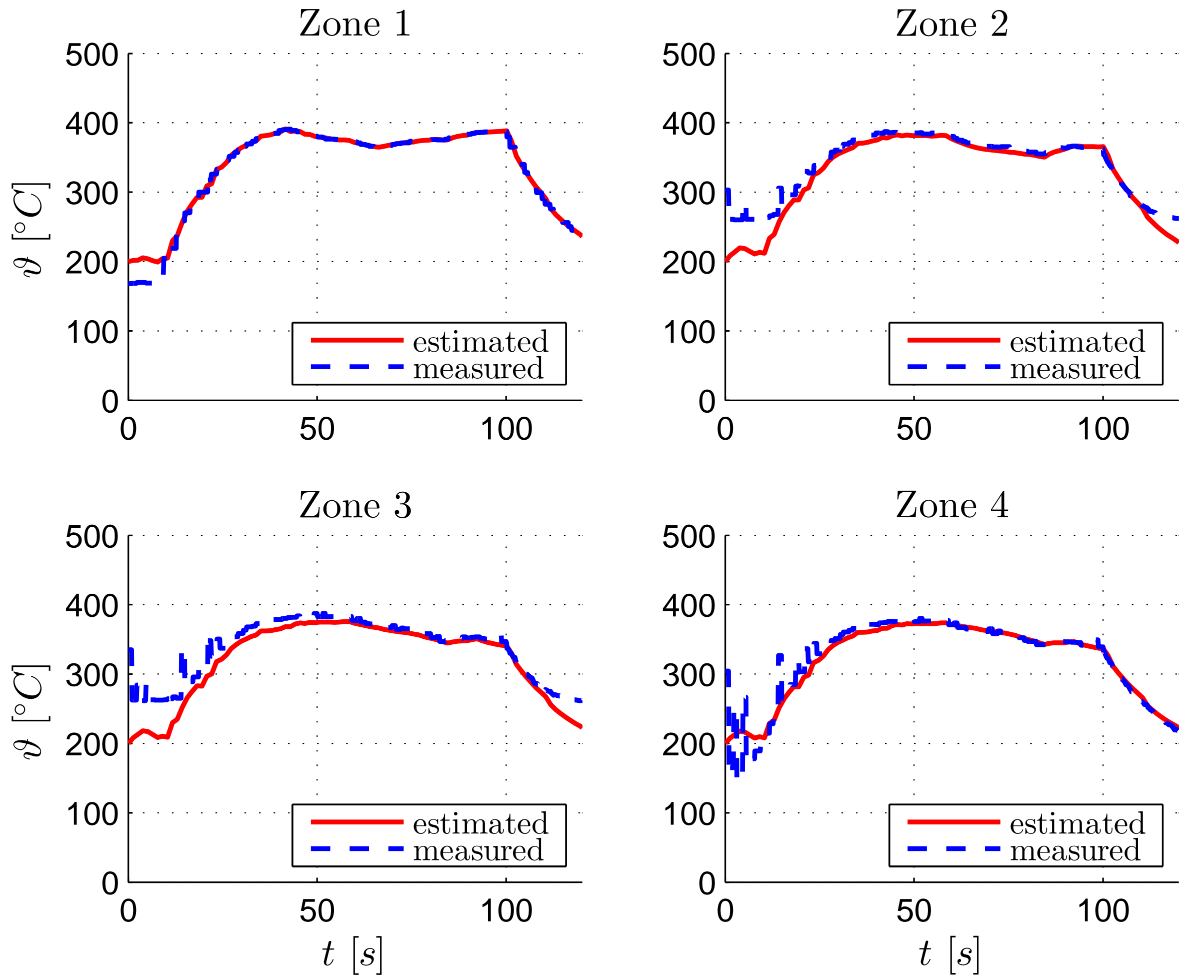

Figure 2.19: Measured and estimated output, "highly doped" wafer: The zone temperatures measured with the help of pyrometers are compared to the estimated ones.

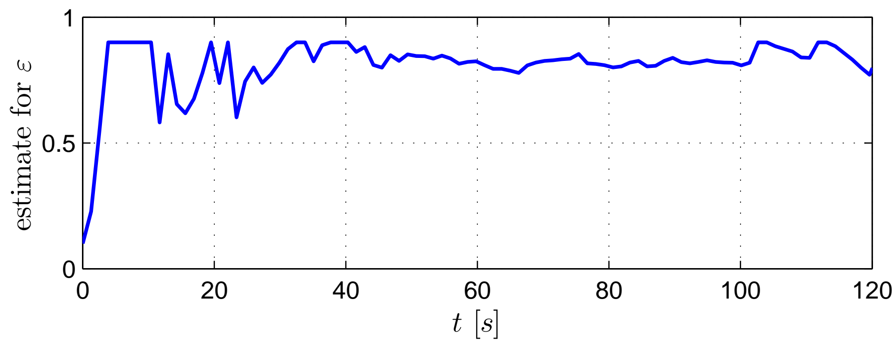

Figure 2.20: Estimated emissivity, "highly doped" wafer: The designed observer also provides an estimate for the total emissivity of the processed wafer.

The measurement noise is due to physical effects in the pyrometer, the process noise being generated by the digital to analogue (D/A) converter for the zone power signals. Thus, it can be assumed that measurement noise and process noise are uncorrelated. Furthermore, the noise signals can be assumed to be Gaussian, white and unbiased.

The state vector is also considered as a stochastic quantity. The expectation value of the initial state $\tilde{\boldsymbol{x}}_0$ is given as

$$E\{\tilde{\boldsymbol{x}}_0\} = \boldsymbol{m}_0 \tag{2.75}$$

and its covariance matrix is given as

$$E\{(\tilde{\boldsymbol{x}}_0 - \boldsymbol{m}_0)(\tilde{\boldsymbol{x}}_0 - \boldsymbol{m}_0)^T\} = \boldsymbol{M}_0. \tag{2.76}$$

The purpose of the Kalman filter is to find the optimal estimate $\hat{\tilde{\boldsymbol{x}}}_k$ such that the expectation value of the estimation error $\bar{\tilde{\boldsymbol{x}}}_k := \tilde{\boldsymbol{x}}_k - \hat{\tilde{\boldsymbol{x}}}_k$ becomes zero, i.e.

$$E\{\bar{\tilde{\boldsymbol{x}}}_k\} = 0 \tag{2.77}$$

and the sum of the variances, i.e. $E\left\{\bar{\tilde{\boldsymbol{x}}}_k^T \bar{\tilde{\boldsymbol{x}}}_k\right\}$, becomes minimal. The covariance matrix of the estimation error is defined as

$$\boldsymbol{Y}_k := E\left\{\bar{\tilde{\boldsymbol{x}}}_k \bar{\tilde{\boldsymbol{x}}}_k^T\right\}. \tag{2.78}$$

So we are looking for a recursive scheme that can be used starting from

$$\hat{\tilde{\boldsymbol{x}}}_{k-1},\ \boldsymbol{Y}_{k-1} \text{ and } y_{1,k} \tag{2.79}$$

to determine the current estimate $\hat{\tilde{\boldsymbol{x}}}_k$ as well as the current covariance matrix of the estimation error, i.e. $\boldsymbol{Y}_k$.

The widespread form of the Kalman filter [Grewal and Andrews, 2001] for the system (2.74) can be written with the five equations

$$\begin{aligned}
\underline{\text{I}}:\quad & \tilde{\boldsymbol{x}}_k^* = \boldsymbol{\Phi}_{k-1}\hat{\tilde{\boldsymbol{x}}}_{k-1} + \boldsymbol{H}_{k-1}\boldsymbol{u}_{k-1} + \boldsymbol{h}_{k-1}\ , \\
\underline{\text{II}}:\quad & \boldsymbol{Y}_k^* = \boldsymbol{\Phi}_{k-1}\boldsymbol{Y}_{k-1}\boldsymbol{\Phi}_{k-1}^T + \boldsymbol{W}_{o,k}\ , \quad \boldsymbol{Y}_0^* = \boldsymbol{M}_0\ , \\
\underline{\text{III}}:\quad & \hat{\boldsymbol{l}}_k = \boldsymbol{Y}_k^*\tilde{\boldsymbol{c}}_1\left(\tilde{\boldsymbol{c}}_1^T\boldsymbol{Y}_k^*\tilde{\boldsymbol{c}}_1 + v_o\right)^{-1}\ , \\
\underline{\text{IV}}:\quad & \boldsymbol{Y}_k = \left(\boldsymbol{I} - \hat{\boldsymbol{l}}_k\tilde{\boldsymbol{c}}_1^T\right)\boldsymbol{Y}_k^*\left(\boldsymbol{I} - \hat{\boldsymbol{l}}_k\tilde{\boldsymbol{c}}_1^T\right)^T + \hat{\boldsymbol{l}}_k v_o \hat{\boldsymbol{l}}_k^T\ , \\
\underline{\text{V}}:\quad & \hat{\tilde{\boldsymbol{x}}}_k = \boldsymbol{\Phi}_{k-1}\hat{\tilde{\boldsymbol{x}}}_{k-1} + \boldsymbol{H}_{k-1}\boldsymbol{u}_{k-1} + \boldsymbol{h}_{k-1} + \hat{\boldsymbol{l}}_k\left(y_{1,k} - \tilde{\boldsymbol{c}}_1^T\tilde{\boldsymbol{x}}_k^*\right)\ .
\end{aligned} \tag{2.80}$$

The first equation of (2.80) is based on a copy of the plant, i.e.

$$\hat{\tilde{\boldsymbol{x}}}_{k+1} = \boldsymbol{\Phi}_k \hat{\tilde{\boldsymbol{x}}}_k + \boldsymbol{H}_k \boldsymbol{u}_k + \boldsymbol{h}_k + \boldsymbol{\omega}_{d,k} \tag{2.81}$$

and

$$\hat{\tilde{\boldsymbol{x}}}_k = \boldsymbol{\Phi}_{k-1} \hat{\tilde{\boldsymbol{x}}}_{k-1} + \boldsymbol{H}_{k-1} \boldsymbol{u}_{k-1} + \boldsymbol{h}_{k-1} + \boldsymbol{\omega}_{d,k-1} \tag{2.82}$$

respectively, where $\tilde{\boldsymbol{x}}_k$ is replaced by $\hat{\tilde{\boldsymbol{x}}}_k$. This first step is well known from the design of the classical asymptotic observer. However, since the noise vector $\boldsymbol{\omega}_{d,k-1}$ is unknown, a further auxiliary quantity $\tilde{\boldsymbol{x}}_k^*$ is introduced and the unknown term is omitted, i.e.

$$\tilde{\boldsymbol{x}}_k^* = \boldsymbol{\Phi}_{k-1} \hat{\tilde{\boldsymbol{x}}}_{k-1} + \boldsymbol{H}_{k-1} \boldsymbol{u}_{k-1} + \boldsymbol{h}_{k-1}. \tag{2.83}$$

The obtained first Kalman filter equation is referred to as the calculation of the a-priori estimate of $\tilde{\boldsymbol{x}}_k$. Furthermore, the first Kalman filter equation can be rewritten as

$$\begin{aligned}
\tilde{\boldsymbol{x}}_k^* &= \boldsymbol{\Phi}_{k-1} \hat{\tilde{\boldsymbol{x}}}_{k-1} + \boldsymbol{H}_{k-1} \boldsymbol{u}_{k-1} + \boldsymbol{h}_{k-1} \\
&= \boldsymbol{\Phi}_{k-1} \left(\tilde{\boldsymbol{x}}_{k-1} - \bar{\tilde{\boldsymbol{x}}}_{k-1} \right) + \boldsymbol{H}_{k-1} \boldsymbol{u}_{k-1} + \boldsymbol{h}_{k-1} \\
&= \underbrace{\boldsymbol{\Phi}_{k-1} \tilde{\boldsymbol{x}}_{k-1} + \boldsymbol{H}_{k-1} \boldsymbol{u}_{k-1} + \boldsymbol{h}_{k-1}}_{= \, \tilde{\boldsymbol{x}}_k - \boldsymbol{\omega}_{d,k-1}} - \boldsymbol{\Phi}_{k-1} \bar{\tilde{\boldsymbol{x}}}_{k-1}.
\end{aligned} \tag{2.84}$$

Thus, the a-priori estimate may be interpreted as the sum of the unknown state vector and an error, i.e.

$$\tilde{\boldsymbol{x}}_k^* = \tilde{\boldsymbol{x}}_k + \underbrace{\left(-\boldsymbol{\Phi}_{k-1} \bar{\tilde{\boldsymbol{x}}}_{k-1} - \boldsymbol{\omega}_{d,k-1} \right)}_{\text{error}}.$$

The covariance matrix of the a-priori estimate can then be written as

$$\begin{aligned}
\boldsymbol{Y}_k^* &= E\left\{ \left(\tilde{\boldsymbol{x}}_k^* - \tilde{\boldsymbol{x}}_k \right) \left(\tilde{\boldsymbol{x}}_k^* - \tilde{\boldsymbol{x}}_k \right)^T \right\} \\
&= E\left\{ \left(\boldsymbol{\Phi}_{k-1} \bar{\tilde{\boldsymbol{x}}}_{k-1} + \boldsymbol{\omega}_{d,k-1} \right) \left(\boldsymbol{\Phi}_{k-1} \bar{\tilde{\boldsymbol{x}}}_{k-1} + \boldsymbol{\omega}_{d,k-1} \right)^T \right\} \\
&= E\left\{ \left(\boldsymbol{\Phi}_{k-1} \bar{\tilde{\boldsymbol{x}}}_{k-1} + \boldsymbol{\omega}_{d,k-1} \right) \left(\bar{\tilde{\boldsymbol{x}}}_{k-1}^T \boldsymbol{\Phi}_{k-1}^T + \boldsymbol{\omega}_{d,k-1}^T \right) \right\} \\
&= E\left\{ \boldsymbol{\Phi}_{k-1} \bar{\tilde{\boldsymbol{x}}}_{k-1} \bar{\tilde{\boldsymbol{x}}}_{k-1}^T \boldsymbol{\Phi}_{k-1}^T + \boldsymbol{\omega}_{d,k-1} \bar{\tilde{\boldsymbol{x}}}_{k-1}^T \boldsymbol{\Phi}_{k-1}^T + \boldsymbol{\Phi}_{k-1} \bar{\tilde{\boldsymbol{x}}}_{k-1} \boldsymbol{\omega}_{d,k-1}^T + \boldsymbol{\omega}_{d,k-1} \boldsymbol{\omega}_{d,k-1}^T \right\} \\
&= E\left\{ \boldsymbol{\Phi}_{k-1} \bar{\tilde{\boldsymbol{x}}}_{k-1} \bar{\tilde{\boldsymbol{x}}}_{k-1}^T \boldsymbol{\Phi}_{k-1}^T \right\} + E\left\{ \boldsymbol{\omega}_{d,k-1} \bar{\tilde{\boldsymbol{x}}}_{k-1}^T \boldsymbol{\Phi}_{k-1}^T \right\} \\
&\quad + E\left\{ \boldsymbol{\Phi}_{k-1} \bar{\tilde{\boldsymbol{x}}}_{k-1} \boldsymbol{\omega}_{d,k-1}^T \right\} + E\left\{ \boldsymbol{\omega}_{d,k-1} \boldsymbol{\omega}_{d,k-1}^T \right\}.
\end{aligned} \tag{2.85}$$

Since $\boldsymbol{\Phi}_{k-1}$ is not considered as a stochastic quantity, it can be extracted from the expectation value and thus it results

$$\begin{aligned}
\boldsymbol{Y}_k^* = {} & \boldsymbol{\Phi}_{k-1} E\left\{ \bar{\tilde{\boldsymbol{x}}}_{k-1} \bar{\tilde{\boldsymbol{x}}}_{k-1}^T \right\} \boldsymbol{\Phi}_{k-1}^T + E\left\{ \boldsymbol{\omega}_{d,k-1} \bar{\tilde{\boldsymbol{x}}}_{k-1}^T \right\} \boldsymbol{\Phi}_{k-1}^T \\
& + \boldsymbol{\Phi}_{k-1} E\left\{ \bar{\tilde{\boldsymbol{x}}}_{k-1} \boldsymbol{\omega}_{d,k-1}^T \right\} + E\left\{ \boldsymbol{\omega}_{d,k-1} \boldsymbol{\omega}_{d,k-1}^T \right\}.
\end{aligned}$$

Due to the above-mentioned considerations that the process noise is caused by the D/A converter, it can also be assumed that the process noise and the estimation error are uncorrelated.

Thus, the calculation of the covariance matrix of the a-priori estimation error simplifies to

$$\boldsymbol{Y}_k^* = \boldsymbol{\Phi}_{k-1} \underbrace{E\left\{\bar{\tilde{\boldsymbol{x}}}_{k-1}\bar{\tilde{\boldsymbol{x}}}_{k-1}^T\right\}}_{=\,\boldsymbol{Y}_k} \boldsymbol{\Phi}_{k-1}^T + E\left\{\boldsymbol{\omega}_{d,k-1}\boldsymbol{\omega}_{d,k-1}^T\right\}$$

and one obtains the second Kalman filter equation, where $\boldsymbol{W}_{o,k} = E\{\boldsymbol{\omega}_{d,k}, \boldsymbol{\omega}_{d,k}^T\}$ is the covariance matrix of the process noise.

Equations three to five can be derived in the sense of calculating the minimal variance of the estimation error. The variance of the measurement noise is denoted by $v_o = E\{\omega_{n,k}^2\}$. For the calculation of the covariance matrix of the estimation error, various forms are known in the literature. The one used here is called "Joseph form" [Grewal and Andrews, 2001].

For the beginning of the recursion of the Kalman equations, the initial conditions for the a priori estimation error as well as its covariance matrix are needed. Note that the a-priori estimation error does not take into account the current value of the output. Thus, for the a priori estimation error, the expectation value of the initial state can also be used for the beginning of the recursion, i.e.

$$\tilde{\boldsymbol{x}}_0^* = E\{\tilde{\boldsymbol{x}}_0\} = \boldsymbol{m}_0. \tag{2.86}$$

This results in the initial value of the covariance matrix of the a-priori estimation error as

$$\begin{aligned} \boldsymbol{Y}_0^* &= E\left\{\left(\tilde{\boldsymbol{x}}_0^* - \tilde{\boldsymbol{x}}_0\right)\left(\tilde{\boldsymbol{x}}_0^* - \tilde{\boldsymbol{x}}_0\right)^T\right\} \\ &= E\left\{\left(\boldsymbol{m}_0 - \tilde{\boldsymbol{x}}_0\right)\left(\boldsymbol{m}_0 - \tilde{\boldsymbol{x}}_0\right)^T\right\} = \boldsymbol{M}_0. \end{aligned} \tag{2.87}$$

2.4.8.1 Covariance matrix of the process noise

The process noise is assumed to exclusively stem from the D/A converter acting at the system input as depicted in Figure 2.21, i.e. the quantization noise $\bar{\boldsymbol{\omega}}_{d,k}$ has to be transformed to the system output. Due to the augmentation of the system model introduced in Section 2.4.1 to get an estimate for the total emissivity of the wafer, the last row of $\boldsymbol{H}_k$ consists of zeros, i.e. the input matrix can be decomposed into two parts

$$\boldsymbol{H}_k = \begin{bmatrix} \boldsymbol{H}_{1,k} \\ \boldsymbol{0}^T \end{bmatrix}. \tag{2.88}$$

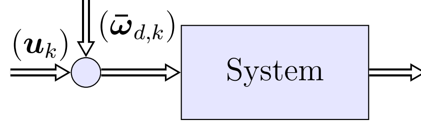

Figure 2.21: Input noise due to digital to analogue converter

With

$$\begin{aligned}\tilde{\boldsymbol{x}}_{k+1} &= \boldsymbol{\Phi}_k \tilde{\boldsymbol{x}}_k + \boldsymbol{H}_k(\boldsymbol{u}_k + \bar{\boldsymbol{\omega}}_{d,k}) + \boldsymbol{h}_k \\ &= \boldsymbol{\Phi}_k \tilde{\boldsymbol{x}}_k + \boldsymbol{H}_k \boldsymbol{u}_k + \boldsymbol{h}_k + \underbrace{\boldsymbol{H}_k \bar{\boldsymbol{\omega}}_{d,k}}_{= \, \boldsymbol{\omega}_{d,k}}\end{aligned} \tag{2.89}$$

and in accordance to the decomposition of the input matrix we can define

$$\boldsymbol{\omega}_{d,1,k} := \boldsymbol{H}_{1,k} \bar{\boldsymbol{\omega}}_{d,k}. \tag{2.90}$$

The covariance matrix of the quantization noise with respect to the original input matrix $\boldsymbol{H}_{1,k}$, which is transferred to the system output, then calculates as

$$\begin{aligned}\boldsymbol{W}_{o,1,k} &= E\{\boldsymbol{\omega}_{d,1,k} \boldsymbol{\omega}_{d,1,k}^T\} \\ &= \boldsymbol{H}_{1,k} \underbrace{E\{\bar{\boldsymbol{\omega}}_{d,k} \bar{\boldsymbol{\omega}}_{d,k}^T\}}_{=: \, \overline{\boldsymbol{W}}_o} \boldsymbol{H}_{k,1}^T = \boldsymbol{H}_{1,k} \overline{\boldsymbol{W}}_o \boldsymbol{H}_{1,k}^T.\end{aligned} \tag{2.91}$$

A suitable choice for the overall covariance matrix of the process noise can finally be stated as

$$\boldsymbol{W}_{o,k} = \begin{bmatrix} \boldsymbol{W}_{o,1,k} & \boldsymbol{0} \\ \boldsymbol{0}^T & \sigma_\varepsilon^2 \end{bmatrix}, \tag{2.92}$$

where the parameter σ_ε weights the estimate for the total emissivity. Since this parameter does not rely on stochastic properties, its value is found with the help of numerical simulations as 0.03.

From (2.92) it can be concluded that although the quantization is treated as a stationary stochastic process, the covariance matrix of the process noise is time-variant, since $\boldsymbol{W}_{o,1,k}$ is calculated as a function of the time-varying input matrix.

To obtain the values for the covariance matrix of the quantization noise $\overline{\boldsymbol{W}}_o$, the D/A converter for the electrical power signal to the four heating zones is considered. The converter has a resolution of 12 bit and the output range is given as 0 to 4.3 W. Thus, the least significant bit of the power signal (LSB_P) calculates as

$$LSB_P = \frac{4.3}{2^{12}}. \tag{2.93}$$

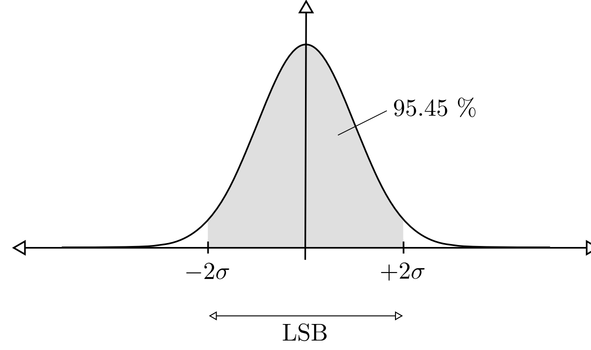

Figure 2.22: Gaussian distribution, D/A converter: The standard deviation of a D/A converted signal is estimated by treating the latter as a Gaussian distributed random variable.

It is well known that a Gaussian distributed random variable with standard deviation σ lies in the interval from -2σ to $+2\sigma$ in more than 95% of cases, like illustrated in Figure 2.22. Thus, it is reasonable to conclude that one LSB_P corresponds to approximately four times the standard deviation, i.e.

$$\sigma_P = \frac{LSB_P}{4}. \tag{2.94}$$

With the knowledge of σ_P, the covariance matrix of the quantization noise can be stated as

$$\overline{\boldsymbol{W}}_o = \begin{bmatrix} \sigma_P^2 & & & & 0 \\ & \sigma_P^2 & & & \\ & & \sigma_P^2 & & \\ & & & \sigma_P^2 & \\ 0 & & & & 0 \end{bmatrix}. \tag{2.95}$$

Please note that the lower right zero corresponds to the variance of the ambient temperature, which is not measured, but constantly set to room temperature.

2.4.8.2 Variance of the measurement noise

The standard deviation of the measurement noise can be determined similar to the choice of the standard deviation of the quantization noise. Referring to the data sheet of the used pyrometer, its measuring tolerance is given as $\pm 1°C$, which is assumed to correspond to four times the standard deviation, i.e.

$$2°C \mathrel{\widehat{=}} 4\sigma_M. \tag{2.96}$$

Accordingly, the variance of the measurement noise reads as

$$v_o = \sigma_M^2 = 0.5^2 = 0.25. \tag{2.97}$$

2.4.8.3 Initial covariance matrix of the a priori estimation error

The covariance matrix of the a priori estimation error at $k = 0$ can be determined by considering probable initial values for $\tilde{\boldsymbol{x}}_k$. It can be assumed that $\tilde{\boldsymbol{x}}_k$ is uniformly distributed and the initial wafer's temperature lies in the range of 20 to 40°C (293.15 to 313.15 K). The total emissivity of the wafer can lie in the whole range of 0.2 to 0.9. According to Appendix E, the standard deviation of the ith element of $\boldsymbol{x}_0$, i.e. $x_{i,0}$, calculates as

$$\sigma_{x_{i,0}} = \frac{20}{\sqrt{12}}. \tag{2.98}$$

The standard deviation of the emissivity at $k = 0$ is given as

$$\sigma_{\varepsilon_0} = \frac{0.7}{\sqrt{12}}. \tag{2.99}$$

Thus, a suitable choice for $\boldsymbol{M}_0$ is

$$\boldsymbol{M}_0 = \begin{bmatrix} \sigma^2_{x_{i,0}} & & & 0 \\ & \ddots & & \\ & & \sigma^2_{x_{i,0}} & \\ 0 & & & \sigma^2_{\varepsilon_0} \end{bmatrix} = \begin{bmatrix} \frac{20^2}{12} & & & 0 \\ & \ddots & & \\ & & \frac{20^2}{12} & \\ 0 & & & \frac{0.7^2}{12} \end{bmatrix}. \tag{2.100}$$

2.4.8.4 Laboratory experiments

The derived Kalman filter is tested with the same experiment introduced in Section 2.4.7. As Figure 2.23 points out, the Kalman filter shows comparably accurate results as the Luenberger observer designed in Section 2.4.5. The advantage of the Kalman filter lies in the structured calculation of the covariance matrix of the process noise and the variance of the measurement noise instead of choosing weighting parameters.

Figure 2.24 also shows that the estimated emissivity again tends to value of approximately 0.8. It is also conspicuous that during the heat-up phase, where the pyrometer reading is not reliable, the emissivity cannot be estimated correctly. One possible solution to avoid a wrong emissivity estimation during the heat-up phase could be to pause the latter until a certain wafer temperature is reached, but this approach has not been pursued in this work.

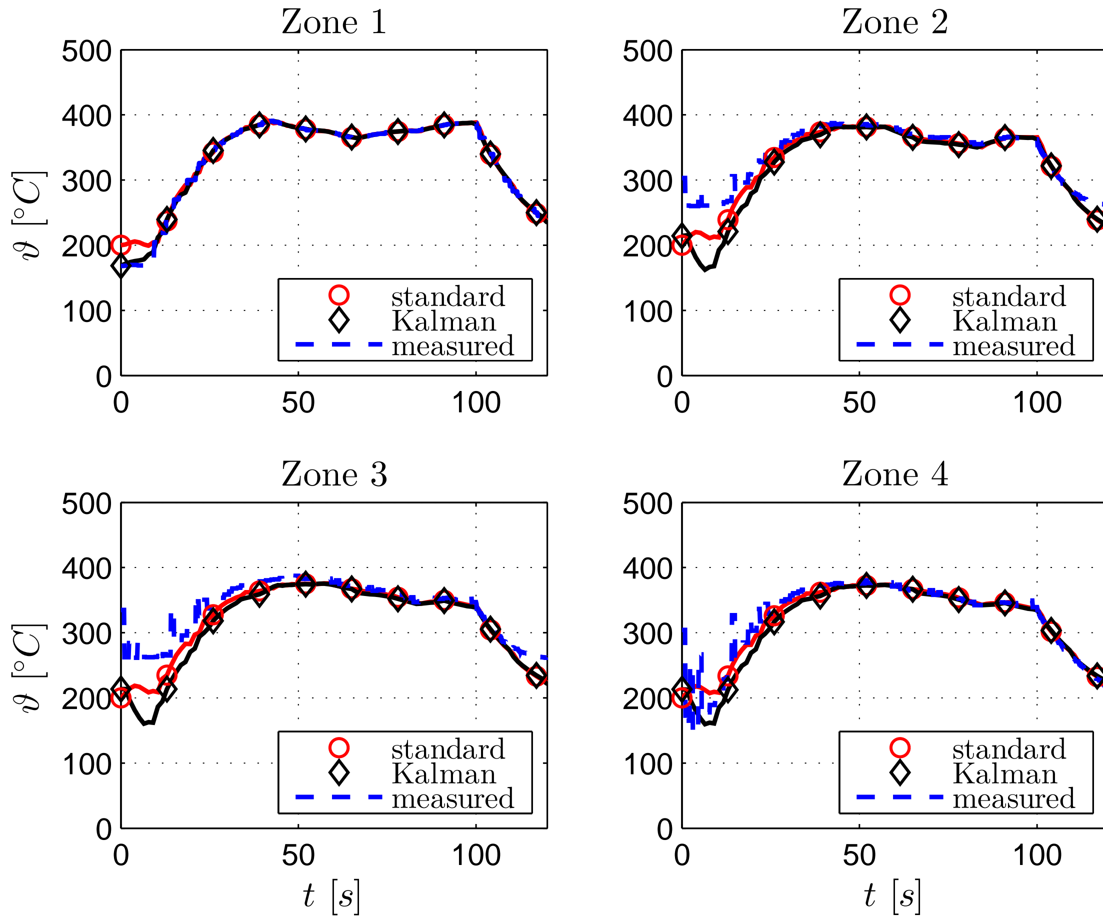

Figure 2.23: Measured and estimated output, "highly doped" wafer, Kalman filter: The observer designed in Section 2.4.5 is compared to a Kalman filter. The plots show that both observer types provide accurate results.

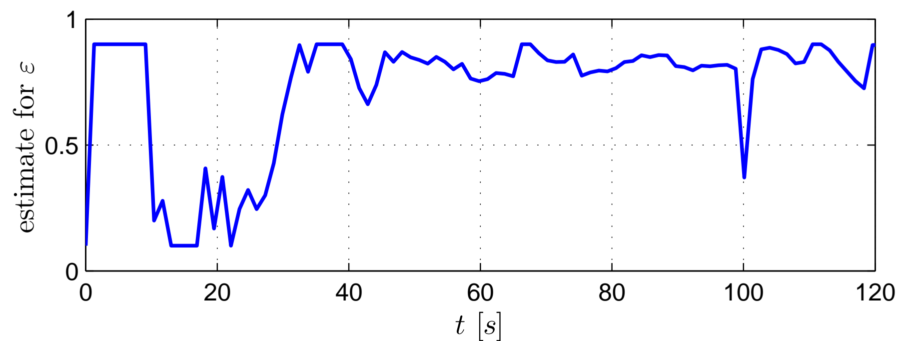

Figure 2.24: Estimated emissivity, "highly doped" wafer, Kalman filter: The Kalman filter also provides a feasible estimate for the total emissivity of the processed "highly doped" silicon wafer.

2.5 Observers based on the late-lumping approach

The design of observers for distributed parameter systems can be carried out by either using so-called early-lumping or late-lumping techniques [Meurer, 2013; Schlake and Konigorski, 2009]. The observer design discussed in Section 2.4 belongs to the first category, which means that the partial differential system is discretized in space in order to obtain a finite-dimensional set of nonlinear, ordinary differential equations.

The nonlinear system is then linearized around the estimated state vector, which leads to a time-varying linear system. To compute the observer gain, an optimization problem is solved iteratively. Due to the fact that the derived linear system is of high order, the computational effort to solve the optimization problem is significant and the implementation at production tools requires powerful programmable controllers.

To reduce the computational effort, an observer approach based on the late-lumping technique, which directly deals with the partial differential equation, is discussed. The procedure proposed in [Schaum, Moreno, Alvarez, and Meurer, 2015] is extended and applied to the present application. The starting point is the quasilinear one-dimensional partial differential heat equation (2.9) in cylindrical coordinates with heat sources and losses

$$\partial_t T(r,t) = \kappa(T)\left[\partial_{rr} T(r,t) + \frac{1}{r}\partial_r T(r,t)\right] + \underbrace{\frac{q(r,t)}{\rho c_p(T)}}_{=:\,\mu(T)} \tag{2.101}$$

with the notation

$$\partial_t := \frac{\partial}{\partial t}\ , \quad \partial_r := \frac{\partial}{\partial r} \quad \text{and} \quad \partial_{rr} := \frac{\partial^2}{\partial r^2}\ . \tag{2.102}$$

The nonlinear function $\mu(T)$ involves the heat input due to light absorption as well as heat losses due to convection and radiation. Neumann boundary conditions are introduced in Section 2.2.3 as

$$\partial_r T(r,t)\Big|_{r=0} = \partial_r T(r,t)\Big|_{r=R} = 0. \tag{2.103}$$

The temperature measured by the pyrometer at radius $r = \zeta$ is denoted by

$$y(t) = T(\zeta, t). \tag{2.104}$$

By introducing the operators

$$\mathcal{A}(T) := \kappa(T)\left[\partial_{rr} + \frac{1}{r}\partial_r\right], \quad \mathcal{B}_0 := \partial_r\Big|_{r=0}, \quad \mathcal{B}_R := \partial_r\Big|_{r=R} \tag{2.105}$$

and

$$\mathcal{C}T(r,t) := \int_0^R \delta(r-\zeta)T(r,t)\,\mathrm{d}r = T(\zeta,t), \tag{2.106}$$

where δ denotes the Dirac delta operator, system (2.101) with boundary conditions (2.103) can compactly be written as

$$\begin{aligned} \partial_t T(r,t) &= \mathcal{A}(T)T(r,t) + \mu(T), \\ \mathcal{B}_0 T(r,t) &= \mathcal{B}_R T(r,t) = 0, \\ \mathcal{C}T(r,t) &= y(t). \end{aligned} \tag{2.107}$$

2.5.1 Late-lumping approach

Based upon the theory presented by Schaum, Moreno, Alvarez, and Meurer, an observer for the system described by (2.107) can be stated as

$$\begin{aligned} \partial_t \hat{T}(r,t) &= \mathcal{A}(\hat{T})\hat{T}(r,t) + \mu(\hat{T}), \\ \mathcal{B}_0 \hat{T}(r,t) &= \mathcal{B}_R \hat{T}(r,t) = 0, \\ \mathcal{C}\hat{T}(r,t) &\overset{!}{=} y(t), \end{aligned} \tag{2.108}$$

with $\hat{T}(r,t)$ denoting the estimated temperature of the wafer. The additional Dirichlet boundary condition

$$\hat{T}(\zeta,t) \overset{!}{=} y(t) \tag{2.109}$$

states that the estimated temperature at the sensor position is fixed to the measured value.

In contrast to the problem outlined in the mentioned paper, the operator $\mathcal{A}$ here depends on the unknown function $\hat{T}(r,t)$ and thus, the given proof of the observer convergence does not fit to the problem at hand. A new proof is discussed later on.

The main idea of the design approach is to divide the observer (2.108) into two subsystems with the additional Dirichlet boundary condition at the sensor position. The two subsystems then read as

$$\begin{aligned} \partial_t \hat{T}_1(r,t) &= \mathcal{A}_1 \hat{T}_1(r,t) + \mu(\hat{T}_1), \\ \partial_t \hat{T}_2(r,t) &= \mathcal{A}_2 \hat{T}_2(r,t) + \mu(\hat{T}_2), \\ \mathcal{B}_0 \hat{T}_1(r,t) &= \mathcal{B}_R \hat{T}_2(r,t) = 0, \\ \mathcal{C}\hat{T}_1(r,t) &= \mathcal{C}\hat{T}_2(r,t) = y(t), \end{aligned} \tag{2.110}$$

with

$$\mathcal{A}_1 := \mathcal{A}(\hat{T}_1),\ \mathcal{A}_2 := \mathcal{A}(\hat{T}_2).$$

The state estimate is given by

$$\hat{T}(r,t) = \begin{cases} \hat{T}_1(r,t), & r \in [0,\zeta) \\ y(t), & r = \zeta \\ \hat{T}_2(r,t), & r \in (\zeta, R] \end{cases}. \tag{2.111}$$

For the implementation of the observer on the laboratory system, a spatial discretization as described in Section 2.2, as well as a time discretization, is applied to the two subsystems (2.110). Due to the additional Dirichlet boundary condition, the estimated temperature at the sensor position is fixed by the value of the pyrometer reading. The remaining temperature profile is estimated by solving the two obtained sets of difference equations at the programmable logic controller.

2.5.1.1 Proof of convergence

A mathematical proof for the convergence of the late-lumping observer (2.110), given by Schaum, Moreno, and Meurer (2017), is discussed in the following. The idea of the proof is to write the error dynamics in a compact form, which is similar to the introduced heat equation (2.9). Based on that, a Lyapunov function is chosen, which enables to derive a set of sufficient conditions to prove the convergence of the observer.

To start with, the estimation error is introduced as

$$e(r,t) = \hat{T}(r,t) - T(r,t). \tag{2.112}$$

Recalling the introduced plant model (2.101) with the observer (2.108) allows to calculate the error dynamics as

$$\begin{aligned} \partial_t e(r,t) &= \mathcal{A}(\hat{T})\hat{T}(r,t) + \mu(\hat{T}) - \mathcal{A}(T)T(r,t) - \mu(T) \\ &= \kappa(T+e)\left[\partial_{rr}T(r,t) + \partial_{rr}e(r,t) + \frac{1}{r}\partial_r T(r,t) + \frac{1}{r}\partial_r e(r,t)\right] \\ &\quad + \mu(T+e) - \kappa(T)\left[\partial_{rr}T(r,t) + \frac{1}{r}\partial_r T(r,t)\right] - \mu(T), \\ \partial_r e(0,t) &= \partial_r e(R,t) = 0, \\ e(\zeta,t) &= 0. \end{aligned} \tag{2.113}$$

Rearranging (2.113) yields

$$\begin{aligned} \partial_t e(r,t) &= [\kappa(T+e)-\kappa(T)]\left[\partial_{rr}T(r,t)+\frac{1}{r}\partial_r T(r,t)\right] \\ &\quad + \kappa(T+e)\left[\partial_{rr}e(r,t)+\frac{1}{r}\partial_r e(r,t)\right]+\mu(T+e)-\mu(T), \\ \partial_r e(0,t) &= \partial_r e(R,t) = 0, \\ e(\zeta,t) &= 0. \end{aligned} \tag{2.114}$$

This enables to introduce

$$\begin{aligned} \Delta\kappa(e,r,t) &:= \kappa(T+e)-\kappa(T), \\ \Delta\mu(e,r,t) &:= \mu(T+e)-\mu(T), \\ \alpha(T) &:= \partial_{rr}T(r,t)+\frac{1}{r}\partial_r T(r,t) \end{aligned} \tag{2.115}$$

and

$$\phi(e,r,t) := \Delta\kappa(e,r,t)\alpha(T)+\Delta\mu(e,r,t), \tag{2.116}$$

which allows to write the error dynamics in the compact form

$$\begin{aligned} \partial_t e(r,t) &= \kappa(\hat{T})\left[\partial_{rr}e(r,t)+\frac{1}{r}\partial_r e(r,t)\right]+\phi(e,r,t), \\ \partial_r e(0,t) &= \partial_r e(R,t) = 0, \\ e(\zeta,t) &= 0. \end{aligned} \tag{2.117}$$

Further rewriting (2.117) yields

$$\begin{aligned} \partial_t e(r,t) &= \hat{\kappa}\frac{1}{r}\partial_r\left[r\partial_r e(r,t)\right]+\phi(e,r,t), \\ \partial_r e(0,t) &= \partial_r e(R,t) = 0, \\ e(\zeta,t) &= 0, \end{aligned} \tag{2.118}$$

with

$$\hat{\kappa} := \kappa(\hat{T}). \tag{2.119}$$

Assuming the Lipschitz uniformity of $\phi(e,r,t)$ in space and time with Lipschitz constant L, it can be expected that

$$e(r,t)\phi(e,r,t) \le Le^2(r,t), \quad \forall e,r,t. \tag{2.120}$$

The Lyapunov function

$$V(e) = \frac{1}{2}\int_0^R w(r)e^2(r,t)dr \tag{2.121}$$

with the weighting function

$$0 \leq w(r), \quad \forall r \in [0,R] \tag{2.122}$$

is used as a candidate to show the asymptotic convergence of the estimation error. The rate of change over time of (2.121) is given by[12]

$$\frac{dV}{dt} = \int_0^R we\partial_t e dr = \int_0^R \left[we\left(\hat{\kappa}\frac{1}{r}\partial_r(r\partial_r e)\right) + we\phi\right] dr. \tag{2.123}$$

Applying integration by parts leads to

$$\frac{dV}{dt} = [w\hat{\kappa}e\partial_r e]_0^R - \int_0^R \left[\partial_r\left(w\hat{\kappa}e\frac{1}{r}\right) r\partial_r e - we\phi\right] dr. \tag{2.124}$$

With

$$\partial_r\left(w\hat{\kappa}e\frac{1}{r}\right) r\partial_r e = w\hat{\kappa}\left(\partial_r e\right)^2 + \partial_r\left(w\hat{\kappa}\frac{1}{r}\right) re\partial_r e \tag{2.125}$$

and inserting the boundary conditions

$$\partial_r e(0,t) = \partial_r e(R,t) = 0 \tag{2.126}$$

into (2.124), the latter reads as

$$\frac{dV}{dt} = -\int_0^R w\hat{\kappa}\left(\partial_r e\right)^2 dr - \int_0^R \partial_r\left(w\hat{\kappa}\frac{1}{r}\right) re\partial_r e dr + \int_0^R we\phi dr. \tag{2.127}$$

By taking into account condition (2.120) and assuming that there exist a constant

$$0 \leq \underline{w\hat{\kappa}} \leq w\hat{\kappa}, \quad \forall t \geq 0,\ r \in [0,R] \tag{2.128}$$

it follows that

$$\frac{dV}{dt} \leq -\underline{w\hat{\kappa}}\int_0^R \left(\partial_r e\right)^2 dr - \int_0^R \partial_r\left(w\hat{\kappa}\frac{1}{r}\right) re\partial_r e dr + \int_0^R wLe^2 dr. \tag{2.129}$$

[12]Arguments are skipped occasionally for the sake of readability.

Applying the so-called "Wirtinger inequality" [Hardy, Littlewood, and Pólya, 1952] to

$$-\underline{w\hat{\kappa}}\int_0^R (\partial_r e)^2\, dr = -\underline{w\hat{\kappa}}\left[\int_0^\zeta (\partial_r e)^2\, dr + \int_\zeta^R (\partial_r e)^2\, dr\right] \tag{2.130}$$

leads to

$$\begin{aligned}-\underline{w\hat{\kappa}}\int_0^R (\partial_r e)^2\, dr &\leq -\underline{w\hat{\kappa}}\left[\frac{\pi^2}{4\zeta^2}\int_0^\zeta e^2 dr + \frac{\pi^2}{4(R-\zeta)^2}\int_\zeta^R e^2 dr\right] \\ &\leq -\frac{\underline{w\hat{\kappa}}\pi^2}{4}\min\left\{\frac{1}{\zeta^2}, \frac{1}{(R-\zeta)^2}\right\}\int_0^R e^2 dr.\end{aligned} \tag{2.131}$$

By inserting (2.131) into (2.129) one arrives at

$$\begin{aligned}\frac{dV}{dt} \leq &-\frac{\underline{w\hat{\kappa}}\pi^2}{4}\min\left\{\frac{1}{\zeta^2}, \frac{1}{(R-\zeta)^2}\right\}\int_0^R e^2 dr \\ &-\int_0^R \partial_r\left(w\hat{\kappa}\frac{1}{r}\right) re\partial_r e dr + \int_0^R wLe^2 dr.\end{aligned} \tag{2.132}$$

Again, partially integrating

$$-\int_0^R \partial_r\left(w\hat{\kappa}\frac{1}{r}\right) re\partial_r e dr = -\int_0^R \partial_r\left(w\hat{\kappa}\frac{1}{r}\right)\frac{r}{2}\partial_r\left(e^2\right) dr \tag{2.133}$$

results

$$-\int_0^R \partial_r\left(w\hat{\kappa}\frac{1}{r}\right) re\partial_r e dr = \left[-\partial_r\left(w\hat{\kappa}\frac{1}{r}\right)\frac{r}{2}e^2\right]_0^R + \int_0^R \partial_r\left[\frac{r}{2}\partial_r\left(w\hat{\kappa}\frac{1}{r}\right)\right] e^2 dr. \tag{2.134}$$

With (2.134) an inequality for the rate of change over time of V can finally stated as

$$\begin{aligned}\frac{dV}{dt} \leq &\left[-\partial_r\left(w\hat{\kappa}\frac{1}{r}\right)\frac{r}{2}e^2\right]_0^R \\ &-\int_0^R e^2\left\{\frac{\underline{w\hat{\kappa}}\pi^2}{4}\min\left\{\frac{1}{\zeta^2}, \frac{1}{(R-\zeta)^2}\right\} - \partial_r\left[\frac{r}{2}\partial_r\left(w\hat{\kappa}\frac{1}{r}\right)\right] - wL\right\} dr.\end{aligned} \tag{2.135}$$

Thus, it can be concluded that the estimation error converges exponentially to zero with rate $\gamma > 0$, if the sensor position ζ is chosen such that there exists a positive function $w(r)$ for which the following conditions hold:

$$\begin{aligned}&(i) \quad \left[-\partial_r\left(w\hat{\kappa}\frac{1}{r}\right)\frac{r}{2}e^2\right]_0^R \leq 0, \\ &(ii) \quad \frac{\underline{w\hat{\kappa}}\pi^2}{4}\min\left\{\frac{1}{\zeta^2}, \frac{1}{(R-\zeta)^2}\right\} - \partial_r\left[\frac{r}{2}\partial_r\left(w\hat{\kappa}\frac{1}{r}\right)\right] - wL \geq \gamma\end{aligned} \tag{2.136}$$

The presented convergence assessment provides two sufficient conditions, which indicate that the stability of the observer can be proven in case a suitable weighting function for the used position of the sensor is chosen. Unfortunately, such a function was not found for the given position. On the other hand, this does not mean that the latter does not exist. With this in mind, the derived convergence criterion may be nonetheless considered as a proof for the stability of the observer, showing that this approach in principle could work. Moreover, the used model is affected by uncertainties. Thus, the final verification of the functionality of the observer can anyway only be checked with its implementation at the real world system.

2.5.2 Late-lumping approach with measurement injection

The dynamics of the observer (2.110) are fixed by the choice of the sensor location and the given plant characteristics. Approaches to additionally tune the observer dynamics have already been considered in the literature. The observation problem addressed in [Schaum, Moreno, Fridman, et al., 2014], for example, deals with the injection of the measurements at the system boundaries. More precisely, the difference between the measurement and its estimate is weighted similarly to a Luenberger observer.

This method of measurement injection cannot be adopted to (2.110), since the difference between the in-domain measurement $y(t)$ and its estimate $\hat{y}(t) = \hat{T}(r,t)|_{r=\zeta}$ is equal to zero due to the introduced Dirichlet boundary condition at the sensor position and (2.111) respectively. To nevertheless introduce a measurement injection, the idea is to make use of an additional estimate $\tilde{y}(t)$ and to extend the observer as

$$\begin{aligned}
\partial_t \hat{T}_1(r,t) &= \mathcal{A}_1 \hat{T}_1(r,t) + \mu(\hat{T}_1) - l(r)\left[\tilde{y}(t) - y(t)\right], \\
\partial_t \hat{T}_2(r,t) &= \mathcal{A}_2 \hat{T}_2(r,t) + \mu(\hat{T}_2) - l(r)\left[\tilde{y}(t) - y(t)\right], \\
\mathcal{B}_0 \hat{T}_1(r,t) &= \mathcal{B}_R \hat{T}_2(r,t) = 0, \\
\mathcal{C} \hat{T}_1(r,t) &= \mathcal{C} \hat{T}_2(r,t) = y(t),
\end{aligned} \tag{2.137}$$

with the weighting function $l(r)$. The state estimate is again given by

$$\hat{T}(r,t) = \begin{cases} \hat{T}_1(r,t), & r \in [0,\zeta) \\ y(t), & r = \zeta \\ \hat{T}_2(r,t), & r \in (\zeta, R] \end{cases}. \tag{2.138}$$

For the estimate $\tilde{y}(t)$, the system model (2.101) is considered at the sensor position and

fed with the estimated temperatures provided by (2.137) for $r \neq \zeta$, i.e.

$$\begin{aligned} \partial_t \tilde{y}(t) &= \partial_t T(r,t) \Big|_{r=\zeta;\ T(r,t)=\begin{cases} \tilde{y}(t), & r=\zeta \\ \hat{T}(r,t), & r\neq\zeta \end{cases}} \\ &= \left[\mathcal{A}(T)T(r,t) + \mu(T)\right] \Big|_{r=\zeta;\ T(r,t)=\begin{cases} \tilde{y}(t), & r=\zeta \\ \hat{T}(r,t), & r\neq\zeta \end{cases}} . \end{aligned} \tag{2.139}$$

Considering the finite-dimensional implementation of (2.139) based on the approximation of the spatial derivatives by difference equations outlined in Section 2.2 and dropping time dependencies yield

$$\dot{\tilde{y}} = a_{1,i_\zeta,i_\zeta-1}(\tilde{y})\hat{x}_{i_\zeta-1} + a_{1,i_\zeta,i_\zeta}(\tilde{y})\tilde{y} + a_{1,i_\zeta,i_\zeta+1}(\tilde{y})\hat{x}_{i_\zeta+1} - \varepsilon a_{2,i_\zeta,i_\zeta}(\tilde{y})\tilde{y}^4 + \boldsymbol{b}_{i_\zeta}^T(\tilde{y})\boldsymbol{u}, \tag{2.140}$$

where i_ζ is the index of the discretization point right at (or behind) the sensor position, i.e.

$$i_\zeta = \min\left(i \mid r_i \geq \zeta\right). \tag{2.141}$$

The factors $a_{1,i,j}$ and $a_{2,i,j}$ respectively denote the elements of the matrices $\boldsymbol{A}_1(\boldsymbol{x})$ and $\boldsymbol{A}_2(\boldsymbol{x})$ of the spatially lumped model (2.41) at row i and column j. The vector $\boldsymbol{b}_{i_\zeta}^T(\tilde{y})$ is the i_ζ-th row of $\boldsymbol{B}(\boldsymbol{x})$ and $\hat{x}_i$ are the estimated temperatures at radius $r = r_i$ provided by (2.137).

Please note that in case of a perfect plant model

$$\lim_{t\to\infty}(\tilde{y} - y) = 0 \tag{2.142}$$

holds and the wafer temperature can be estimated exactly.

2.5.2.1 Remarks on the stability

Although the experiments, which are discussed later on, will indicate the convergence of the designed late-lumping observer with measurement injection, its stability is not proven within this work. Nevertheless, some remarks are given in the following and possibly necessary preparations for future considerations are made.

To proof the convergence of infinite dimensional systems, different methods are known in the literature. Lyapunov based approaches, like applied in Section 2.5.1.1, are frequently

used for linear and nonlinear partial differential equations [Miranda et al., 2012; Ahmed-Ali, Giri, and Krstic, 2017; Schaum, Moreno, and Alvarez, 2008]. Another possibility to prove the stability of distributed parameter systems is based on the so-called semigroup theory, which may be applicable to the problem at hand. In reference to linear finite dimensional systems, where the stability can be characterized by the eigenvalues of the system matrix, this procedure can be expanded to infinite dimensional systems. Here it might be concluded from the spectrum of the associated linear differential operator on the asymptotic convergence of the system.

With a view to prove the convergence of the proposed observer, the eigenvalues of the introduced operators $\mathcal{A}_1$ and $\mathcal{A}_2$ are calculated in Appendix F.

2.5.3 Extension to estimate the wafer's total emissivity

As discussed in former sections, the total emissivity ε of the wafer is highly dependent on its dopant level and therefore on the wafer type. It directly affects the amount of heat loss due to radiation. Thus, its value is of particular importance for obtaining reasonable estimates of the wafer's temperature. Since the wafer type is not known a priori and the late-lumping observers are not capable of providing an estimate of the emissivity directly, an extension is introduced. Therefor, the derived physical, nonlinear, affine-input model (2.41) is reconsidered right at the sensor position, i.e. at a radius of $r = \zeta$. Due to the fact that the heat loss due to radiation and convection prevails, heat conduction is neglected for the estimation of the total emissivity. Thus, system (2.41) evaluated at the sensor position without considering heat conduction is given by

$$\dot{x}_{i_\zeta} = \frac{1}{\rho h c_p(x_{i_\zeta})} \left(-\alpha_{i_\zeta} x_{i_\zeta} - 2\varepsilon\sigma_{sb} x_{i_\zeta}^4 \right) + \boldsymbol{b}_{i_\zeta}^T(x_{i_\zeta})\boldsymbol{u}. \tag{2.143}$$

The constant α_{i_ζ} denotes the heat transfer coefficient at radius $r = \zeta$ and $\boldsymbol{b}_{i_\zeta}^T(x_{i_\zeta})$ is the i_ζ^{th} row of the input matrix $\boldsymbol{B}(\boldsymbol{x})$ derived in Section 2.2, which corresponds to the heat input at the sensor position.

To obtain an estimate for ε, different methods are conceivable. One possibility is based on sliding mode concepts. Rewriting equation (2.143) as

$$\dot{x}_{i_\zeta} = -\frac{\alpha_{i_\zeta}}{\rho h c_p(x_{i_\zeta})} x_{i_\zeta} - \frac{2\sigma_{sb} x_{i_\zeta}^4}{\rho h c_p(x_{i_\zeta})} \varepsilon + \boldsymbol{b}_{i_\zeta}^T(x_{i_\zeta})\boldsymbol{u} \tag{2.144}$$

isolates a term which includes the total emissivity. Following a copy of (2.144), a differential equation for the estimate of x_{i_ζ} can then be formulated as

$$\dot{\hat{x}}_{i_\zeta} = -\frac{\alpha_{i_\zeta}}{\rho h c_p(x_{i_\zeta})} x_{i_\zeta} + \boldsymbol{b}_{i_\zeta}^T(x_{i_\zeta})\boldsymbol{u} + \eta_{i_\zeta} \operatorname{sign} \underbrace{\left(x_{i_\zeta} - \hat{x}_{i_\zeta} \right)}_{=: e_{i_\zeta}}, \tag{2.145}$$

where the unknown term including ε is omitted and the sign function weighted by a tuning parameter η_{i_ς} is added. The difference between the measured temperature x_{i_ς} and its estimate is denoted by the estimation error e_{i_ς}, whose associated error dynamics is calculated as

$$\dot{e}_{i_\varsigma} = \dot{x}_{i_\varsigma} - \dot{\hat{x}}_{i_\varsigma} = \underbrace{-\frac{2\sigma_{sb} x_{i_\varsigma}^4}{\rho h c_p(x_{i_\varsigma})}\varepsilon}_{=:\,\Delta} - \eta_{i_\varsigma} \operatorname{sign}\left(e_{i_\varsigma}\right). \tag{2.146}$$

The term denoted by Δ is treated as an uncertainty, which is assumed to be bounded, i.e.

$$|\Delta| \leq \Delta_{max}. \tag{2.147}$$

Then it is easy to verify that e_{i_ς} converges to zero in finite time in case the tuning parameter η_{i_ς} is chosen such that

$$\eta_{i_\varsigma} > \Delta_{max} \tag{2.148}$$

holds. If so in steady state, i.e. $e_{i_\varsigma} = \dot{e}_{i_\varsigma} = 0$, it furthermore holds that

$$\eta_{i_\varsigma} \operatorname{sign}\left(e_{i_\varsigma}\right) = -\frac{2\sigma_{sb} x_{i_\varsigma}^4}{\rho h c_p(x_{i_\varsigma})}\varepsilon. \tag{2.149}$$

Please note that up to now all considerations are based on the assumption that the sign function can be operated in continuous time, i.e. with an infinitely high sampling frequency. This is clearly neither the case in practical applications, nor in numerical simulations. On the contrary, the present sampling interval causes the sign function to fluctuate with a high frequency. This phenomenon is well known in sliding mode control. Nevertheless, the low frequency components of the left-hand side of (2.149) can be used to estimate the total emissivity, i.e. the latter can be calculated as

$$\hat{\varepsilon} = -\frac{\rho h c_p(x_{i_\varsigma})}{2\sigma_{sb} x_{i_\varsigma}^4} \operatorname{lowpass}\left[\eta_{i_\varsigma} \operatorname{sign}\left(e_{i_\varsigma}\right)\right], \tag{2.150}$$

where lowpass $[\,\cdot\,]$ denotes the lowpass filtering of the considered signal.

2.5.3.1 Estimation of Δ_{max} and choice of η_{i_ς}

To estimate the upper bound of the uncertainty Δ, the physical minimal and maximal values listed in Table 2.4 are considered.

Physical parameter	Description	Value [unit]
$x_{i_\varsigma,max}$	Max. achievable temperature	673.15 $[K]$
ε_{max}	Max. total emissivity	0.9 [-]
$c_p(x_{i_\varsigma,min})$	Min. heat capacity (at 300 K)	703 $\left[\frac{J}{kgK}\right]$

Table 2.4: Minimal and maximal physical parameters

According to (2.146) and Table 2.4, an estimate for the upper bound of Δ computes as

$$\Delta_{max} \approx \left| -\frac{2\sigma_{sb} x_{i_\varsigma,max}^4}{\rho h c_p(x_{i_\varsigma,min})} \varepsilon_{max} \right| = 16.47. \tag{2.151}$$

Thus, choosing $\eta_{i_\varsigma} = 50$ should be sufficiently large in order to obtain reasonable estimates for the total emissivity.

2.5.4 Laboratory experiment

For the implementation, the two subsystems of the derived observers (2.110) and (2.137) respectively are discretized in space by means of the vertical method of lines discussed in Section 2.2.2. The entire radius is divided into 30 equidistant segments, where the temperature sensor is located above the eighth segment. Thus, the first subsystem is of order 7 and the second one is of order 22. The modelling of the heat input as well as the heat losses due to convection and radiation are as in Sections 2.2.4 and 2.2.5.

A direct comparison between the early-lumping and the late-lumping observers[13] is depicted in Figures 2.25 and 2.27. The comparison reveals that both late-lumping approaches provide feasible results after about 50 seconds. Furthermore, it indicates that both late-lumping observers provide a converging estimation error. The estimated temperatures of the late-lumping approach without measurement injection show a slight overshoot during the transient phase. By introducing the measurement injection, it is possible to overcome this effect and the performance of the late-lumping observer is identical to the early-lumping approach.

In addition, the estimate of the total emissivity, plotted in Figure 2.26, converges to a reasonable value for a “highly doped” wafer shortly after the used pyrometer provides reliable temperature readings.

[13]The weighting function of the late-lumping observer with measurement injection is chosen as $l(r) = 1.5$.

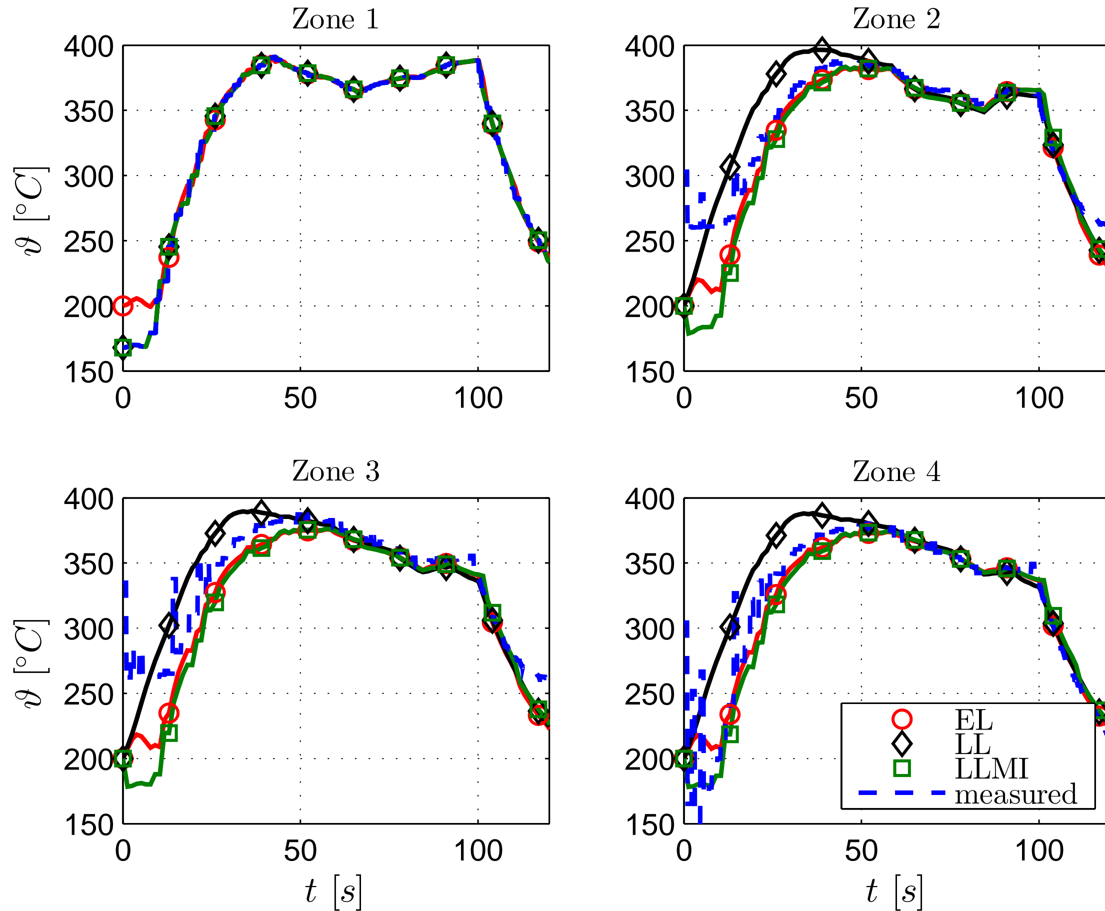

Figure 2.25: Measured and estimated zone temperatures: Comparison between early-lumping observer (EL), late-lumping observer without measurement injection (LL) and late-lumping observer with measurement injection (LLMI) for a "highly doped" wafer.

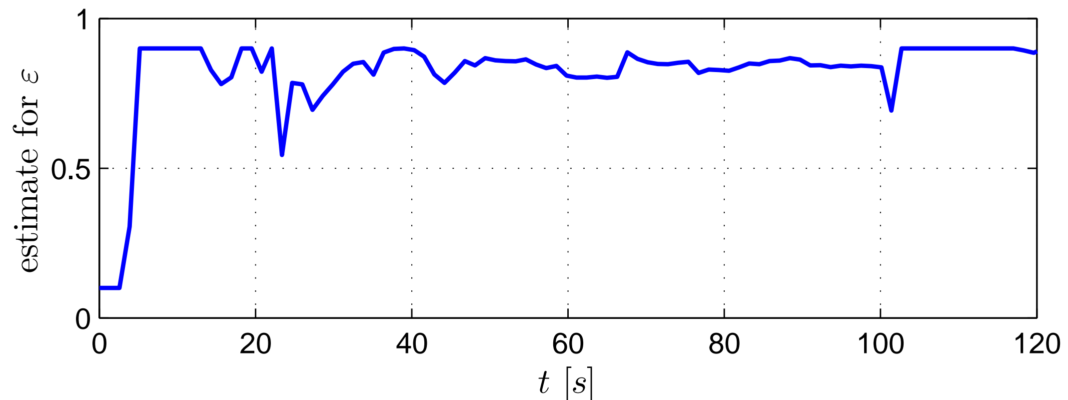

Figure 2.26: Estimated emissivity, "highly doped" wafer, late-lumping observer

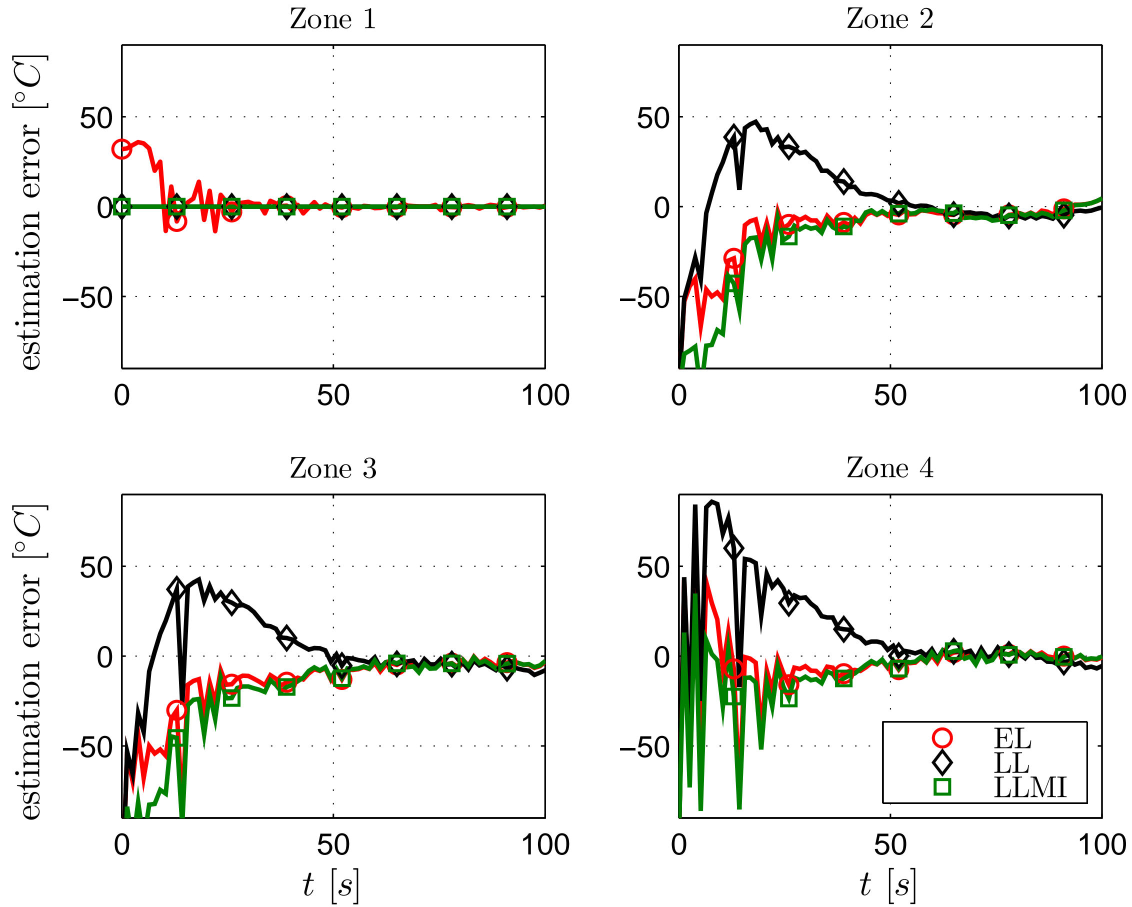

Figure 2.27: Estimation error: early-lumping observer (EL), late-lumping observer without measurement injection (LL) and late-lumping observer with measurement injection (LLMI)

2.5.5 Conclusion

It turned out that the late-lumping observer with measurement injection appears to have a performance comparable to the early-lumping observers designed in Section 2.4. The main advantage of this alternative approach is that there is no need to iteratively solve an optimization problem for a high-order system. This reveals a major benefit for the implementation of the observer at real world systems, where the computational power is limited. Thus, the use of the late-lumping observer with measurement injection is proposed.

2.6 Controller design

As described above, the wafer's surface should be heated to 300 to 400 $°C$ (573.15 to 673.15 K) by supplying the appropriate electrical power to the LEDs in the four heating zones. The temperature of the radial midpoint in each zone serves as the control variables. Only the temperature reading of the pyrometer, which is measuring in zone 1, is directly available for feedback. To control the temperature of the other zones, the intention is to use the estimated zone temperatures, which are provided by the observer designed in Section 2.5.2.

To ensure feasible temperature estimates, the designed observer relies on a precise time-varying mathematical model which incorporates temperature dependencies of parameters as well as a light absorption which is subject to the total emissivity of the wafer. In addition, the model is extended in order to estimate the total emissivity of the wafer. Such a precise model is not necessary for the design of the controller. Therefore, in contrast to the observer design addressed in Section 2.4, the nonlinear plant model (2.41) with the output equation (2.45) is linearized around a constant state vector, whose elements are equal to room temperature. The total emissivity is set to its maximal value of 0.9. This results a linear, time-invariant model instead of a time-varying one, since the linearization is carried out only once and not in every sampling instance. Subsequently, the linearized model is discretized in time which leads to

$$\begin{aligned} \boldsymbol{x}_{k+1} &= \boldsymbol{\Phi}\boldsymbol{x}_k + \boldsymbol{H}\boldsymbol{u}_k + \boldsymbol{h}, \\ \boldsymbol{y}_k &= \boldsymbol{C}\boldsymbol{x}_k. \end{aligned} \tag{2.152}$$

The input vector is composed of the electrical power per LED in the four zones as well as the ambient temperature. Since the latter represents an unmodifiable input, the input vector is formally split into two parts, i.e.

$$\boldsymbol{u}_k = \begin{bmatrix} \boldsymbol{u}_k^c \\ u_k^{\bar{c}} \end{bmatrix}, \tag{2.153}$$

where $\boldsymbol{u}_k^c$ denotes the changeable inputs and $u_k^{\bar{c}}$ the non-changeable part. The modified system then reads as

$$\begin{aligned} \boldsymbol{x}_{k+1} &= \boldsymbol{\Phi}\boldsymbol{x}_k + \boldsymbol{H}^c\boldsymbol{u}_k^c + \underbrace{\boldsymbol{h}^{\bar{c}}u_k^{\bar{c}} + \boldsymbol{h}}_{=:\ \boldsymbol{w}_k}, \\ \boldsymbol{y}_k &= \boldsymbol{C}\boldsymbol{x}_k, \end{aligned} \tag{2.154}$$

where the input matrix $\boldsymbol{H}$ is divided into two parts $\boldsymbol{H}^c$ and $\boldsymbol{h}^{\bar{c}}$ according to the decomposition of $\boldsymbol{u}_k$. Please note that the defined vector $\boldsymbol{w}_k$ represents a known disturbance.

To cope with this known disturbance by means of a disturbance rejection approach, $\boldsymbol{u}_k^c$ is further split into two parts, i.e.

$$\boldsymbol{u}_k^c = \boldsymbol{u}_{1,k}^c + \boldsymbol{u}_{2,k}^c. \tag{2.155}$$

Accordingly, (2.154) is rewritten as

$$\begin{aligned} \boldsymbol{x}_{k+1} &= \boldsymbol{\Phi}\boldsymbol{x}_k + \boldsymbol{H}^c\boldsymbol{u}_{1,k}^c + \boldsymbol{H}^c\boldsymbol{u}_{2,k}^c + \boldsymbol{w}_k, \\ \boldsymbol{y}_k &= \boldsymbol{C}\boldsymbol{x}_k. \end{aligned} \tag{2.156}$$

The second part of the changeable input is used to vanish the expression

$$\boldsymbol{H}^c\boldsymbol{u}_{2,k}^c + \boldsymbol{w}_k. \tag{2.157}$$

Since $\boldsymbol{H}^c$ is not invertible, the expression (2.157) is minimized in the sense of a least squares approach. The extreme value of $(\boldsymbol{H}^c\boldsymbol{u}_{2,k}^c + \boldsymbol{w}_k)^T(\boldsymbol{H}^c\boldsymbol{u}_{2,k}^c + \boldsymbol{w}_k)$ with respect to $\boldsymbol{u}_{2,k}^c$ calculates as[14]

$$\begin{aligned}
&\frac{\partial}{\partial \boldsymbol{u}_{2,k}^c}\left[(\boldsymbol{H}^c\boldsymbol{u}_{2,k}^c + \boldsymbol{w}_k)^T(\boldsymbol{H}^c\boldsymbol{u}_{2,k}^c + \boldsymbol{w}_k)\right] \stackrel{!}{=} \boldsymbol{0} \\
&\frac{\partial}{\partial \boldsymbol{u}_{2,k}^c}\left[\boldsymbol{w}_k^T\boldsymbol{w}_k + (\boldsymbol{u}_{2,k}^c)^T(\boldsymbol{H}^c)^T\boldsymbol{w}_k + \boldsymbol{w}_k^T\boldsymbol{H}^c\boldsymbol{u}_{2,k}^c + (\boldsymbol{u}_{2,k}^c)^T(\boldsymbol{H}^c)^T\boldsymbol{H}^c\boldsymbol{u}_{2,k}^c\right] = \boldsymbol{0} \\
&\frac{\partial}{\partial \boldsymbol{u}_{2,k}^c}\left[\boldsymbol{w}_k^T\boldsymbol{w}_k + 2\boldsymbol{w}_k^T\boldsymbol{H}^c\boldsymbol{u}_{2,k}^c + (\boldsymbol{u}_{2,k}^c)^T(\boldsymbol{H}^c)^T\boldsymbol{H}^c\boldsymbol{u}_{2,k}^c\right] = \boldsymbol{0} \\
&2\boldsymbol{w}_k^T\boldsymbol{H}^c + (\boldsymbol{u}_{2,k}^c)^T\left[(\boldsymbol{H}^c)^T\boldsymbol{H}^c + (\boldsymbol{H}^c)^T\boldsymbol{H}^c\right] = \boldsymbol{0} \\
&2\boldsymbol{w}_k^T\boldsymbol{H}^c + 2(\boldsymbol{u}_{2,k}^c)^T(\boldsymbol{H}^c)^T\boldsymbol{H}^c = \boldsymbol{0} \\
&(\boldsymbol{H}^c)^T\boldsymbol{w}_k + (\boldsymbol{H}^c)^T\boldsymbol{H}^c\boldsymbol{u}_{2,k}^c = \boldsymbol{0}.
\end{aligned} \tag{2.158}$$

Solving for $\boldsymbol{u}_{2,k}^c$ then results

$$\boldsymbol{u}_{2,k}^c = -\underbrace{\left[(\boldsymbol{H}^c)^T\boldsymbol{H}^c\right]^{-1}(\boldsymbol{H}^c)^T}_{\text{pseudoinverse of } \boldsymbol{H}^c}\boldsymbol{w}_k. \tag{2.159}$$

To ensure that (2.159) represents a minimum, it is sufficient to show that

$$\frac{\partial^2}{\partial(\boldsymbol{u}_{2,k}^c)^2}\left[(\boldsymbol{H}^c\boldsymbol{u}_{2,k}^c + \boldsymbol{w}_k)^T(\boldsymbol{H}^c\boldsymbol{u}_{2,k}^c + \boldsymbol{w}_k)\right] = 2(\boldsymbol{H}^c)^T\boldsymbol{H}^c \tag{2.160}$$

is positive definite. Since the columns of $\boldsymbol{H}^c$ are linearly independent, this implies that $(\boldsymbol{H}^c)^T\boldsymbol{H}^c$ is positive definite and thus, (2.159) represents a minimum.

[14] Since $\boldsymbol{w}_k^T\boldsymbol{H}^c\boldsymbol{u}_{2,k}^c$ is a scalar value, it holds that $\boldsymbol{w}_k^T\boldsymbol{H}^c\boldsymbol{u}_{2,k}^c = (\boldsymbol{w}_k^T\boldsymbol{H}^c\boldsymbol{u}_{2,k}^c)^T = (\boldsymbol{u}_{2,k}^c)^T(\boldsymbol{H}^c)^T\boldsymbol{w}_k$.

Under the assumption that (2.157) vanishes completely, system (2.156) simplifies to

$$\begin{aligned} \boldsymbol{x}_{k+1} &= \boldsymbol{\Phi}\boldsymbol{x}_k + \boldsymbol{H}^c\boldsymbol{u}^c_{1,k}, \\ \boldsymbol{y}_k &= \boldsymbol{C}\boldsymbol{x}_k. \end{aligned} \tag{2.161}$$

The controllability of (2.161) is checked numerically with the help of the Hautus criterion, i.e. every left eigenvector $\boldsymbol{v}_i$ corresponding to the eigenvalue λ_i of $\boldsymbol{\Phi}$ fulfills

$$\boldsymbol{v}_i^T\boldsymbol{H}^c \neq \boldsymbol{0}^T. \tag{2.162}$$

In the following, two different control strategies, namely a PI state feedback controller and an extended observer-based control approach, are designed for (2.161). The prerequisite for the designed controllers is that the closed-loop response does not show a residual steady-state control error for constant reference signals $\boldsymbol{r}_k$ in the presence of constant perturbations. The maximum electrical power supplied to the LEDs is limited to 4.3 W. Furthermore, the LEDs should not be operated below 0.6 W to assure a long lifetime of the used hardware. To be aware of the present input saturation, the controller should include a suitable anti-windup strategy.

2.6.1 PI state feedback controller

State feedback controllers can not inherently guarantee a vanishing steady state control error in the event of constant disturbances or modeling uncertainties. This requires to extend the system (2.161) with integral action. Therefore, the latter is augmented with the integrator states $\boldsymbol{x}_{I,k}$, summing up the control error $\boldsymbol{r}_k - \boldsymbol{y}_k$. The modified system accordingly reads as

$$\begin{aligned} \boldsymbol{x}_{k+1} &= \boldsymbol{\Phi}\boldsymbol{x}_k + \boldsymbol{H}^c\boldsymbol{u}^c_{1,k}, \\ \boldsymbol{x}_{I,k+1} &= \boldsymbol{x}_{I,k} + \boldsymbol{r}_k - \boldsymbol{y}_k, \\ \boldsymbol{y}_k &= \boldsymbol{C}\boldsymbol{x}_k. \end{aligned} \tag{2.163}$$

The second difference equation ensures that the system output tracks a constant reference signal $(\boldsymbol{r}_k) = (\boldsymbol{r}_\infty,\ \boldsymbol{r}_\infty,\ \ldots)$ in steady-state, i.e. $\boldsymbol{r}_\infty = \boldsymbol{y}_\infty$, as long as the overall system is asymptotically stable. The applied control law is given as

$$\boldsymbol{u}^c_{1,k} = \boldsymbol{K}\boldsymbol{x}_k + \boldsymbol{K}_I\boldsymbol{x}_{I,k} + \boldsymbol{K}_P(\boldsymbol{r}_k - \underbrace{\boldsymbol{C}\boldsymbol{x}_k}_{\boldsymbol{y}_k}), \tag{2.164}$$

where the feedback gains $\boldsymbol{K}$, $\boldsymbol{K}_I$ and $\boldsymbol{K}_P$ are of appropriate dimension. Figure 2.28 schematically depicts the overall control loop.

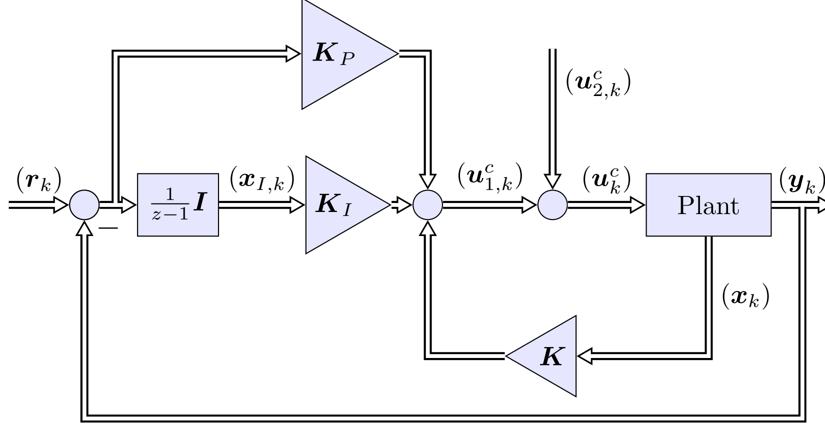

Figure 2.28: PI state feedback controller

In order to find suitable feedback gains, the first step is to calculate the closed-loop system by inserting the control law into (2.163), i.e.

$$\begin{aligned}\boldsymbol{x}_{k+1} &= \boldsymbol{\Phi}\boldsymbol{x}_k + \boldsymbol{H}^c\boldsymbol{K}\boldsymbol{x}_k + \boldsymbol{H}^c\boldsymbol{K}_I\boldsymbol{x}_{I,k} + \boldsymbol{H}^c\boldsymbol{K}_P(\boldsymbol{r}_k - \boldsymbol{C}\boldsymbol{x}_k)\\ &= (\boldsymbol{\Phi} + \boldsymbol{H}^c\boldsymbol{K} - \boldsymbol{H}^c\boldsymbol{K}_P\boldsymbol{C})\boldsymbol{x}_k + \boldsymbol{H}^c\boldsymbol{K}_I\boldsymbol{x}_{I,k} + \boldsymbol{H}^c\boldsymbol{K}_P\boldsymbol{r}_k,\\ \boldsymbol{x}_{I,k+1} &= \boldsymbol{x}_{I,k} + \boldsymbol{r}_k - \boldsymbol{C}\boldsymbol{x}_k.\end{aligned} \tag{2.165}$$

Rewriting (2.165) in matrix notation yields

$$\begin{bmatrix}\boldsymbol{x}_{k+1}\\ \boldsymbol{x}_{I,k+1}\end{bmatrix} = \underbrace{\begin{bmatrix}\boldsymbol{\Phi} + \boldsymbol{H}^c(\boldsymbol{K} - \boldsymbol{K}_P\boldsymbol{C}) & \boldsymbol{H}^c\boldsymbol{K}_I\\ -\boldsymbol{C} & \boldsymbol{I}\end{bmatrix}}_{\circledast}\begin{bmatrix}\boldsymbol{x}_k\\ \boldsymbol{x}_{I,k}\end{bmatrix} + \begin{bmatrix}\boldsymbol{H}^c\boldsymbol{K}_P\\ \boldsymbol{I}\end{bmatrix}\boldsymbol{r}_k. \tag{2.166}$$

Provided that the controller parameters are chosen such that $\circledast$ is a stable matrix, i.e. all its eigenvalues are within the unit circle, a vanishing control error can be ensured. Splitting this matrix into a part which is independent of the controller gains and a gain-dependent part leads to

$$\begin{aligned}\begin{bmatrix}\boldsymbol{\Phi} + \boldsymbol{H}^c(\boldsymbol{K} - \boldsymbol{K}_P\boldsymbol{C}) & \boldsymbol{H}^c\boldsymbol{K}_I\\ -\boldsymbol{C} & \boldsymbol{I}\end{bmatrix} &= \begin{bmatrix}\boldsymbol{\Phi} & \boldsymbol{0}\\ -\boldsymbol{C} & \boldsymbol{I}\end{bmatrix} + \begin{bmatrix}\boldsymbol{H}^c(\boldsymbol{K} - \boldsymbol{K}_P\boldsymbol{C}) & \boldsymbol{H}^c\boldsymbol{K}_I\\ \boldsymbol{0} & \boldsymbol{0}\end{bmatrix}\\ &= \underbrace{\begin{bmatrix}\boldsymbol{\Phi} & \boldsymbol{0}\\ -\boldsymbol{C} & \boldsymbol{I}\end{bmatrix}}_{=:\,\tilde{\boldsymbol{\Phi}}} + \underbrace{\begin{bmatrix}\boldsymbol{H}^c\\ \boldsymbol{0}\end{bmatrix}}_{=:\,\tilde{\boldsymbol{H}}^c}\underbrace{\begin{bmatrix}\boldsymbol{K} - \boldsymbol{K}_P\boldsymbol{C} & \boldsymbol{K}_I\end{bmatrix}}_{=:\,\tilde{\boldsymbol{K}}}.\end{aligned} \tag{2.167}$$

This alternative representation results in a standard eigenvalue placement problem with the closed-loop dynamic matrix $(\tilde{\boldsymbol{\Phi}} + \tilde{\boldsymbol{H}}^c\tilde{\boldsymbol{K}})$, where

$$\tilde{\boldsymbol{K}} = \begin{bmatrix}\tilde{\boldsymbol{K}}_1 & \tilde{\boldsymbol{K}}_2\end{bmatrix}. \tag{2.168}$$

The augmented feedback matrix $\tilde{\boldsymbol{K}}$ is assigned using the LQR approach. Thus, the latter computes as

$$\tilde{\boldsymbol{K}}^T = \left[\boldsymbol{R} + (\tilde{\boldsymbol{H}}^c)^T \boldsymbol{X} \tilde{\boldsymbol{H}}^c\right]^{-1} (\tilde{\boldsymbol{H}}^c)^T \boldsymbol{X} \tilde{\boldsymbol{\Phi}}, \tag{2.169}$$

where $\boldsymbol{X}$ is the solution of the algebraic Riccati equation

$$\boldsymbol{X} = \boldsymbol{Q} + \tilde{\boldsymbol{\Phi}}^T \boldsymbol{X} \tilde{\boldsymbol{\Phi}} - \tilde{\boldsymbol{\Phi}}^T \boldsymbol{X} \tilde{\boldsymbol{H}}^c \left[\boldsymbol{R} + (\tilde{\boldsymbol{H}}^c)^T \boldsymbol{X} \tilde{\boldsymbol{H}}^c\right]^{-1} (\tilde{\boldsymbol{H}}^c)^T \boldsymbol{X} \tilde{\boldsymbol{\Phi}} \tag{2.170}$$

with the positive semi-definite weighting matrix $\boldsymbol{Q}$ and the positive definite matrix $\boldsymbol{R}$. Due to the fact that the pair $(\boldsymbol{\Phi}, \boldsymbol{H}^c)$ is controllable, $\boldsymbol{\Phi}$ has no eigenvalue at 1 and no component of the transfer function from $\boldsymbol{u}^c_{1,k}$ to $\boldsymbol{y}_k$ has a zero at 1, it follows that the pair $(\tilde{\boldsymbol{\Phi}}, \tilde{\boldsymbol{H}}^c)$ is controllable too (see Appendix G). Provided that $\boldsymbol{Q}$ is chosen such that the pair $(\boldsymbol{Q}, \tilde{\boldsymbol{\Phi}})$ is detectable, the Riccati equation has a unique solution.

The parameter $\boldsymbol{K}_I$ directly results from the eigenvalue placement procedure, i.e. $\boldsymbol{K}_I = \tilde{\boldsymbol{K}}_2$. On the other hand, the choice of $\boldsymbol{K}$ and $\boldsymbol{K}_P$ offers some degree of freedom. A common method of choice is to calculate $\boldsymbol{K}_P$ such that the initial value of $\boldsymbol{u}^c_{1,k}$ is equal to its expected steady-state value, which assures

$$\boldsymbol{y}_\infty \stackrel{!}{=} \boldsymbol{r}_\infty \tag{2.171}$$

in case of an ideal plant model. Considering the steady-state of (2.161) and solving for the state vector yields

$$\begin{aligned} \boldsymbol{x}_\infty &= \boldsymbol{\Phi}\boldsymbol{x}_\infty + \boldsymbol{H}^c \boldsymbol{u}^c_{1,\infty} \\ (\boldsymbol{I} - \boldsymbol{\Phi})\boldsymbol{x}_\infty &= \boldsymbol{H}^c \boldsymbol{u}^c_{1,\infty} \\ \boldsymbol{x}_\infty &= (\boldsymbol{I} - \boldsymbol{\Phi})^{-1} \boldsymbol{H}^c \boldsymbol{u}^c_{1,\infty}. \end{aligned} \tag{2.172}$$

Since $\boldsymbol{\Phi}$ has no eigenvalues equal to 1, the matrix $(\boldsymbol{I} - \boldsymbol{\Phi})$ has full rank and is invertible. In addition, the system output for $(k \to \infty)$ reads as

$$\boldsymbol{y}_\infty = \boldsymbol{C}\boldsymbol{x}_\infty. \tag{2.173}$$

Inserting (2.172) into (2.173) results in

$$\boldsymbol{y}_\infty = \boldsymbol{C}(\boldsymbol{I} - \boldsymbol{\Phi})^{-1} \boldsymbol{H}^c \boldsymbol{u}^c_{1,\infty}. \tag{2.174}$$

With (2.171) and rearranging (2.174), the steady-state input signal computes as

$$\boldsymbol{u}^c_{1,\infty} = \left[\boldsymbol{C}(\boldsymbol{I} - \boldsymbol{\Phi})^{-1} \boldsymbol{H}^c\right]^{-1} \boldsymbol{r}_\infty. \tag{2.175}$$

Using (2.175) for the initial value of $\boldsymbol{u}^c_{1,k}$ and assuming that the initial values of $\boldsymbol{x}_k$ and $\boldsymbol{x}_{I,k}$ are zero, it follows

$$\left[\boldsymbol{C}(\boldsymbol{I} - \boldsymbol{\Phi})^{-1} \boldsymbol{H}^c\right]^{-1} \boldsymbol{r}_\infty \stackrel{!}{=} \boldsymbol{K}_P \boldsymbol{r}_\infty \tag{2.176}$$

and thus,

$$\boldsymbol{K}_P = \left[\boldsymbol{C}(\boldsymbol{I} - \boldsymbol{\Phi})^{-1}\boldsymbol{H}^c\right]^{-1}. \tag{2.177}$$

Finally, the remaining feedback gain can be calculated according to (2.167) and (2.168) as

$$\boldsymbol{K} = \tilde{\boldsymbol{K}}_1 + \boldsymbol{K}_P\boldsymbol{C}. \tag{2.178}$$

The designed controller is verified with the help of numerical simulations without considering the input saturation and assuming that all states are available for feedback. The weighting matrices are chosen as

$$\boldsymbol{R} = 5000\boldsymbol{I} \quad \text{and} \quad \boldsymbol{Q} = \mathbf{diag}(\underbrace{0.5,\ \ldots\ 0.5}_{\text{weighting } \boldsymbol{x}_k}, \underbrace{10,\ \ldots\ 10}_{\text{weighting } \boldsymbol{x}_{I,k}}). \tag{2.179}$$

A closed-loop step response simulating the heat-up of a “highly doped” wafer from room temperature to 350 $°C$ (623.15 K) is depicted in Figure 2.29b. As the simulation points out, the closed-loop step response shows an undesired undershoot, because the stabilizing part of the control law forces the wafer's temperature towards the absolute zero point, i.e. -273.15 $°C$ (0 K). This effect may be reduced by adjusting the weighting matrices. A systematic approach, on the other hand, is to introduce the euclidean transformation

$$\boldsymbol{x}'_k := \boldsymbol{x}_k - \boldsymbol{x}_{RT}, \tag{2.180}$$

where the elements of the constant vector $\boldsymbol{x}_{RT}$ are equal to room temperature, i.e. 25 $°C$ (298.15 K). Rearranging (2.180) yields

$$\boldsymbol{x}_k = \boldsymbol{x}'_k + \boldsymbol{x}_{RT} \tag{2.181}$$

and

$$\boldsymbol{x}_{k+1} = \boldsymbol{x}'_{k+1} + \boldsymbol{x}_{RT} \tag{2.182}$$

respectively. Inserting (2.181) and (2.182) into (2.154), i.e. the plant model after splitting the input vector, results

$$\begin{aligned}
\boldsymbol{x}'_{k+1} &= \boldsymbol{\Phi}(\boldsymbol{x}'_k + \boldsymbol{x}_{RT}) + \boldsymbol{H}^c\boldsymbol{u}^c_k + \boldsymbol{w}_k - \boldsymbol{x}_{RT} \\
&= \boldsymbol{\Phi}\boldsymbol{x}'_k + \boldsymbol{H}^c\boldsymbol{u}^c_k + \underbrace{\boldsymbol{w}_k + (\boldsymbol{\Phi} - \boldsymbol{I})\boldsymbol{x}_{RT}}_{\boldsymbol{w}'_k}, \\
\boldsymbol{y}_k &= \boldsymbol{C}(\boldsymbol{x}'_k + \boldsymbol{x}_{RT}).
\end{aligned} \tag{2.183}$$

Please note that the transformed system (2.183) has the very same structure as the original model (2.154). The only difference is that the equilibrium point after rejecting

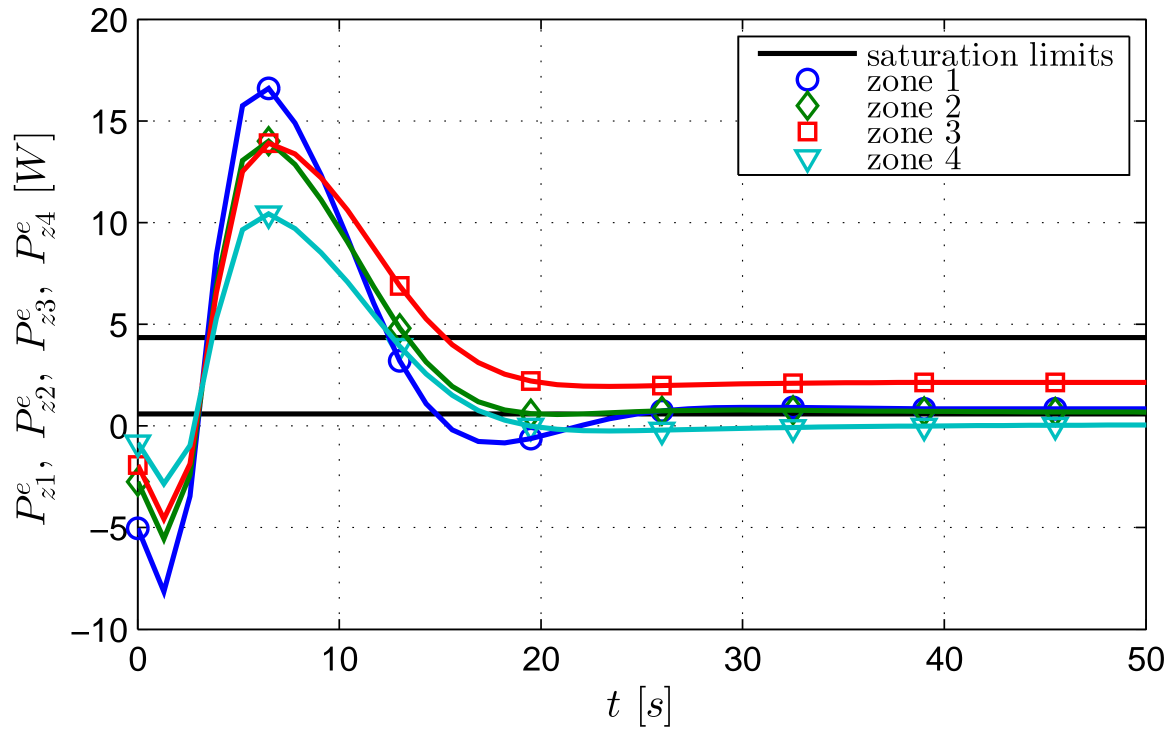

(a) Electrical power supplied to LEDs

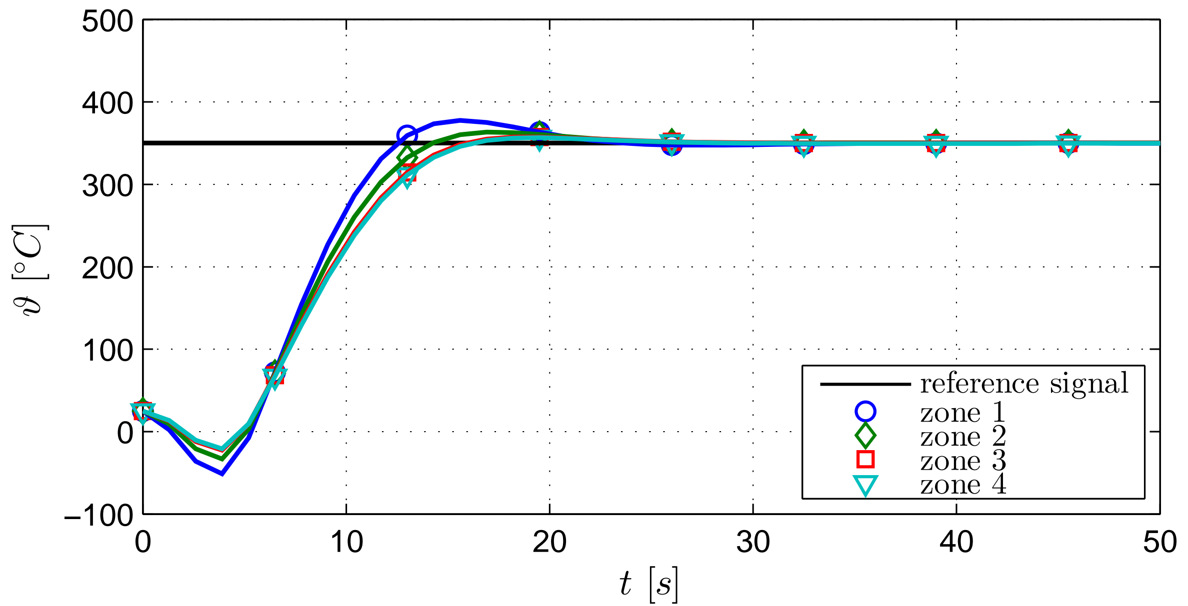

(b) Zone temperatures

Figure 2.29: Simulated heat-up of a "highly doped" wafer: A PI state feedback controller is tested with the help of a numerical simulation. Input saturations and an anti-windup strategy are not considered yet.

the known disturbance is now at room temperature. Thus, the outlined design procedure involving the rejection of the known disturbance $\boldsymbol{w}'_k$ as well as the design of the PI state feedback controller can be adopted to the transformed system as it stands. The closed-loop behaviour is again validated without considering the input saturation and assuming that the system states are available for feedback. The weighting matrices to solve the Riccati equation are chosen as (2.179).

Figure 2.30b shows the heat-up of a "highly doped" wafer from room temperature to 350 $°C$ (623.15 K). As expected, the undershoot can be avoided with the aid of the introduced coordinate transformation. Figure 2.30a, on the other hand, points out that the electrical power supplied to the four heating zones still exceed the saturation limits significantly. As a remedy, an input saturation in combination with a possible anti-windup technique is discussed in Section 2.6.1.1.

2.6.1.1 Prevention of controller windup

The PI state feedback controller with input saturation is schematically depicted in Figure 2.31. The saturation block imposes upper and lower limits on the actuating signal $\boldsymbol{u}_k^c$. The saturated power signal is denoted by $\boldsymbol{u}_{sat,k}^c$. According to the considerations in the previous section, the PI state feedback controller in combination with the disturbance rejection for the plant model after the coordinate transformation reads as[15]

$$\begin{aligned} \boldsymbol{x}_{I,k+1} &= \boldsymbol{x}_{I,k} + \boldsymbol{r}_k - \boldsymbol{y}_k, \\ \boldsymbol{u}_k^c &= \boldsymbol{K}\boldsymbol{x}'_k + \boldsymbol{K}_I\boldsymbol{x}_{I,k} + \boldsymbol{K}_P\boldsymbol{r}_k - \boldsymbol{K}_P\boldsymbol{y}_k - (\boldsymbol{H}^c)^+\boldsymbol{w}_k. \end{aligned} \tag{2.184}$$

A suitable anti-windup strategy for the given controller is the well-known "conditioning technique" according to Hanus [Hanus, Kinnaert, and Henrotte, 1987]. The starting point in this case is a copy of (2.184), i.e.

$$\begin{aligned} \tilde{\boldsymbol{x}}_{I,k+1} &= \tilde{\boldsymbol{x}}_{I,k} + \boldsymbol{r}_k - \boldsymbol{y}_k, \\ \boldsymbol{u}_k^c &= \boldsymbol{K}\boldsymbol{x}'_k + \boldsymbol{K}_I\tilde{\boldsymbol{x}}_{I,k} + \boldsymbol{K}_P\boldsymbol{r}_k - \boldsymbol{K}_P\boldsymbol{y}_k - (\boldsymbol{H}^c)^+\boldsymbol{w}_k, \end{aligned} \tag{2.185}$$

with the new state vector denoted by $\tilde{\boldsymbol{x}}_{I,k}$. The idea behind Hanus' technique is to use an auxiliary reference signal $\tilde{\boldsymbol{r}}_k$, called realizable reference, instead of $\boldsymbol{r}_k$ in case the desired actuating signal is unequal to the saturated one, i.e. $\boldsymbol{u}_k^c \neq \boldsymbol{u}_{sat,k}^c$. The conditioned controller can then be represented as

$$\begin{aligned} \tilde{\boldsymbol{x}}_{I,k+1} &= \tilde{\boldsymbol{x}}_{I,k} + \tilde{\boldsymbol{r}}_k - \boldsymbol{y}_k, \\ \boldsymbol{u}_{sat,k}^c &= \boldsymbol{K}\boldsymbol{x}'_k + \boldsymbol{K}_I\tilde{\boldsymbol{x}}_{I,k} + \boldsymbol{K}_P\tilde{\boldsymbol{r}}_k - \boldsymbol{K}_P\boldsymbol{y}_k - (\boldsymbol{H}^c)^+\boldsymbol{w}_k. \end{aligned} \tag{2.186}$$

[15] $(\boldsymbol{H}^c)^+ = \left[(\boldsymbol{H}^c)^T\boldsymbol{H}^c\right]^{-1}(\boldsymbol{H}^c)^T$ denotes the pseudoinverse of $\boldsymbol{H}^c$.

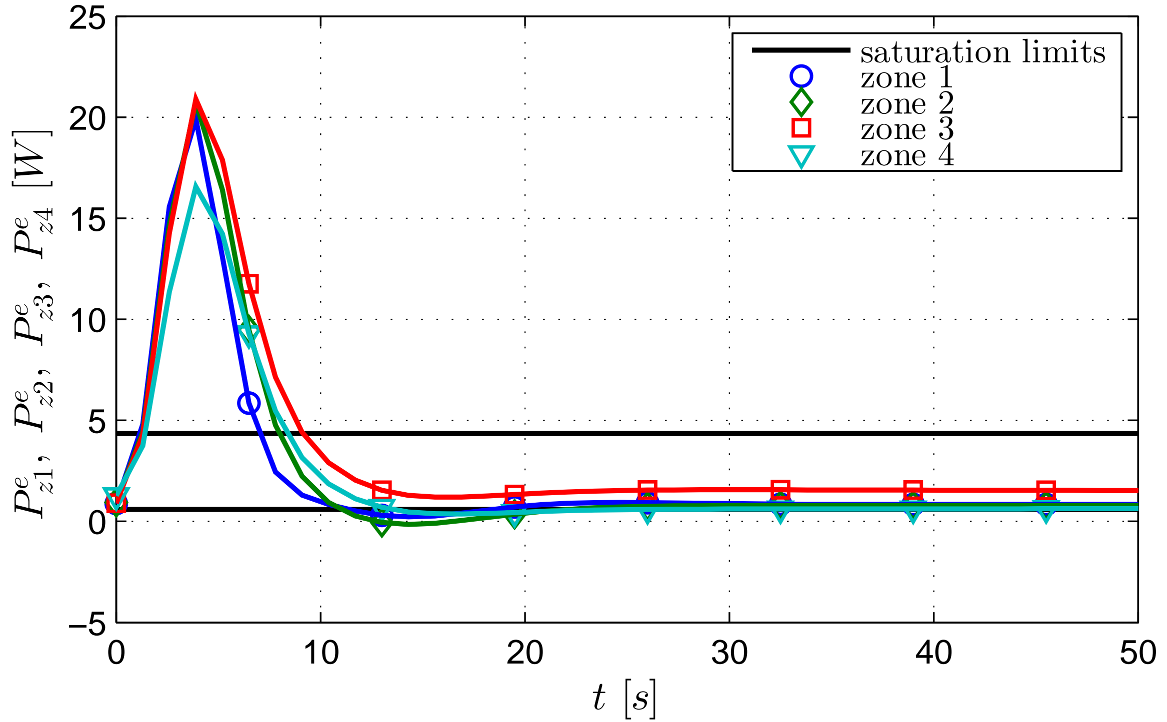

(a) Electrical power supplied to LEDs

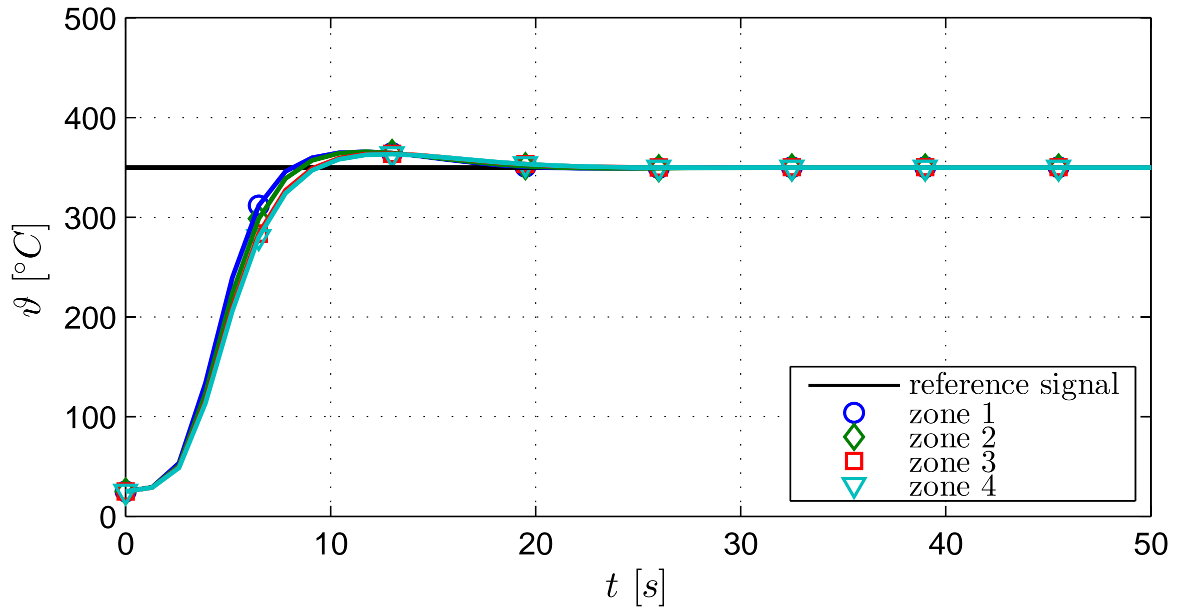

(b) Zone temperatures

Figure 2.30: Simulated heat-up of a “highly doped” wafer: An additional coordinate transformation is applied in order to avoid an undershoot of the control outputs. The input saturations are not considered.

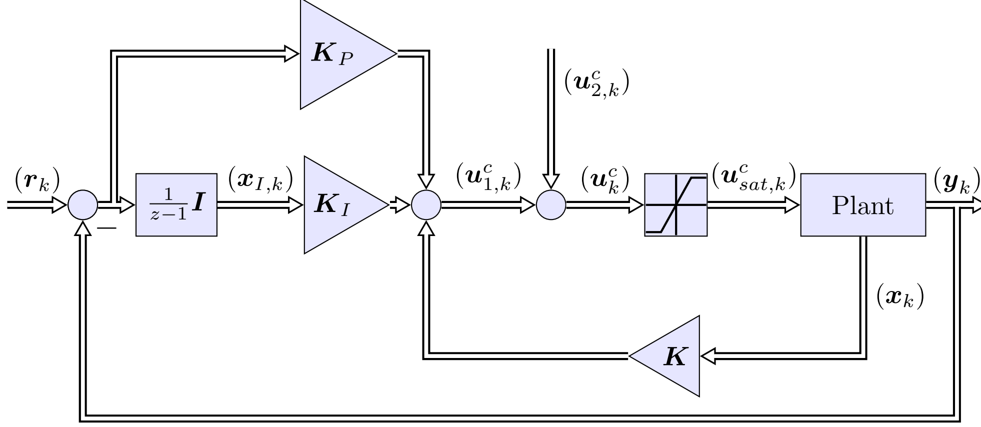

Figure 2.31: PI state feedback controller

The use of the conditioned reference signal forces the actuating signal to be equal to the saturated one. To calculate the auxiliary reference signal, the difference between $\boldsymbol{u}^c_{sat,k}$ and $\boldsymbol{u}^c_k$ is evaluated, i.e.

$$\boldsymbol{u}^c_{sat,k} - \boldsymbol{u}^c_k = \boldsymbol{K}_P\left(\tilde{\boldsymbol{r}}_k - \boldsymbol{r}_k\right). \tag{2.187}$$

Solving (2.187) for $\tilde{\boldsymbol{r}}_k$ yields

$$\tilde{\boldsymbol{r}}_k = \boldsymbol{r}_k + \boldsymbol{K}_P^{-1}\left(\boldsymbol{u}^c_{sat,k} - \boldsymbol{u}^c_k\right). \tag{2.188}$$

Inserting (2.188) into the conditioned controller (2.186) and using equation(2.185) finally results

$$\begin{aligned}
\tilde{\boldsymbol{x}}_{I,k+1} &= \tilde{\boldsymbol{x}}_{I,k} + \tilde{\boldsymbol{r}}_k - \boldsymbol{y}_k \\
&= \tilde{\boldsymbol{x}}_{I,k} + \boldsymbol{r}_k + \boldsymbol{K}_P^{-1}\boldsymbol{u}^c_{sat,k} - \boldsymbol{K}_P^{-1}\boldsymbol{u}^c_k - \boldsymbol{y}_k \\
&= \tilde{\boldsymbol{x}}_{I,k} + \boldsymbol{K}_P^{-1}\boldsymbol{u}^c_{sat,k} - \boldsymbol{K}_P^{-1}\boldsymbol{K}\boldsymbol{x}'_k - \boldsymbol{K}_P^{-1}\boldsymbol{K}_I\tilde{\boldsymbol{x}}_{I,k} + \boldsymbol{K}_P^{-1}(\boldsymbol{H}^c)^+\boldsymbol{w}_k \\
&= \left(\boldsymbol{I} - \boldsymbol{K}_P^{-1}\boldsymbol{K}_I\right)\tilde{\boldsymbol{x}}_{I,k} + \boldsymbol{K}_P^{-1}\boldsymbol{u}^c_{sat,k} - \boldsymbol{K}_P^{-1}\boldsymbol{K}\boldsymbol{x}'_k + \boldsymbol{K}_P^{-1}(\boldsymbol{H}^c)^+\boldsymbol{w}_k, \\
\boldsymbol{u}^c_k &= \boldsymbol{K}\boldsymbol{x}'_k + \boldsymbol{K}_I\tilde{\boldsymbol{x}}_{I,k} + \boldsymbol{K}_P\boldsymbol{r}_k - \boldsymbol{K}_P\boldsymbol{y}_k - (\boldsymbol{H}^c)^+\boldsymbol{w}_k.
\end{aligned} \tag{2.189}$$

Obviously, the matrix $\boldsymbol{K}_P$ must have full rank, i.e. its inverse exists. Referring to [Hanus, Kinnaert, and Henrotte, 1987], this condition is fulfilled, since the opposite would lead to at least one dead time in the control action, which is not the case here. Of course, the overall control loop is designed in such a manner that it is stable in case the saturation is inactive. On the other hand, it is necessary that the conditioned controller (2.189) is stable as well, i.e. the eigenvalues of the matrix $(\boldsymbol{I} - \boldsymbol{K}_P^{-1}\boldsymbol{K}_I)$ are within the unit circle. Unfortunately, the calculation of the controller parameters with the weighting matrices (2.179) show that this condition is not fulfilled. This problem is adressed in [Walgama, Ronnback, and Sternby, 1992] and the authors propose a modification to the conditioning

technique. Instead of calculating the auxiliary reference signal $\tilde{\boldsymbol{r}}_k$ as (2.188), the latter is chosen as

$$\tilde{\boldsymbol{r}}_k = \boldsymbol{r}_k + (\boldsymbol{K}_P + \gamma \boldsymbol{I})^{-1} \left(\boldsymbol{u}^c_{sat,k} - \boldsymbol{u}^c_k\right) \tag{2.190}$$

with the additional design parameter γ. Using (2.190) for the conditioned controller (2.186) yields

$$\begin{aligned}
\tilde{\boldsymbol{x}}_{I,k+1} &= \tilde{\boldsymbol{x}}_{I,k} + \tilde{\boldsymbol{r}}_k - \boldsymbol{y}_k \\
&= \tilde{\boldsymbol{x}}_{I,k} + \boldsymbol{r}_k + (\boldsymbol{K}_P + \gamma \boldsymbol{I})^{-1} \boldsymbol{u}^c_{sat,k} - (\boldsymbol{K}_P + \gamma \boldsymbol{I})^{-1} \boldsymbol{u}^c_k - \boldsymbol{y}_k \\
&= \tilde{\boldsymbol{x}}_{I,k} + \boldsymbol{r}_k + (\boldsymbol{K}_P + \gamma \boldsymbol{I})^{-1} \boldsymbol{u}^c_{sat,k} - (\boldsymbol{K}_P + \gamma \boldsymbol{I})^{-1} \boldsymbol{K}\boldsymbol{x}'_k - (\boldsymbol{K}_P + \gamma \boldsymbol{I})^{-1} \boldsymbol{K}_I \tilde{\boldsymbol{x}}_{I,k} \\
&\quad - (\boldsymbol{K}_P + \gamma \boldsymbol{I})^{-1} \boldsymbol{K}_P \boldsymbol{r}_k + (\boldsymbol{K}_P + \gamma \boldsymbol{I})^{-1} \boldsymbol{K}_P \boldsymbol{y}_k + (\boldsymbol{K}_P + \gamma \boldsymbol{I})^{-1} (\boldsymbol{H}^c)^+ \boldsymbol{w}_k - \boldsymbol{y}_k \\
&= \left[\boldsymbol{I} - (\boldsymbol{K}_P + \gamma \boldsymbol{I})^{-1} \boldsymbol{K}_I\right] \tilde{\boldsymbol{x}}_{I,k} + \left[\boldsymbol{I} - (\boldsymbol{K}_P + \gamma \boldsymbol{I})^{-1} \boldsymbol{K}_P\right] \boldsymbol{r}_k \\
&\quad + (\boldsymbol{K}_P + \gamma \boldsymbol{I})^{-1} \boldsymbol{u}^c_{sat,k} - (\boldsymbol{K}_P + \gamma \boldsymbol{I})^{-1} \boldsymbol{K}\boldsymbol{x}'_k + \left[(\boldsymbol{K}_P + \gamma \boldsymbol{I})^{-1} \boldsymbol{K}_P - \boldsymbol{I}\right] \boldsymbol{y}_k \\
&\quad + (\boldsymbol{K}_P + \gamma \boldsymbol{I})^{-1} (\boldsymbol{H}^c)^+ \boldsymbol{w}_k, \\
\boldsymbol{u}^c_k &= \boldsymbol{K}\boldsymbol{x}'_k + \boldsymbol{K}_I \tilde{\boldsymbol{x}}_{I,k} + \boldsymbol{K}_P \boldsymbol{r}_k - \boldsymbol{K}_P \boldsymbol{y}_k - (\boldsymbol{H}^c)^+ \boldsymbol{w}_k.
\end{aligned} \tag{2.191}$$

The designed controller (2.191) is verified with the help of a numerical simulation. The design parameter γ is chosen as 0.2, which guarantees that the eigenvalues of $\left[\boldsymbol{I} - (\boldsymbol{K}_P + \gamma \boldsymbol{I})^{-1} \boldsymbol{K}_I\right]$ are within the unit circle. Figure 2.32 depicts a heat-up scenario of a "highly doped" wafer. The designed controller is now stable. However, the performance achieved does not meet expectations and further approaches need to be evaluated.

2.6.2 Extended observer-based control approach

The designed PI state feedback controller in combination with anti-windup strategy according to Hanus and Walgama ensures a stable feedback loop even under the presence of an input saturation. The performance in terms of its transient behaviour, on the other hand, is unsatisfactory and the parameter γ has to be found experimentally.

An additional control approach is thus designed and evaluated for the system (2.161). To account for modelling uncertainties, the plant model is extended with an additional unknown disturbance $\boldsymbol{d}_k$, which is assumed to be constant for $k \to \infty$. Furthermore, it is assumed that the latter is acting at the system input, i.e. the model is rewritten as

$$\begin{aligned}
\boldsymbol{x}_{k+1} &= \boldsymbol{\Phi}\boldsymbol{x}_k + \boldsymbol{H}^c \boldsymbol{u}^c_{1,k} + \boldsymbol{H}^c \boldsymbol{d}_k, \\
\boldsymbol{y}_k &= \boldsymbol{C}\boldsymbol{x}_k.
\end{aligned} \tag{2.192}$$

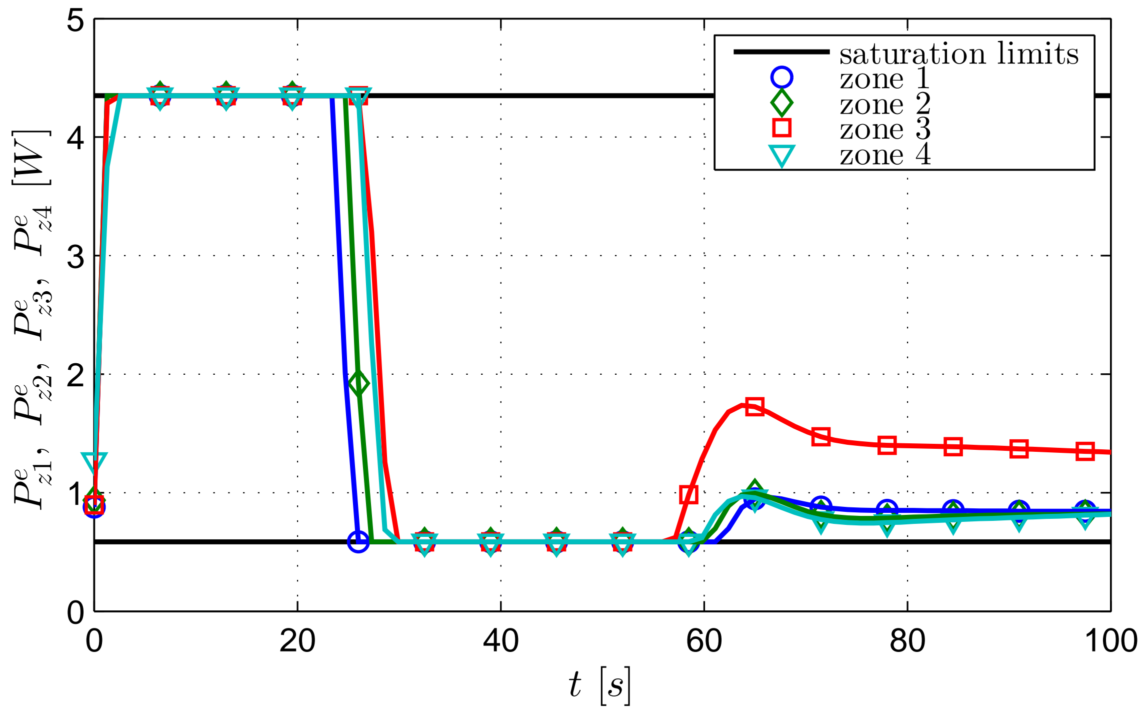

(a) Electrical power supplied to LEDs

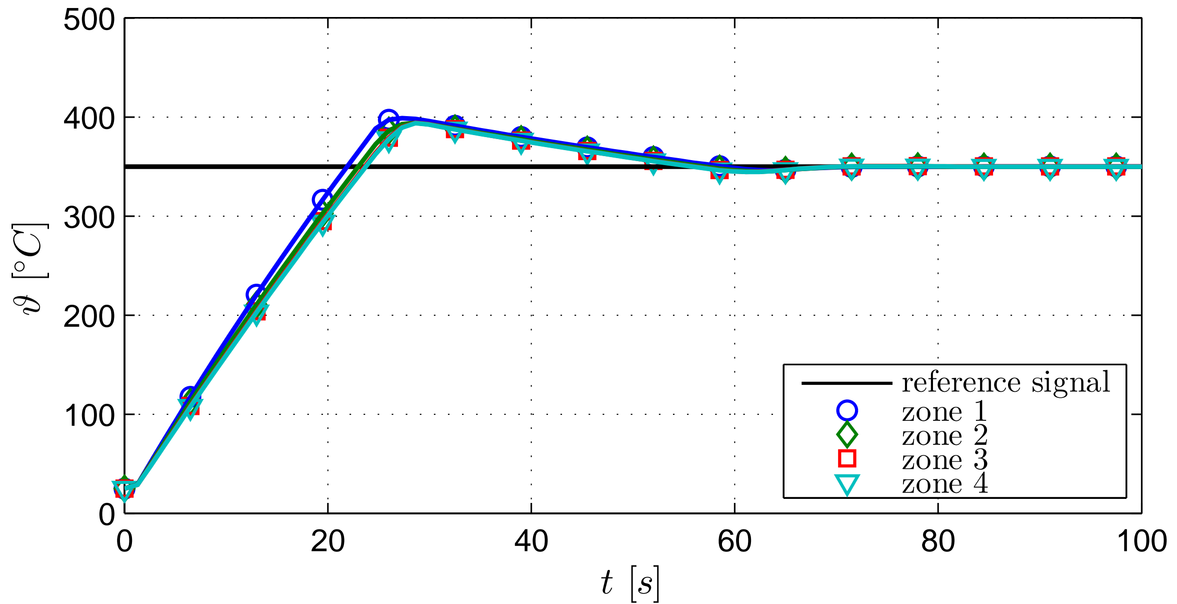

(b) Zone temperatures

Figure 2.32: Simulated heat-up of a "highly doped" wafer: The PI state feedback controller is extended with a strategy according to Hanus and Walgama [Hanus, Kinnaert, and Henrotte, 1987; Walgama, Ronnback, and Sternby, 1992] in order to prevent the effect of controller windup. Although a windup can be avoided, the controller performance is unsatisfactory due to a high and long-lasting overshoot.

In the following, a controller is designed which ensures that the control error vanishes in steady-state. In a first step, a state feedback controller with a static pre-filter

$$\boldsymbol{u}_{1,k}^{c} = \boldsymbol{K}\boldsymbol{x}_k + \boldsymbol{N}\boldsymbol{r}_k \tag{2.193}$$

is considered. The pre-filter is assigned such that the output $\boldsymbol{y}_k$ tracks a constant reference signal $(\boldsymbol{r}_k) = (\boldsymbol{r}_\infty,\ \boldsymbol{r}_\infty,\ \ldots)$ asymptotically in case of a perfect plant model and no disturbances acting, i.e. $(\boldsymbol{d}_k) = (\boldsymbol{0},\ \boldsymbol{0},\ \ldots)$. Thus, the pre-filter $\boldsymbol{N}$ can be calculated by considering the plant (2.192) with control law (2.193) in steady-state, i.e.

$$\begin{aligned}\boldsymbol{x}_\infty &= (\boldsymbol{\Phi} + \boldsymbol{H}^c\boldsymbol{K})\boldsymbol{x}_\infty + \boldsymbol{H}^c\boldsymbol{N}\boldsymbol{r}_\infty \\ &= \left[\boldsymbol{I} - (\boldsymbol{\Phi} + \boldsymbol{H}^c\boldsymbol{K})\right]^{-1}\boldsymbol{H}^c\boldsymbol{N}\boldsymbol{r}_\infty, \\ \boldsymbol{y}_\infty &= \boldsymbol{C}\boldsymbol{x}_\infty.\end{aligned} \tag{2.194}$$

With

$$\boldsymbol{y}_\infty \overset{!}{=} \boldsymbol{r}_\infty \tag{2.195}$$

it follows

$$\boldsymbol{C}\left[\boldsymbol{I} - (\boldsymbol{\Phi} + \boldsymbol{H}^c\boldsymbol{K})\right]^{-1}\boldsymbol{H}^c\boldsymbol{N}\boldsymbol{r}_\infty \overset{!}{=} \boldsymbol{r}_\infty \tag{2.196}$$

and thus, the pre-filter computes as

$$\boldsymbol{N} = \left\{\boldsymbol{C}\left[\boldsymbol{I} - (\boldsymbol{\Phi} + \boldsymbol{H}^c\boldsymbol{K})\right]^{-1}\boldsymbol{H}^c\right\}^{-1}. \tag{2.197}$$

The constant gain $\boldsymbol{K}$ is calculated by means of the LQR approach. Since $\boldsymbol{x}_k$ is not available, a Luenberger observer

$$\hat{\boldsymbol{x}}_{k+1} = \boldsymbol{\Phi}\hat{\boldsymbol{x}}_k + \boldsymbol{H}^c\boldsymbol{u}_{1,k}^c + \hat{\boldsymbol{L}}(\boldsymbol{y}_k - \boldsymbol{C}\hat{\boldsymbol{x}}_k) \tag{2.198}$$

for the time-invariant system (2.192) is designed similar to Section 2.4.5 without considering the unknown disturbance. The observer gain $\hat{\boldsymbol{L}}$ is computed as

$$\hat{\boldsymbol{L}}^T = (\boldsymbol{V}_c + \boldsymbol{C}\boldsymbol{Y}\boldsymbol{C}^T)^{-1}\boldsymbol{C}\boldsymbol{Y}\boldsymbol{\Phi}^T, \tag{2.199}$$

where $\boldsymbol{Y}$ is the solution of the algebraic Riccati equation

$$\boldsymbol{Y} = \boldsymbol{W}_c + \boldsymbol{\Phi}\boldsymbol{Y}\boldsymbol{\Phi}^T - \boldsymbol{\Phi}\boldsymbol{Y}\boldsymbol{C}^T(\boldsymbol{V}_c + \boldsymbol{C}\boldsymbol{Y}\boldsymbol{C}^T)^{-1}\boldsymbol{C}\boldsymbol{Y}\boldsymbol{\Phi}^T. \tag{2.200}$$

Since the system is time-invariant, the Riccati equation can be solved offline.

Calculating the dynamics of the estimation error $\boldsymbol{e}_k := \boldsymbol{x}_k - \hat{\boldsymbol{x}}_k$ yields

$$\boldsymbol{e}_{k+1} = (\boldsymbol{\Phi} - \hat{\boldsymbol{L}}\boldsymbol{C})\boldsymbol{e}_k + \boldsymbol{H}^c\boldsymbol{d}_k, \tag{2.201}$$

i.e. the steady-state estimation error is unequal to zero in the event that $\boldsymbol{d}_k$ is unequal to zero. In this case $\Delta\boldsymbol{y}_k := \boldsymbol{y}_k - \boldsymbol{C}\hat{\boldsymbol{x}}_k = \boldsymbol{C}(\boldsymbol{x}_k - \hat{\boldsymbol{x}}_k) = \boldsymbol{C}\boldsymbol{e}_k$ neither converges to zero and it holds

$$\begin{aligned} \boldsymbol{e}_\infty &= (\boldsymbol{\Phi} - \hat{\boldsymbol{L}}\boldsymbol{C})\boldsymbol{e}_\infty + \boldsymbol{H}^c\boldsymbol{d}_\infty \\ \left[\boldsymbol{I} - (\boldsymbol{\Phi} - \hat{\boldsymbol{L}}\boldsymbol{C})\right]\boldsymbol{e}_\infty &= \boldsymbol{H}^c\boldsymbol{d}_\infty \\ \boldsymbol{e}_\infty &= \left[\boldsymbol{I} - (\boldsymbol{\Phi} - \hat{\boldsymbol{L}}\boldsymbol{C})\right]^{-1}\boldsymbol{H}^c\boldsymbol{d}_\infty \end{aligned} \tag{2.202}$$

and accordingly

$$\Delta\boldsymbol{y}_\infty = \boldsymbol{C}\left[\boldsymbol{I} - (\boldsymbol{\Phi} - \hat{\boldsymbol{L}}\boldsymbol{C})\right]^{-1}\boldsymbol{H}^c\boldsymbol{d}_\infty. \tag{2.203}$$

Rearranging (2.203) yields the calculated disturbance in steady-state given by

$$\boldsymbol{d}_\infty = \left\{\boldsymbol{C}\left[\boldsymbol{I} - (\boldsymbol{\Phi} - \hat{\boldsymbol{L}}\boldsymbol{C})\right]^{-1}\boldsymbol{H}^c\right\}^{-1}\Delta\boldsymbol{y}_\infty \tag{2.204}$$

and respectively

$$\boldsymbol{e}_\infty = \left[\boldsymbol{I} - (\boldsymbol{\Phi} - \hat{\boldsymbol{L}}\boldsymbol{C})\right]^{-1}\boldsymbol{H}^c\left\{\boldsymbol{C}\left[\boldsymbol{I} - (\boldsymbol{\Phi} - \hat{\boldsymbol{L}}\boldsymbol{C})\right]^{-1}\boldsymbol{H}^c\right\}^{-1}\Delta\boldsymbol{y}_\infty. \tag{2.205}$$

This means that the steady-state estimation error can be calculated as a function of $\Delta\boldsymbol{y}_\infty$. Thus, the idea is to introduce a corrected estimate for the state vector as

$$\begin{aligned} \bar{\boldsymbol{x}}_k &:= \hat{\boldsymbol{x}}_k + \boldsymbol{e}_\infty \\ &= \hat{\boldsymbol{x}}_k + \left[\boldsymbol{I} - (\boldsymbol{\Phi} - \hat{\boldsymbol{L}}\boldsymbol{C})\right]^{-1}\boldsymbol{H}^c\left\{\boldsymbol{C}\left[\boldsymbol{I} - (\boldsymbol{\Phi} - \hat{\boldsymbol{L}}\boldsymbol{C})\right]^{-1}\boldsymbol{H}^c\right\}^{-1}\Delta\boldsymbol{y}_\infty. \end{aligned} \tag{2.206}$$

This guarantees that it holds

$$\boldsymbol{x}_\infty - \bar{\boldsymbol{x}}_\infty = \boldsymbol{0}. \tag{2.207}$$

In the event that the corrected state vector is used for feedback and, in addition, subtracting (2.204) from the actuating signal yields the extended feedback law

$$\begin{aligned} \boldsymbol{u}^c_{1,k} &= \boldsymbol{K}\bar{\boldsymbol{x}}_k - \boldsymbol{d}_\infty + \boldsymbol{N}\boldsymbol{r}_k \\ &= \boldsymbol{K}\hat{\boldsymbol{x}}_k + \boldsymbol{K}\left[\boldsymbol{I} - (\boldsymbol{\Phi} - \hat{\boldsymbol{L}}\boldsymbol{C})\right]^{-1}\boldsymbol{H}^c\left\{\boldsymbol{C}\left[\boldsymbol{I} - (\boldsymbol{\Phi} - \hat{\boldsymbol{L}}\boldsymbol{C})\right]^{-1}\boldsymbol{H}^c\right\}^{-1}\Delta\boldsymbol{y}_\infty \\ &\quad - \left\{\boldsymbol{C}\left[\boldsymbol{I} - (\boldsymbol{\Phi} - \hat{\boldsymbol{L}}\boldsymbol{C})\right]^{-1}\boldsymbol{H}^c\right\}^{-1}\Delta\boldsymbol{y}_\infty + \boldsymbol{N}\boldsymbol{r}_k \\ &= \boldsymbol{K}\hat{\boldsymbol{x}}_k + \boldsymbol{K}_I\Delta\boldsymbol{y}_\infty + \boldsymbol{N}\boldsymbol{r}_k \end{aligned} \tag{2.208}$$

with

$$\boldsymbol{K}_I := \left\{\boldsymbol{K}\left[\boldsymbol{I} - (\boldsymbol{\Phi} - \hat{\boldsymbol{L}}\boldsymbol{C})\right]^{-1}\boldsymbol{H}^c - \boldsymbol{I}\right\}\left\{\boldsymbol{C}\left[\boldsymbol{I} - (\boldsymbol{\Phi} - \hat{\boldsymbol{L}}\boldsymbol{C})\right]^{-1}\boldsymbol{H}^c\right\}^{-1}.$$

Clearly, $\Delta\boldsymbol{y}_\infty$ is not measurable. Thus, $\Delta\boldsymbol{y}_\infty$ is replaced with $\Delta\boldsymbol{y}_k$, i.e.

$$\boldsymbol{u}^c_{1,k} = \boldsymbol{K}\hat{\boldsymbol{x}}_k + \boldsymbol{K}_I\Delta\boldsymbol{y}_k + \boldsymbol{N}\boldsymbol{r}_k. \tag{2.209}$$

This still guarantees that $\boldsymbol{y}_k$ tracks a constant reference signal $\boldsymbol{r}_k$ in steady-state, even in the presence of unknown perturbations that are constant for $k \to \infty$.

The presented approach is also suitable in the presence of model mismatches. The main advantage of the derived controller is that a controller windup can be prevented systematically by applying the well-known observer technique [Hippe, 2006], i.e. the observer (2.198) is driven by the saturated input.

2.6.2.1 Numerical simulation and laboratory experiments

The designed controller is tested with the help of numerical simulations. To simulate the plant, the derived nonlinear, affine-input model (2.41) is used. The four outputs of the systems are available for feedback in simulation. Table 2.5 lists the parameters for the observer-based controller.

Parameter	Value	Description
$\boldsymbol{Q}$	$\boldsymbol{I}$	Controller weighting matrix
$\boldsymbol{R}$	$10\boldsymbol{I}$	Controller weighting matrix
$\boldsymbol{W}_c$	$10\boldsymbol{I}$	Observer weighting matrix
$\boldsymbol{V}_c$	$\boldsymbol{I}$	Observer weighting matrix

Table 2.5: Parameters for the observer-based controller

As shown in Figures 2.33 and 2.34, the heating of the wafer can be performed regardless of the wafer type. Because of the higher emissivity of a highly doped wafer compared to a bare silicon wafer, the heat losses due to radiation are higher. This goes along with a higher amount of electrical power required to heat a highly doped wafer.

The designed observer in combination with the derived controller was also tested at the test rig. Again, a uniform wafer temperature profile of 350 $°C$ should be controlled to achieve uniform process results across the whole wafer. As Figure 2.35 and 2.36 point out, the designed feedback loop allows the setting up of a desired wafer temperature with a very accurate performance independent of the wafer type.

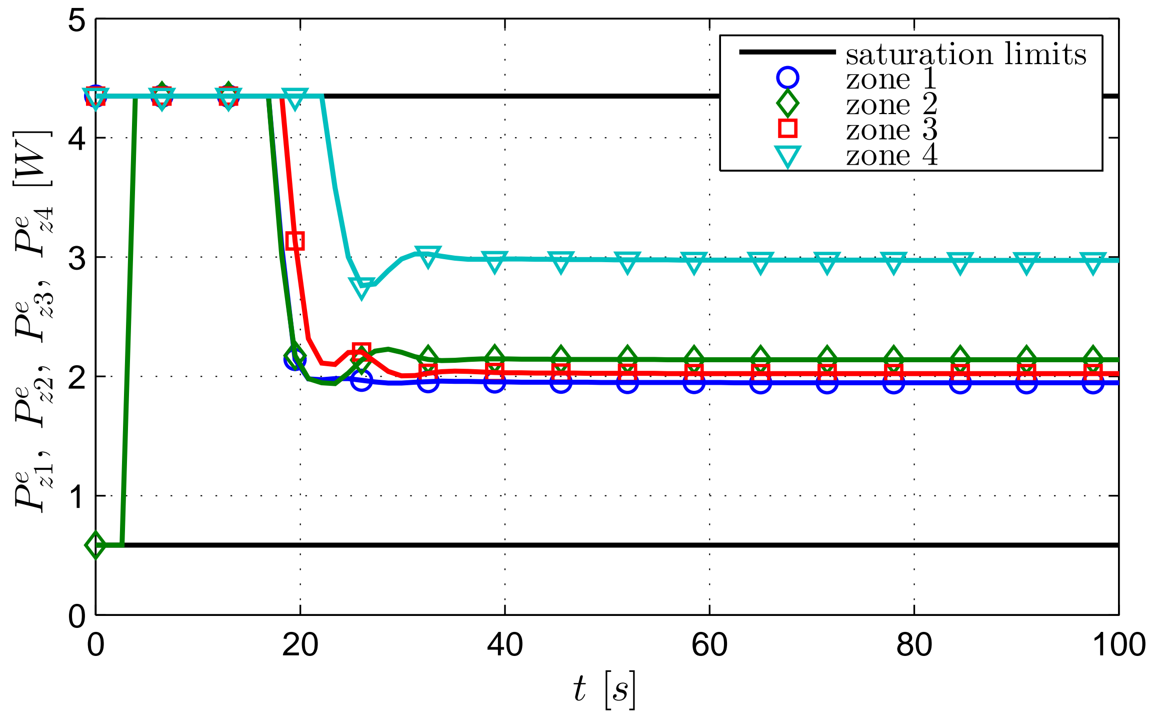

(a) Electrical power supplied to LEDs

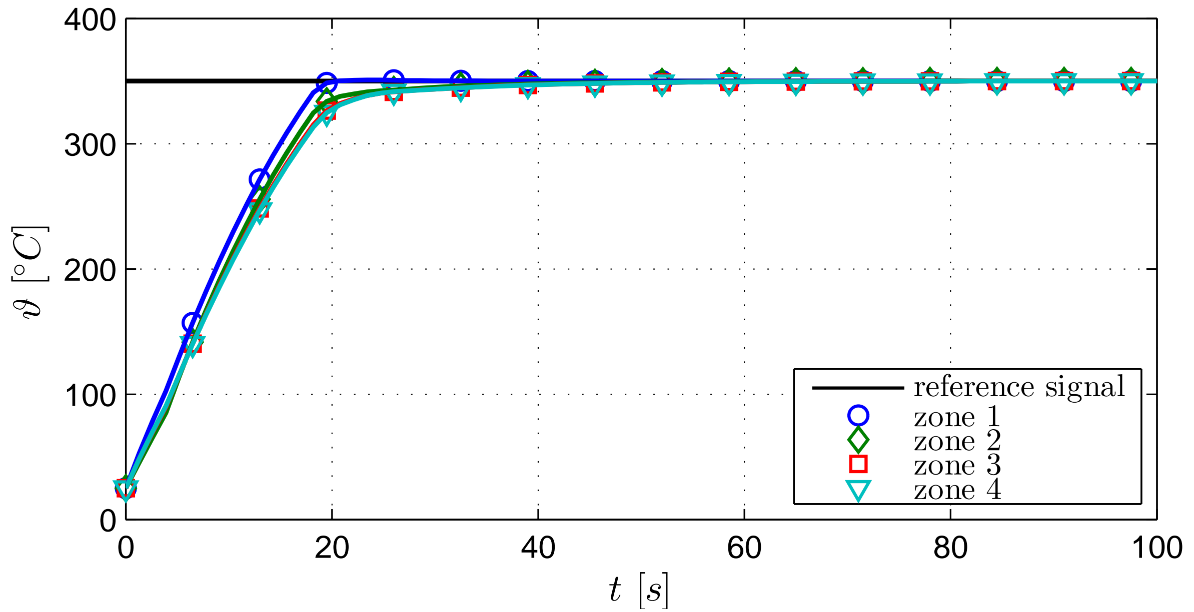

(b) Zone temperatures

Figure 2.33: Simulated heat-up of a "highly doped" wafer: An extended state feedback controller is tested with the help of a numerical simulation. The well-known observer technique is used to prevent the effect of controller windup.

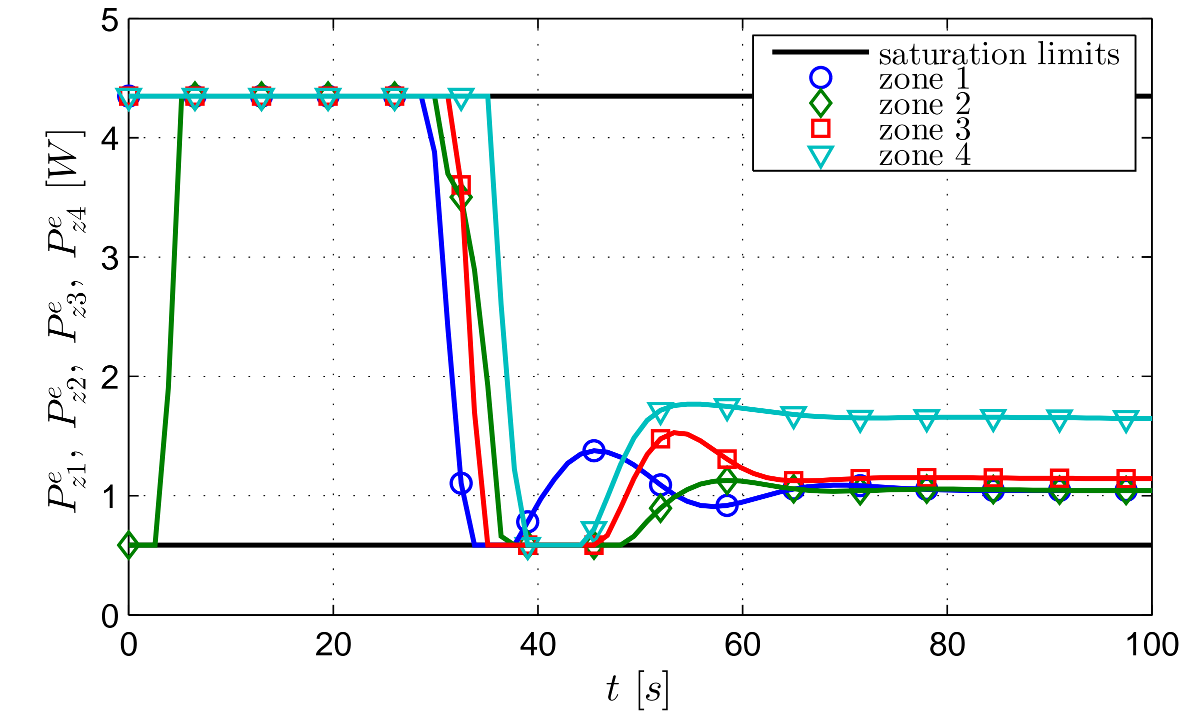

(a) Electrical power supplied to LEDs

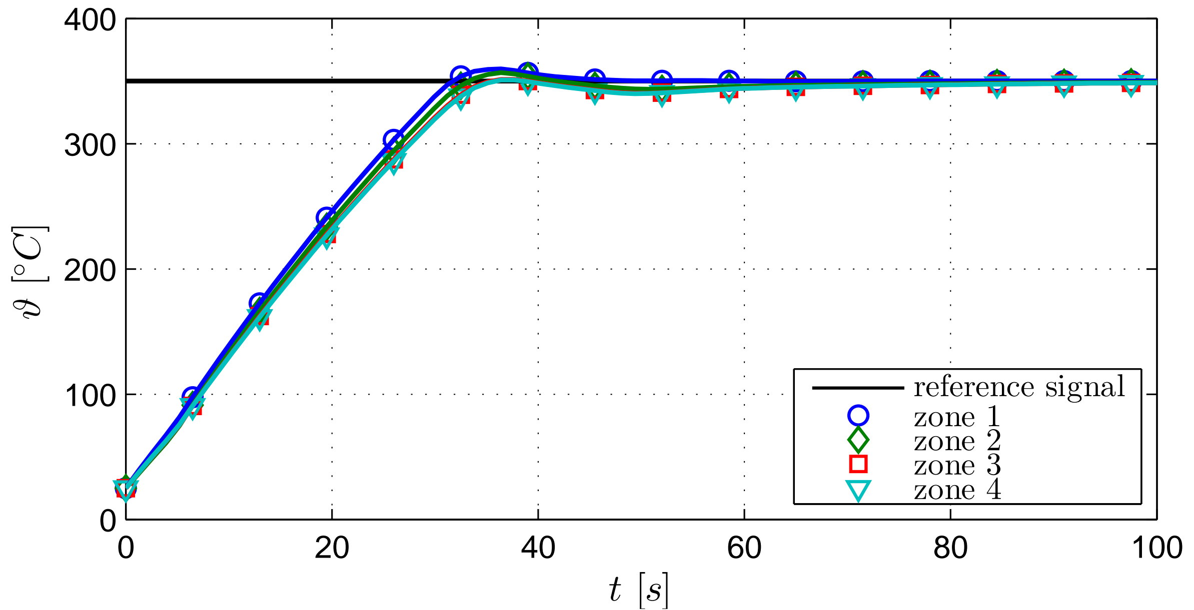

(b) Zone temperatures

Figure 2.34: Simulated heat-up of a "bare silicon" wafer: The proposed approach can be used to control the surface temperature of the wafer regardless of the wafer type. The actuating signals are kept within the saturation limits.

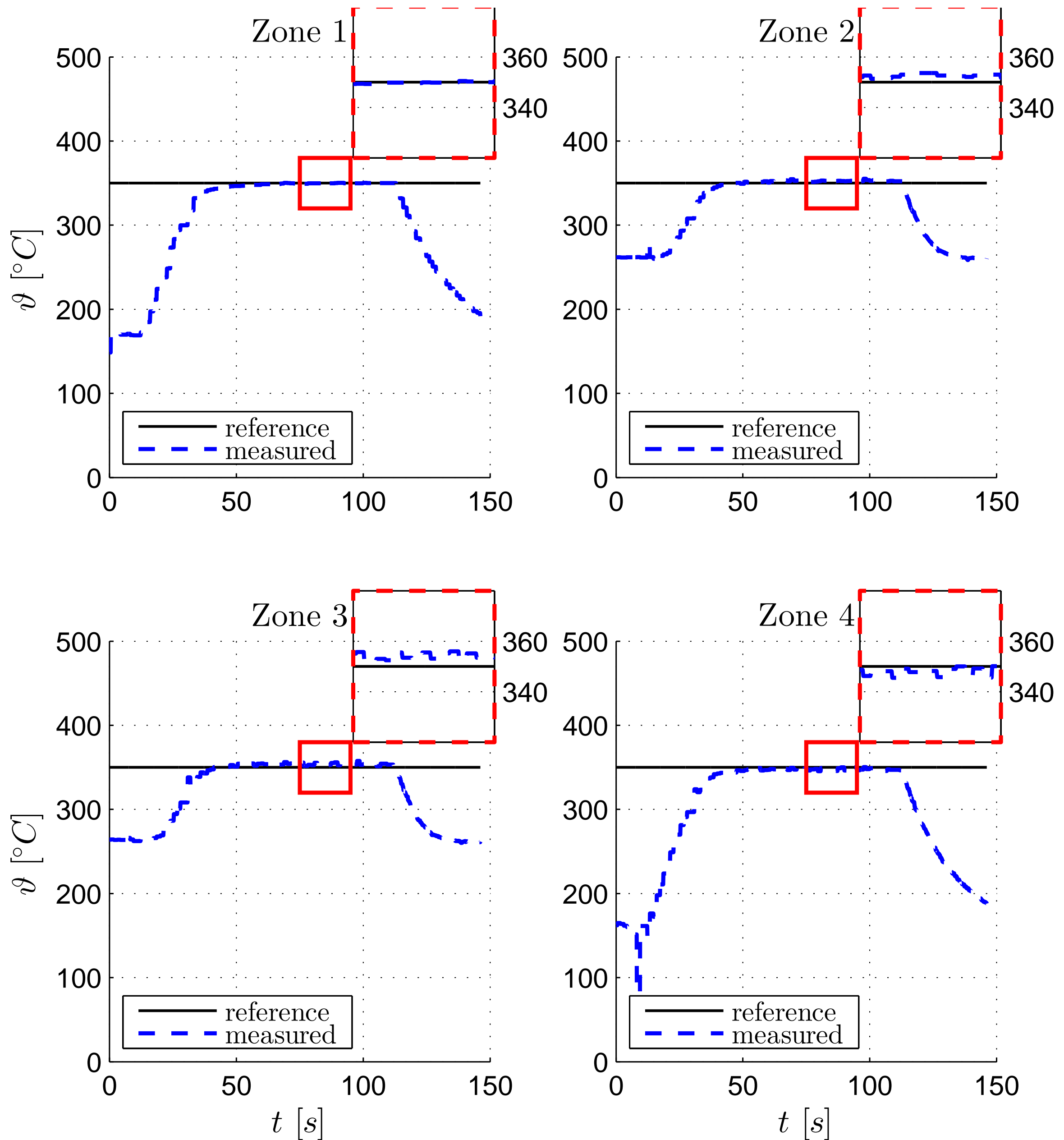

Figure 2.35: Heat-up experiment with a “highly doped” wafer: An extended state feedback controller is used to heat up a highly doped wafer to a temperature of 350 $^\circ C$. The hardware setup is divided into four heating zones, whereas the temperature at the radial midpoint in zone 1 is measured with the help of a pyrometer. An observer is used to estimate the remaining three zone temperatures. The measured and estimated zone temperatures serve as a feedback for the controller.

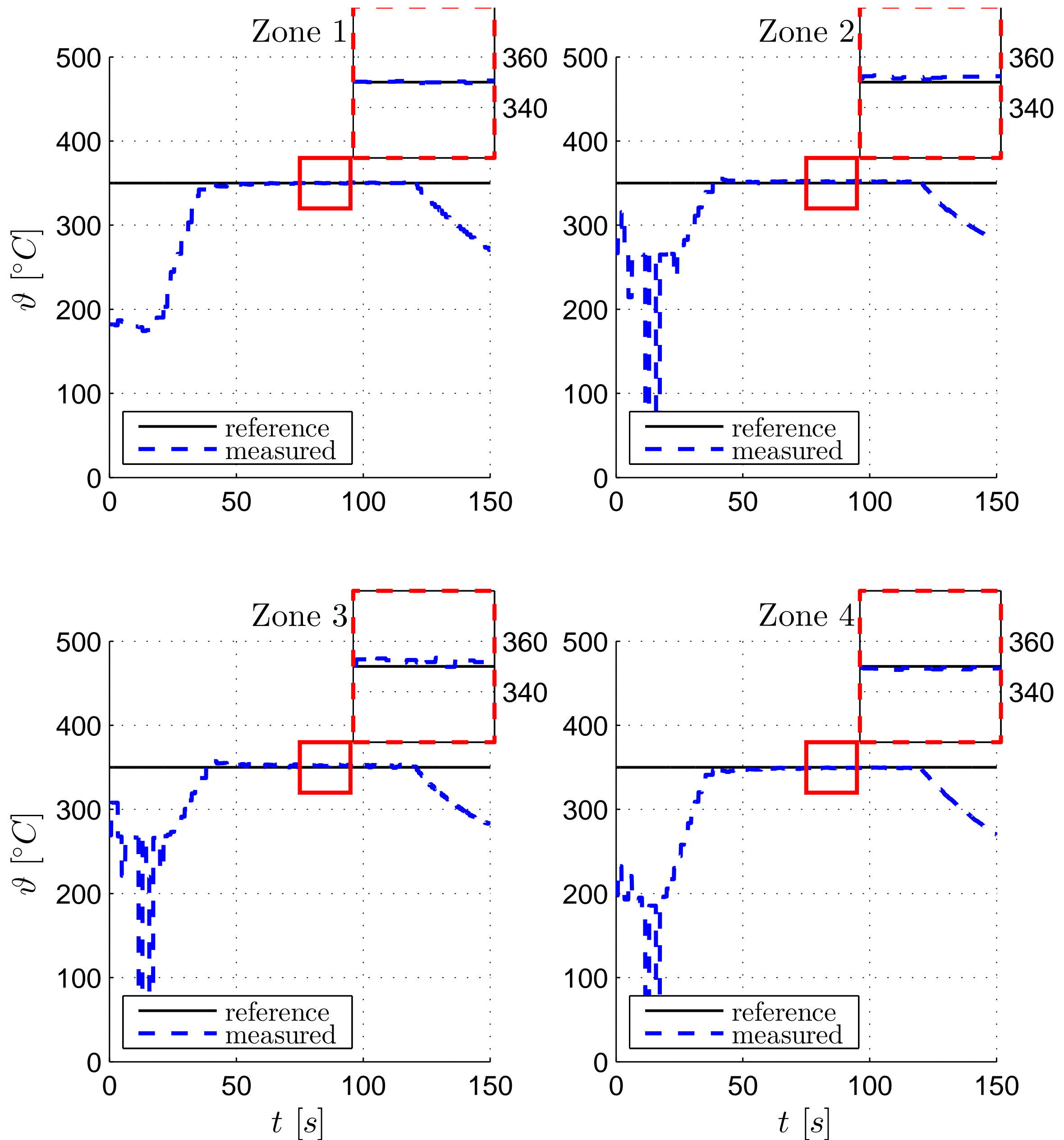

Figure 2.36: Heat-up experiment with a "bare silicon" wafer: A test rig equipped with four contactless temperature sensors in each heating zone is used to verify the performance of the proposed extended state feedback control law. At future production tools just one pyrometer in zone 1 will be available. The temperatures in the remaining heating zones will be estimated with the help of the proposed late-lumping observer with measurement injection. The experiments point out that the designed controller in combination with the observer can be used to heat up a silicon wafer independent of its dopand level. The accuracy is identified as less than $\pm$ 10 $°C$, which is known to be accurate enough to uniformly treat the wafer surface with highly reactive gasses.

2.7 Conclusion

In this chapter, the design of a state observer to estimate the temperature profile of a wafer, which is heated up with a large number of high-power LEDs, is discussed. A physical plant model is derived and discretized in space with the so-called vertical method of lines. The resulting nonlinear, affine-input system is linearized around the estimated state vector in every sampling instance, which provides a linear time-varying system. For this system, a Luenberger observer based on the LQR approach and a Kalman filter are designed and verified with the help of numerical simulations as well as at a laboratory plant.

The so-called early-lumping approach, where the partial differential system is discretized in space before the observer design step, leads to a high-order finite-dimensional system, for which the online calculation of the observer gain is computationally intensive. Therefore, an alternative late-lumping observer approach is applied, which directly deals with the partial differential system. The derived observer, which is not discretized before the implementation phase, is verified with the help of numerical simulations and compared to the "standard approach" on a test rig.

The estimated zone temperatures of the wafer are used as a feedback for a controller, which is designed in such a manner that it is able to cope with unknown disturbances and modeling uncertainties. Among a disturbance rejection approach, the proposed controller involves a systematic procedure to avoid the well-known effect of controller windup. Closed-loop tests verify that the controller can be used to heat up wafers of diverse types. The achieved accuracy lies within $\pm 10\ ^{\circ}C$ with respect to the reference signal, which is known to be sufficient to achieve desired process results on the wafer.

3 Post-clean step - design of a point of use mixing system

In order to remove residues that have been deposited on the wafer after an etching step or a photoresist stripping process, selected solutions are applied to the rotating wafer. State of the art spin wet clean tools use tanks that are filled with desired chemicals in a predefined mixing ratio. This mixture is permanently circulated through a heater and a cooler to maintain a desired temperature. Furthermore, the pressure within the recirculation line is kept at a nearly constant value. The flow rates to the process chambers are adjusted manually using needle valves.

3.1 Problem formulation

A tank-based supply system has the disadvantage that varying the process parameters, i.e. outlet flow rates, temperature and mixing ratio of the solution, requires either high maintenance or long-running routines. A change of process parameters from wafer to wafer or even during the processing of a wafer is not possible. However, chip manufacturers want to do exactly that with future wet clean equipment. To increase the flexibility provided by future tools, a novel point of use mixing system is designed to mix the solution "online" with a desired mixing ratio, temperature and outlet flow rates. With such a mixing system, it is also possible to change the process parameters while processing a wafer. A schematic representation of the point of use mixing system is shown in Figure 3.1.

The main component of the point-of-use mixing system is the so-called liquid flow controller (LFC). The hardware used for an LFC is shown in Figure 3.2. A flowmeter measures the current flow rate in the piping. It is followed by an air-operated valve, referred to as "pressure regulator". The pressure loss across this component can be adjusted by changing its control air pressure. To set a desired control air pressure, a so-called "electro-pneumatic converter" is used, which is a device for controlling the outlet air pressure in proportion to an electric current signal. The initial design of the LFC is discussed in detail in [Kleindienst, 2013]. The proposed control strategy is a combination of compensating the present input-nonlinearity and a PI controller. In addition, a Smith predictor is used to take into account the constant dead time of the plant.

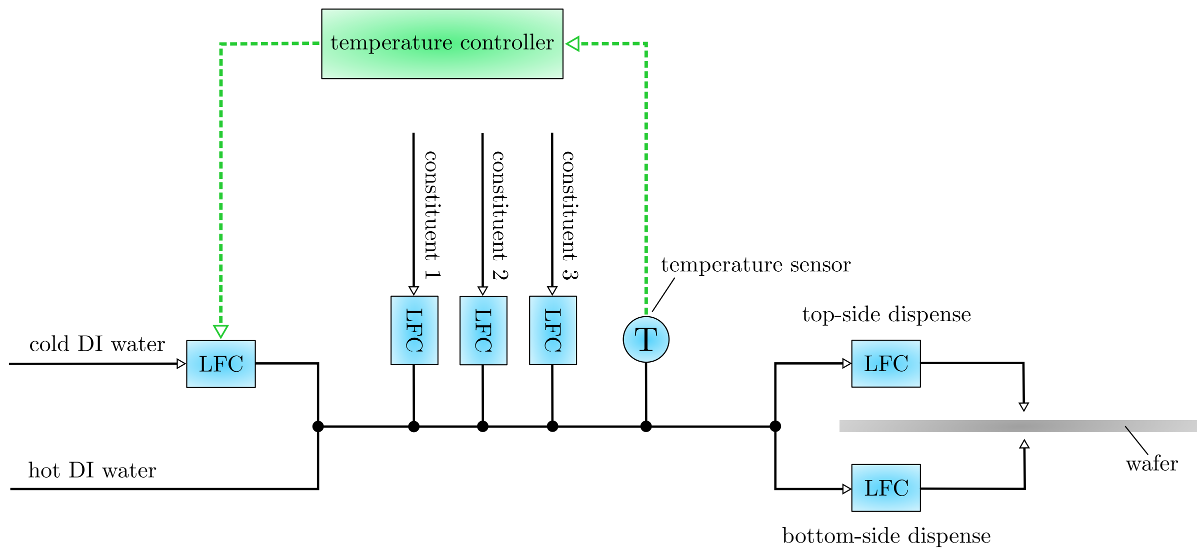

Figure 3.1: Schematic representation of the point of use mixing system: Cold and hot deionized (DI) water as well as up to three chemical constituents are mixed "online" in a defined ratio to obtain a desired mixing ratio and temperature. The outlet flow rates can also be adjusted with the help of feedback loops.

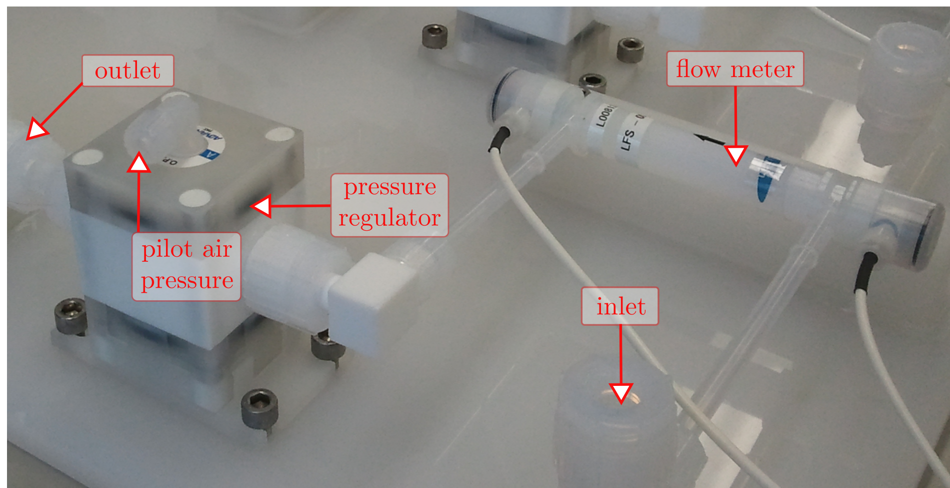

Figure 3.2: Hardware setup of an LFC: The actuating signal is converted to a pilot air pressure, which is fed to the pressure regulator. The pilot air pressure acts via a diaphragm against a spring and adjusts the aperture within the flow path. The flow rate over the pressure regulator correlates with the pressure loss over the orifice. A flowmeter is used to measure the actual flow rate through the LFC system.

A point of use mixing system contains up to six LFCs, i.e. one for cold water, one for each injection of highly concentrated chemicals and one each for applying the mixture on top and on the bottom side of the wafer.

3.2 Plant description and mathematical model

The desired dispense flow rates, the mixing ratio of the solution (water relative to the three highly concentrated chemicals) and the desired temperature define the required flow rates for the single LFCs. The required amount of cold water is added to the solution with the help of an LFC, whereas the remaining amount of hot water is added automatically due to the selected pressure conditions. The reference signal for the cold water LFC is provided by an overlain temperature controller.

3.2.1 Blending of constituents

In a first step, the blending of cold and hot water as well as the three highly concentrated constituents is considered in terms of their internal energy. More precisely, a mathematical relation is sought to compute the required flow rate of cold water such that the mixture shows a desired temperature.

The amount of heat energy transferred to or from an object is proportional to its mass m and to its increase or decrease in temperature denoted by the temperature difference $\Delta\vartheta$, i.e.

$$\Delta Q = c\ m\ \Delta\vartheta. \tag{3.1}$$

Therein, ΔQ denotes the transferred quantity of heat and c denotes the specific heat capacity. Applying (3.1) to the five inlets of the mixing system with respect to the resulting temperature of the mixture, denoted by ϑ_m, yields

$$\begin{aligned}
\Delta Q_h &= c_h m_h (\vartheta_m - \vartheta_h), \\
\Delta Q_c &= c_c m_c (\vartheta_m - \vartheta_c), \\
\Delta Q_{p1} &= c_{p1} m_{p1} (\vartheta_m - \vartheta_{p1}), \\
\Delta Q_{p2} &= c_{p2} m_{p2} (\vartheta_m - \vartheta_{p2}), \\
\Delta Q_{p3} &= c_{p3} m_{p3} (\vartheta_m - \vartheta_{p3}).
\end{aligned} \tag{3.2}$$

The indices h (for “hot”), c (for “cold”), $p1$ (for “part stream 1”), $p2$ (for “part stream 2”) and $p3$ (for “part stream 3”) are introduced to distinguish the physical quantities of the five inlets.

Due to the conservation of energy it holds

$$\begin{aligned} 0 &= \Delta Q_h + \Delta Q_c + \Delta Q_{p1} + \Delta Q_{p2} + \Delta Q_{p3} \\ &= c_h m_h(\vartheta_m - \vartheta_h) + c_c m_c(\vartheta_m - \vartheta_c) + c_{p1} m_{p1}(\vartheta_m - \vartheta_{p1}) \\ &\quad + c_{p2} m_{p2}(\vartheta_m - \vartheta_{p2}) + c_{p3} m_{p3}(\vartheta_m - \vartheta_{p3}). \end{aligned} \tag{3.3}$$

Differentiating (3.3) with respect to time and assuming that the in- and outlet temperatures as well as the heat capacities are constant results in

$$\begin{aligned} 0 &= c_h \dot{m}_h(\vartheta_m - \vartheta_h) + c_c \dot{m}_c(\vartheta_m - \vartheta_c) + c_{p1} \dot{m}_{p1}(\vartheta_m - \vartheta_{p1}) \\ &\quad + c_{p2} \dot{m}_{p2}(\vartheta_m - \vartheta_{p2}) + c_{p3} \dot{m}_{p3}(\vartheta_m - \vartheta_{p3}). \end{aligned} \tag{3.4}$$

Since the densities of the inlet liquids can also be assumed to be constant over the considered temperature range, the mass changes can be replaced by flow rates ϕ, i.e.

$$\begin{aligned} \dot{m}_h &= \rho_h \phi_h, \\ &\vdots \\ \dot{m}_{p3} &= \rho_{p3} \phi_{p3}. \end{aligned} \tag{3.5}$$

This leads to

$$\begin{aligned} 0 &= c_h \rho_h \phi_h(\vartheta_m - \vartheta_h) + c_c \rho_c \phi_c(\vartheta_m - \vartheta_c) + c_{p1} \rho_{p1} \phi_{p1}(\vartheta_m - \vartheta_{p1}) \\ &\quad + c_{p2} \rho_{p2} \phi_{p2}(\vartheta_m - \vartheta_{p2}) + c_{p3} \rho_{p3} \phi_{p3}(\vartheta_m - \vartheta_{p3}). \end{aligned} \tag{3.6}$$

Due to the continuity equation, the flow rate of hot water can be expressed by

$$\phi_h = \phi_m - \phi_c - \phi_{p1} - \phi_{p2} - \phi_{p3}, \tag{3.7}$$

where ϕ_m is the total flow rate of the mixture[1]. Inserting (3.7) into (3.6) and solving for ϕ_c finally yields

$$\phi_c = \frac{\begin{aligned} c_h \rho_h(\phi_m - \phi_{p1} - \phi_{p2} - \phi_{p3})(\vartheta_m - \vartheta_h) + c_{p1} \rho_{p1} \phi_{p1}(\vartheta_m - \vartheta_{p1}) \\ + c_{p2} \rho_{p2} \phi_{p2}(\vartheta_m - \vartheta_{p2}) + c_{p3} \rho_{p3} \phi_{p3}(\vartheta_m - \vartheta_{p3}) \end{aligned}}{c_h \rho_h(\vartheta_m - \vartheta_h) - c_c \rho_c(\vartheta_m - \vartheta_c)}. \tag{3.8}$$

The obtained mixing formula (3.8) involves the heat capacities and densities of all five inlet fluids. However, it is very often the case that the constituents itself consist primarily of water (e.g. a typical dilution of hydrogen peroxide consists of 70% water) or they are at least water-like chemicals. Thus, it may be often appropriate to assume that all heat capacities and all densities are equal, i.e.

$$c_h = c_c = c_{p1} = c_{p2} = c_{p3} \tag{3.9}$$

[1] ϕ_m denotes the total dispense flow rate, i.e. the sum of the top-side and the bottom-side flow rate.

and

$$\rho_h = \rho_c = \rho_{p1} = \rho_{p2} = \rho_{p3}. \tag{3.10}$$

In this case, equation (3.8) simplifies to

$$\phi_c = \frac{\begin{array}{r}(\phi_m - \phi_{p1} - \phi_{p2} - \phi_{p3})(\vartheta_m - \vartheta_h) + \phi_{p1}(\vartheta_m - \vartheta_{p1}) \\ + \phi_{p2}(\vartheta_m - \vartheta_{p2}) + \phi_{p3}(\vartheta_m - \vartheta_{p3})\end{array}}{\vartheta_c - \vartheta_h}. \tag{3.11}$$

Thus, the required amount of cold water to obtain an expected temperature of the mixture at given flow rates and inlet temperatures can be calculated. To handle unmodeled disturbances and uncertainties, an overlain temperature controller is intended to adjust the reference signal for the cold water flow rate in case of a temperature deviation.

3.2.2 Liquid flow controller

The initial design of the LFC is based on the assumption that the pressure as well as the temperature conditions at the inlet and the outlet of the system are constant. In this case, a steady-state relation between the actuating signal u and the outlet flow rate y can be identified. This relation can be interpreted as a static input-nonlinearity of the plant. The initial implementation of the LFC contains an automated procedure to measure and store the input-nonlinearity in a lookup table (LUT), which is then used for compensation. A PI controller with Smith predictor is applied to the remaining linear system.

This approach has proven itself in case that the in- and outlet conditions in terms of pressure and temperature are almost constant. Unfortunately, this is not the case with the point of use mixing system, where several liquids are mixed together. For example, the pressure at the outlet of a constituent LFC, which injects into the so-called main stream, is highly dependent on the flow rate in the main stream. Figure 3.3 compares two LUTs of a constituent LFC measured at contrary main stream conditions. It points out that a change in the main stream conditions does not significantly affect the shape of the LUT (aside from the maximal reached flow rate). On the other hand, a change in the main stream conditions shifts the LUT significantly along the axis of the abscissas. This may have a severe impact on the control performance in case that the stored LUT to compensate the input-nonlinearity does not reflect the real-world behavior of the system. Figure 3.4 depicts the result of a numerical simulation, where a oscillation around the reference signal occurs, because the controller uses the red curve shown in Figure 3.3 for compensation, but the input-nonlinearity of the plant is simulated with the black curve.

To conclude, the compensation of the plant's input-nonlinearity is advisable if the in- and outlet conditions at the LFC system do not change significantly. Otherwise, this approach

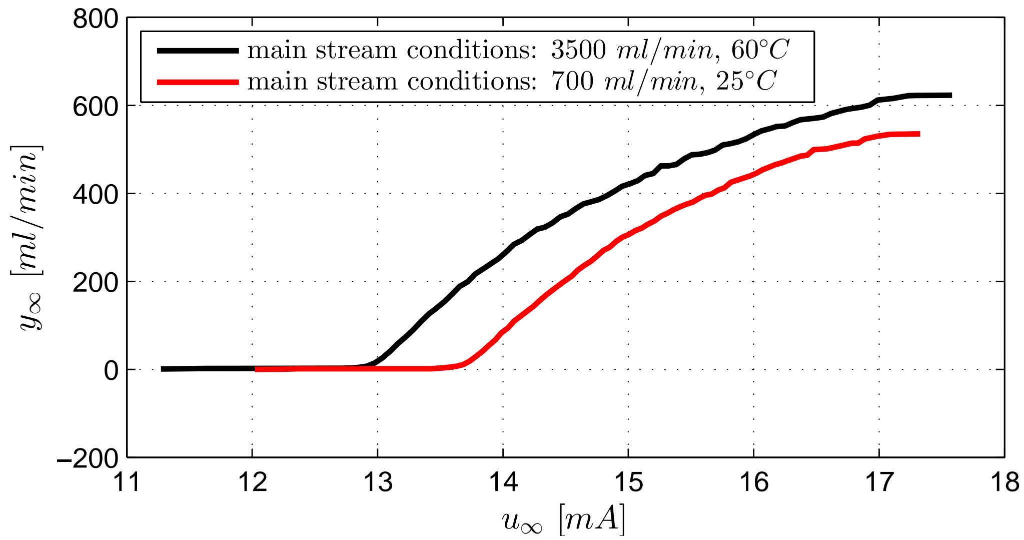

Figure 3.3: Lookup tables of constituent LFC measured at two different main stream conditions: Changing the main stream conditions of the point of use mixing system results in a shift of the steady-state flow rate along the x-axis.

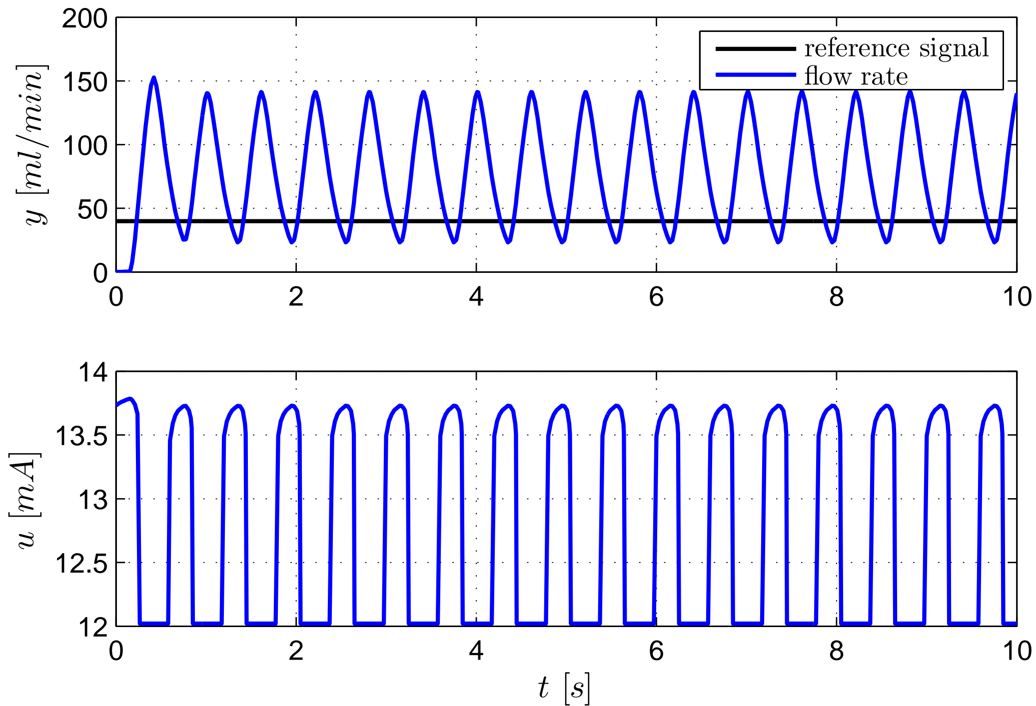

Figure 3.4: LFC simulation with improper lookup table: Using the improper lookup table to compensate the plant's input-nonlinearity leads to an undesirable control behavior.

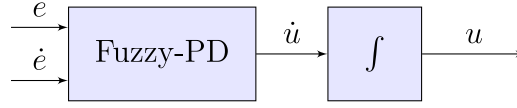

Figure 3.5: Fuzzy-PI controller: A Fuzzy-PD block, whose inputs are the control error and its derivative, is followed by an integrator. This incremental form entails a good disturbance suppression by integrating $\dot{u}$. Furthermore, the effect of controller windup can be prevented easily by stopping the integrator in case that the actuating signal is outside of its saturation limits.

may lead to an undesired control performance. Thus, this section discusses a different control approach, namely a Fuzzy-PI controller [Jantzen, 2013]. This type of controller can be directly designed for the nonlinear plant, i.e. the input non-linearity does not have to be compensated. The designed controller is realized in the so-called incremental form, see Figure 3.5. Due to the present integral action, the controller vanishes a steady state control error in case of a constant reference signal and constant disturbances.

The two inputs of the controller are the error signal e, which is defined as the difference between the reference signal and the measured flow rate, and its derivative with respect to time denoted by $\dot{e}$. The output of the Fuzzy-PD block is the derivative of the actuating signal with respect to time, i.e. $\dot{u}$. For the so-called fuzzification of the two inputs as well as for the output membership functions are introduced as shown in Figure 3.6. The error signal is given as a percentage of the maximal readable flow rate and the derivative of the control signal is given in amperes per second. For the AND operation of the two inputs, the algebraic product is used [Jantzen, 2013]. So-called "singletons" of a "Takagi-Sugeno" system [Takagi and Sugeno, 1985] are used to implement the membership functions of the output. The defuzzification is realized via the weighted average, i.e. the derivative of the control signal computes as

$$\dot{u} = \frac{\sum\limits_{i=1}^{k} \mu_i s_i}{\sum\limits_{i=1}^{k} \mu_i}. \tag{3.12}$$

The number of rules is denoted by k, μ_i is the resulting membership value of the AND operation of the ith rule and s_i is the corresponding value of the singleton. The list of rules is summarized in Table 3.1 and the used abbreviations are listed in Table 3.2.

The designed Fuzzy-PI controller is applied to the point of use mixing system, which is built on a laboratory tool. Please note that deviating from Figure 3.1, only two highly concentrated part streams are built up instead of three. Figure 3.7 shows the performance of the two dispense LFCs as well as the two constituent LFCs. The top-side flow rate is changed stepwise from 2000 ml/min to 750 ml/min and the bottom-side flow rate is

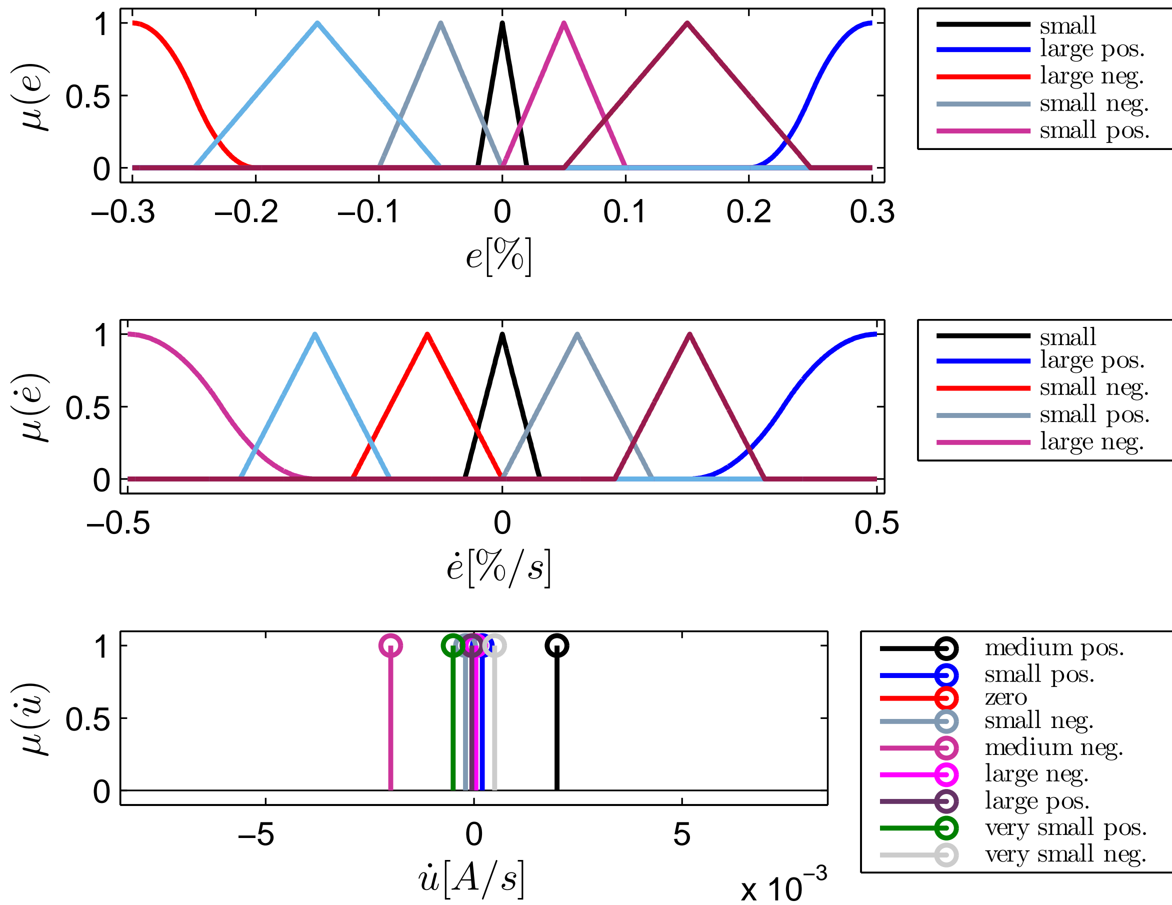

Figure 3.6: Fuzzification: Membership functions are chosen for the two inputs e and $\dot{e}$ as well as for the output $\dot{u}$.

$\dot{u}$		e				
		ln	**sn**	**s**	**sp**	**lp**
$\dot{e}$	**ln**	ln	mn	sn	vsn	mp
	sn	ln	mn	vsn	z	lp
	s	ln	sn	z	sp	lp
	sp	ln	z	vsp	mp	lp
	lp	mn	vsp	sp	mp	lp

Table 3.1: Fuzzy-PI, table of rules: The two inputs are each assigned five membership functions. The table assigns the input membership functions the respective membership function for the output.

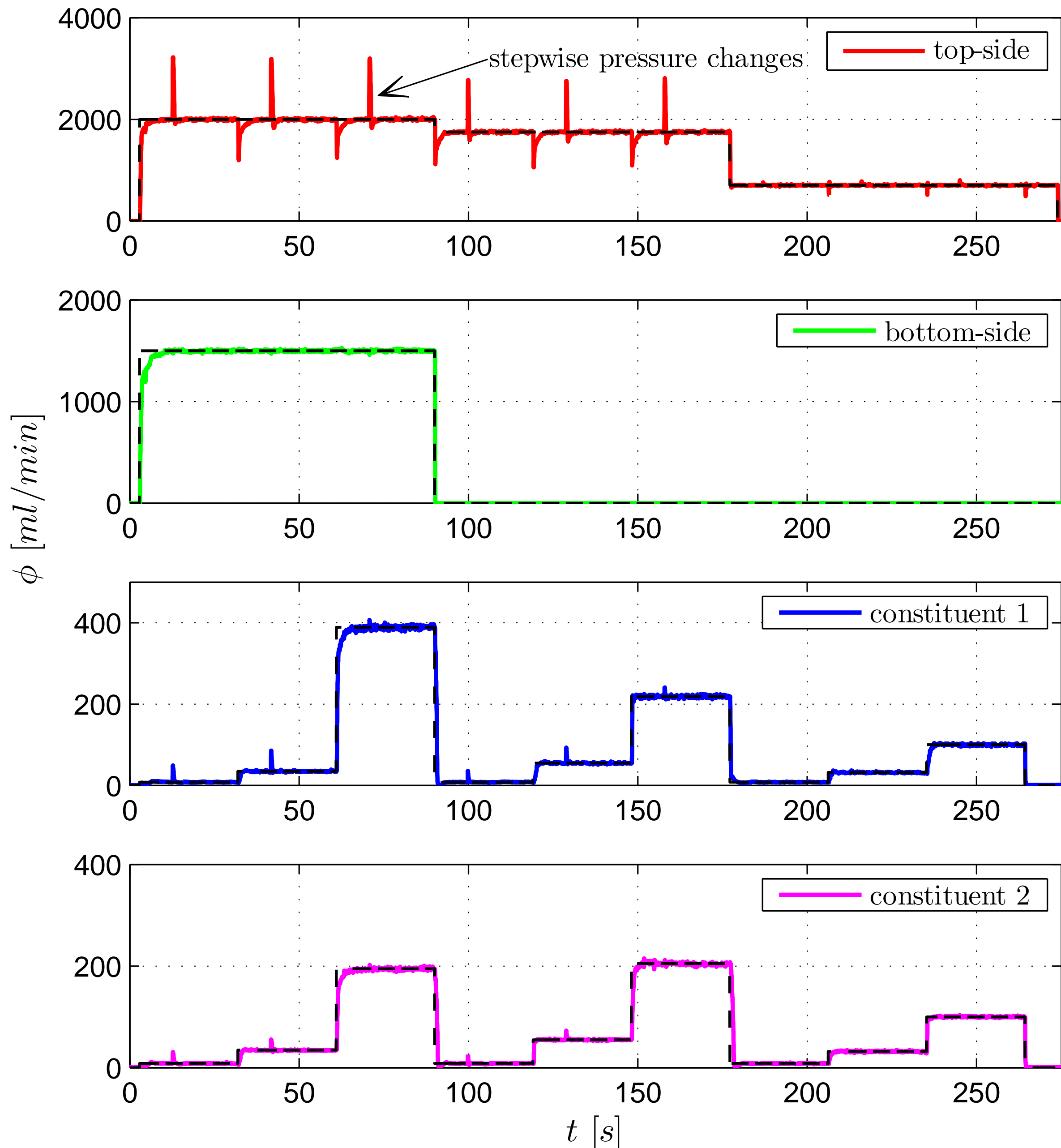

Figure 3.7: Point of use mixing system with LFCs based on a Fuzzy-PI controller: The developed mixing system can be used to create a mixture with a desired chemical concentration. Based on the desired output flow rates for top-side and bottom-side dispense to the wafer as well as the targeted concentration of the mixture, the corresponding reference signals for the LFCs for the insertion of highly concentrated constituents are calculated. Depending on the main stream flow rates, the back pressure for these constituent LFCs changes.
The test demonstrates that with the aid of the Fuzzy-PI controller, the reference signals (black dashed lines) can be tracked with convincing performance regardless of the changing pressure conditions.

	Abbreviation	Meaning
$e,\ \dot{e}$	ln	large negative
	sn	small negative
	s	small
	sp	small positive
	lp	large positive
$\dot{u}$	ln	large negative
	mn	medium negative
	sn	small negative
	vsn	very small negative
	z	zero
	vsp	very small positive
	sp	small positive
	mp	medium positive
	lp	large positive

Table 3.2: Fuzzy-PI, abbreviations

changed from 1500 ml/min to zero. The reference signals for the two constituent LFCs are calculated according to typical mixing ratios.

The test indicates that the LFCs based on the designed Fuzzy-PI controller show a proper performance, i.e. the constituent LFCs are able to control the requested flow rates independent of the main stream conditions. Furthermore, the disturbance rejection capability is tested at the top-side LFC by changing the fluid resistance within the piping abruptly. This is carried out by switching from a small dispensing nozzle to a larger one and vice versa. It can be seen that the applied disturbance can be rejected quickly. Furthermore, one recognizes also that the changed back pressure in the main stream also makes itself felt on the constituent LFCs. Again, the disturbance rejection here is very satisfactory.

3.2.3 Temperature sensor dynamics

To measure the temperature of the mixture, the point of use mixing system is equipped with a temperature sensor. Its dynamic behavior can be sufficiently modeled with the help of the first-order transfer function

$$P_s(s) = \frac{1}{1 + 0.45s}, \tag{3.13}$$

where s denotes the complex Laplace-variable. Figure 3.8 compares a measured temperature step response from approximately 20 to 60 $^\circ C$ with the simulated one. Please

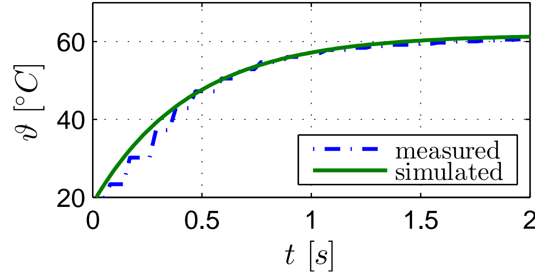

Figure 3.8: Mathematical model of temperature sensor: The dynamic behavior of the temperature sensor can be modeled sufficiently with the help of a transfer function of order one.

note that the gain of the transfer function and the initial temperature value have been adjusted for the comparison.

3.2.4 Transport delay

The dead time L_{Tmix} between the time instance when changing the reference signal to the cold water LFC and the time instance when the temperature sensor detects a temperature change mainly depends on the transport time of the liquid. Provided that the pipe between the actuator for the cold water stream and the mixing point is fully filled with cold water when changing the reference signal to the cold water LFC, the dead time can be computed based on the involved flow rates and pipe volumes $V_{p1}, V_{p2}, V_{p3}, V_{p4}$ as illustrated in Figure 3.9. Thus, the overall dead time of the point of use mixing system computes as

$$L_{Tmix} = L_{Lfc} + \frac{V_{p1}}{\phi_m - \phi_{p1} - \phi_{p2} - \phi_{p3}} + \frac{V_{p2}}{\phi_m - \phi_{p2} - \phi_{p3}} + \frac{V_{p3}}{\phi_m - \phi_{p3}} + \frac{V_{p4}}{\phi_m}, \qquad (3.14)$$

where L_{Lfc} denotes the dead time of the cold water LFC.

3.3 Temperature control

The previous considerations can be used to compose a plant model to design the temperature controller for the point of use mixing system. As Figure 3.10 shows, the reference signal to the cold water LFC serves as the input signal to the plant. As a measured step response of a constituent LFC plotted in Figure 3.11 reveals, the dynamic behavior of the

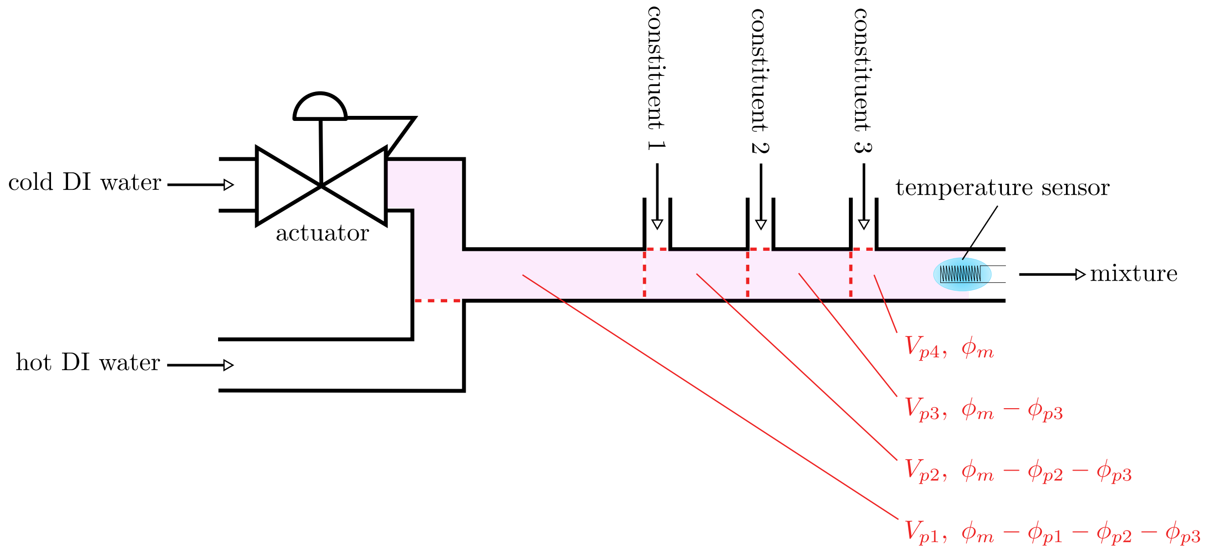

Figure 3.9: Dead time schematic: The dead time of the point of use mixing system is mainly caused by the transport duration of the liquid from the cold water actuator to the temperature sensor.

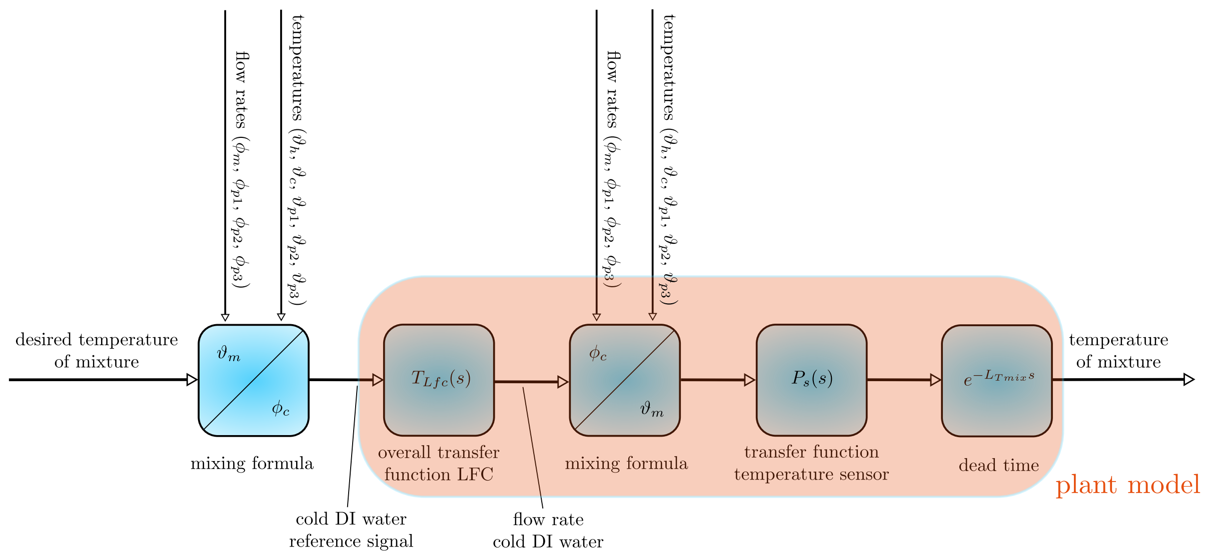

Figure 3.10: Overall plant model with inversion of mixing formula: The overall plant model describing the dynamic behavior between the reference signal for the cold water LFC and the outlet temperature of the point of use mixing system is used to design a controller. The obtained mixing formula ahead of the plant model is a part of the overall temperature controller.

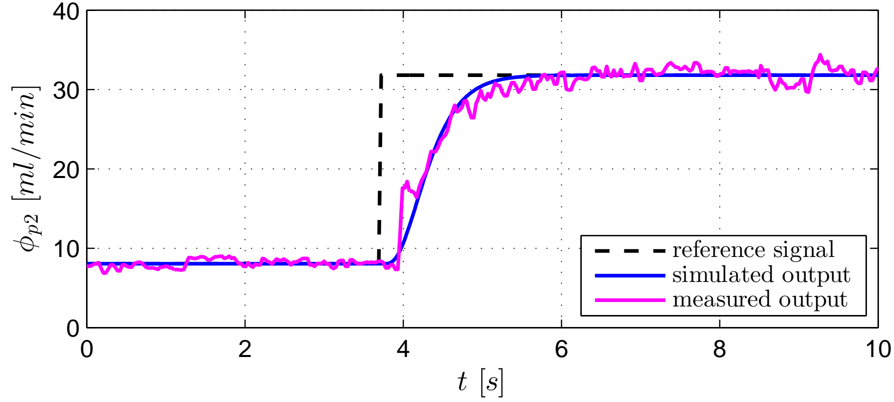

Figure 3.11: Constituent LFC: A measured closed-loop step response is compared to the simulated one.

LFC can be sufficiently approximated by the transfer function[2]

$$T_{Lfc}(s) = \frac{1}{(1+0.2s)^3}. \tag{3.15}$$

The cold water flow rate is then converted to the calculated outlet temperature by applying a rearranged form of the mixing formula (3.11). Transfer function (3.13) models the dynamic behavior of the temperature sensor and the dead time of the overall plant model is given in equation (3.14).

The proposed structure of the temperature controller for the point of use mixing system is a combination of the mixing formula (3.11) and a PI controller with Smith predictor [Smith, 1959]. The mixing formula is used to compensate the static conversion from the cold water flow rate to the outlet temperature. Hence, the remaining overall linear plant model used for the controller design can be written as

$$P_{Tmix}(s) = T_{Lfc}(s)P_s(s)e^{-L_{Tmix}s} = \frac{e^{-L_{Tmix}s}}{(1+0.2s)^3(1+0.45s)}. \tag{3.16}$$

The Smith predictor is used in order to cope for the known dead time. For the obtained plant model without taking into account the dead time, a PI controller

$$C_{Tmix}(s) = \frac{0.25s+0.8}{s} \tag{3.17}$$

is designed based on bode plots.

[2]Since the dead time of the LFC is already considered in equation (3.14), its transfer function is given without dead time.

3.4 Laboratory experiment and conclusion

The temperature controller designed in Section 3.3 in combination with the LFCs based on the Fuzzy-PI controller designed in Section 3.2.2 are implemented at a laboratory tool. The used hardware is depicted in Figure 3.12. It is evident that the novel point of use mixing system can be built much more compact than the conventional tank-based distribution system. The experiment depicted in Figure 3.13 demonstrates the

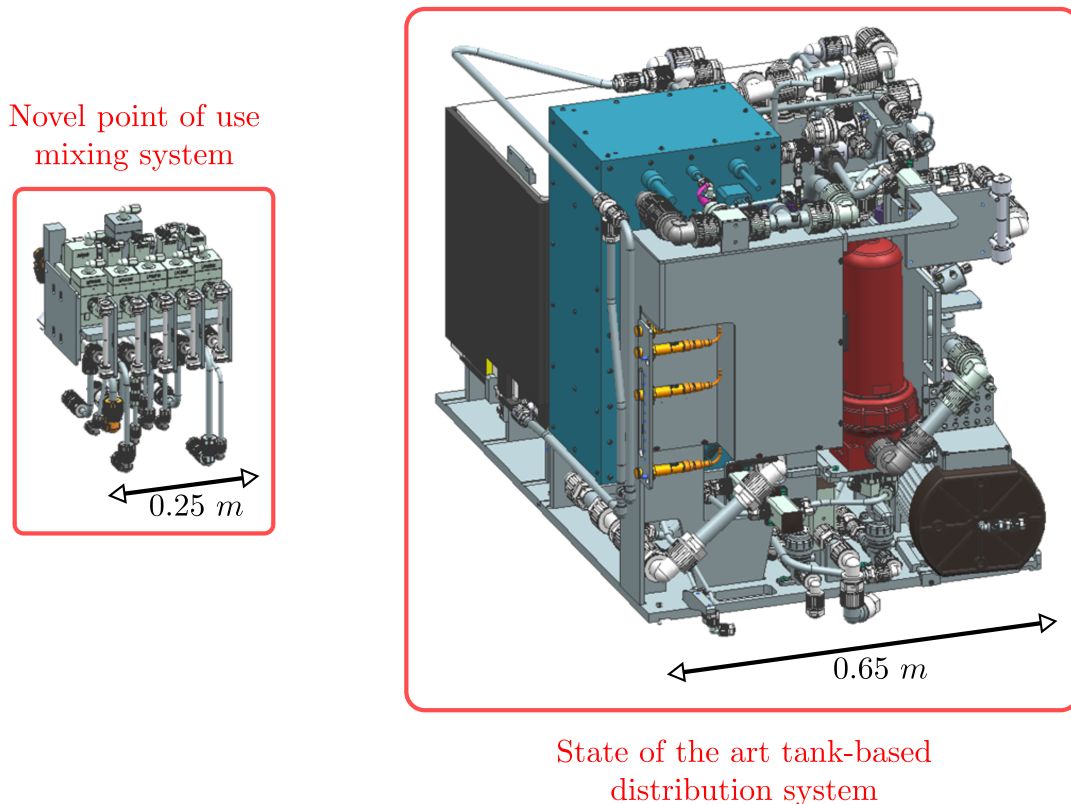

Figure 3.12: Hardware design of the point of use mixing system: The novel mixing system consumes much less space than the state of the art tank-based distribution system. The number of required components can also be reduced significantly.

powerfulness of the point of use mixing system. It shows that it is possible to change the process parameters, i.e. outlet flow rates, temperature and mixing ratio of the solution, during the process of a wafer. This gain in flexibility will allow process engineers to optimize the on-wafer performance significantly in future. A prospective use case of now possible flow rate ramps as well as temperature ramps is to synchronize these changes with the movement of the chemical dispenser. This will enable to control the etch rate across the wafer diameter for the first time. First point of use mixing systems are already installed at customer tools and show promising results.

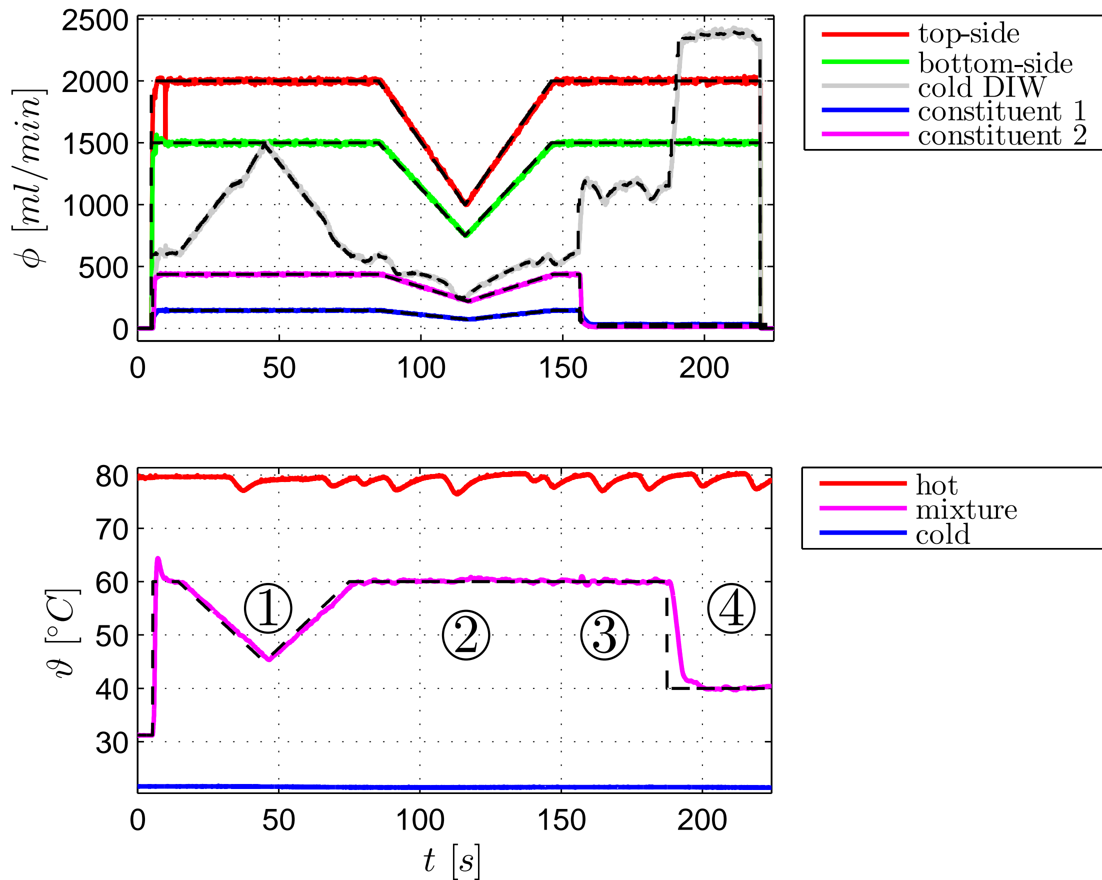

Figure 3.13: Point of use mixing including temperature control: The novel mixing system allows to change the process parameters during the process of a wafer. Black dashed lines are used to plot the reference signals. Possible use cases of the point of use mixing system are: ① Change the temperature at a constant mixing ratio and constant outlet flow rates. ② Maintain a constant temperature as well as a constant mixing ratio, while changing the outlet flow rates. ③ Change the mixing ratio stepwise, while keeping the temperature as well as the outlet flow rates constant. ④ Carry out a stepwise temperature change, while keeping the mixing ratio and the outlet flow rates constant.

4 Summary and outlook

The present work deals with control concepts for the next generation of single-wafer spin clean tools. It is divided into two main parts.

The first part of the thesis discusses the stripping of hard-baked photoresist on the wafer surface. State of the art processes use massive amounts of solutions containing sulfuric acid to etch off the photoresist by dispensing the solution onto the rotating wafer. Since the usage of sulfuric acid is on the one hand expensive and on the other hand harmful to the environment, the chip manufacturers are searching forcefully for an alternative process. The approach presented in this thesis discusses a novel process, which is using ozone gas to break the photoresist structure. One of the main challenges to enable this process is the uniform heat-up of the wafer without contacting its surface. This is carried out with a large number of high-power LEDs, whose emitted light is absorbed by the wafer. A closed-loop approach to control the wafer's temperature requires the latter to be available for feedback. For this, different observer approaches are presented, which allow to estimate the temperature profile of the wafer surface by using just one contactless temperature sensor. Based on the estimated temperatures, possible concepts are proposed to control the wafer's temperature. Numerical simulations and experiments at a real world heating system emphasize the achieved performance of the presented approaches.

The second part deals with the design of a point of use mixing system, which is intended to be used to float off the broken photoresist with well-defined solutions. Instead of utilizing a state of the art tank-based chemical supply system, a novel point of use mixing system is proposed to mix the desired solution online. Such a point of use mixing system uses several so-called "liquid flow controllers" (LFCs) to adjust the flow rates at the inlets as well as at the outlets of the mixing system. An existing control approach for the LFCs is discussed. Moreover, a robust solution, which is capable to suppress fluctuations of the pressure at the in- and outlet of the LFC, is proposed. Finally, a temperature controller is designed to adjust the temperature of the mixture. The validation of the point of use mixing system at a laboratory tool demonstrates its strengths, especially the huge gain of flexibility in terms of the mixing ratio, outlet flow rates and temperature.

The proposed control concepts enlarge the lab engineer's repertoire to define recipes in order to enable new processes for future wet clean applications. Moreover, the opportunity of controlling the wafer's temperature rises new possibilities to further improve the performance of spin clean tools. One idea is to heat the wafer during the dispense of

chemical solutions onto its surface. This is intended to increase the reactivity of certain chemicals. In order to design model-based estimators and controllers, the proposed mathematical model would have to be extended with the effect of dispensing and spinning off liquids. The liquid flow on the wafer surface clearly impacts the temperature of the wafer. To describe the fluid flow, the so-called transport equation can possibly be applied in cylindrical coordinates. In this case, the overall plant model would then be an interaction of two partial differential equations.

Appendix

Appendix A

Heat transfer equation

The heat transfer equation with heat sources and losses is given as

$$\rho c_p(T)\frac{\partial T(\boldsymbol{\xi},t)}{\partial t} = \mathrm{div}\left\{\lambda_c(T)\mathrm{grad}\left[T(\boldsymbol{\xi},t)\right]\right\} + q(\boldsymbol{\xi},t). \tag{A.1}$$

The term $\mathrm{div}\left\{\lambda_c(T)\mathrm{grad}\left[T(\boldsymbol{\xi},t)\right]\right\}$ can be rearranged as follows:

$$\begin{aligned}
\mathrm{div}\left\{\lambda_c(T)\mathrm{grad}\left[T(\boldsymbol{\xi},t)\right]\right\} &= \mathrm{div}\left\{\lambda_c(T)\begin{bmatrix}\frac{\partial T(\boldsymbol{\xi},t)}{\partial \xi_1}\\ \frac{\partial T(\boldsymbol{\xi},t)}{\partial \xi_2}\\ \frac{\partial T(\boldsymbol{\xi},t)}{\partial \xi_3}\end{bmatrix}\right\} = \mathrm{div}\left\{\begin{bmatrix}\lambda_c(T)\frac{\partial T(\boldsymbol{\xi},t)}{\partial \xi_1}\\ \lambda_c(T)\frac{\partial T(\boldsymbol{\xi},t)}{\partial \xi_2}\\ \lambda_c(T)\frac{\partial T(\boldsymbol{\xi},t)}{\partial \xi_3}\end{bmatrix}\right\}\\
&= \frac{\partial\left[\lambda_c(T)\frac{\partial T(\boldsymbol{\xi},t)}{\partial \xi_1}\right]}{\partial \xi_1} + \frac{\partial\left[\lambda_c(T)\frac{\partial T(\boldsymbol{\xi},t)}{\partial \xi_2}\right]}{\partial \xi_2} + \frac{\partial\left[\lambda_c(T)\frac{\partial T(\boldsymbol{\xi},t)}{\partial \xi_3}\right]}{\partial \xi_3}\\
&= \frac{\partial \lambda_c(T)}{\partial \xi_1}\frac{\partial T(\boldsymbol{\xi},t)}{\partial \xi_1} + \lambda_c(T)\frac{\partial^2 T(\boldsymbol{\xi},t)}{\partial \xi_1^2} + \frac{\partial \lambda_c(T)}{\partial \xi_2}\frac{\partial T(\boldsymbol{\xi},t)}{\partial \xi_2} + \lambda_c(T)\frac{\partial^2 T(\boldsymbol{\xi},t)}{\partial \xi_2^2}\\
&\quad + \frac{\partial \lambda_c(T)}{\partial \xi_3}\frac{\partial T(\boldsymbol{\xi},t)}{\partial \xi_3} + \lambda_c(T)\frac{\partial^2 T(\boldsymbol{\xi},t)}{\partial \xi_3^2}\\
&= \lambda_c(T)\left[\frac{\partial^2 T(\boldsymbol{\xi},t)}{\partial \xi_1^2} + \frac{\partial^2 T(\boldsymbol{\xi},t)}{\partial \xi_2^2} + \frac{\partial^2 T(\boldsymbol{\xi},t)}{\partial \xi_3^2}\right]\\
&\quad + \frac{\partial \lambda_c(T)}{\partial \xi_1}\frac{\partial T(\boldsymbol{\xi},t)}{\partial \xi_1} + \frac{\partial \lambda_c(T)}{\partial \xi_2}\frac{\partial T(\boldsymbol{\xi},t)}{\partial \xi_2} + \frac{\partial \lambda_c(T)}{\partial \xi_3}\frac{\partial T(\boldsymbol{\xi},t)}{\partial \xi_3}\\
&= \lambda_c(T)\mathrm{div}\left\{\mathrm{grad}\left[T(\boldsymbol{\xi},t)\right]\right\} + \frac{\partial \lambda_c(T)}{\partial \xi_1}\frac{\partial \xi_1}{\partial T(\boldsymbol{\xi},t)}\frac{\partial T(\boldsymbol{\xi},t)}{\partial \xi_1}\frac{\partial T(\boldsymbol{\xi},t)}{\partial \xi_1}\\
&\quad + \frac{\partial \lambda_c(T)}{\partial \xi_2}\frac{\partial \xi_2}{\partial T(\boldsymbol{\xi},t)}\frac{\partial T(\boldsymbol{\xi},t)}{\partial \xi_2}\frac{\partial T(\boldsymbol{\xi},t)}{\partial \xi_2} + \frac{\partial \lambda_c(T)}{\partial \xi_3}\frac{\partial \xi_3}{\partial T(\boldsymbol{\xi},t)}\frac{\partial T(\boldsymbol{\xi},t)}{\partial \xi_3}\frac{\partial T(\boldsymbol{\xi},t)}{\partial \xi_3}\\
&= \lambda_c(T)\mathrm{div}\left\{\mathrm{grad}\left[T(\boldsymbol{\xi},t)\right]\right\} + \frac{\partial \lambda_c(T)}{\partial T(\boldsymbol{\xi},t)}\left\{\left[\frac{\partial T(\boldsymbol{\xi},t)}{\partial \xi_1}\right]^2 + \left[\frac{\partial T(\boldsymbol{\xi},t)}{\partial \xi_2}\right]^2 + \left[\frac{\partial T(\boldsymbol{\xi},t)}{\partial \xi_3}\right]^2\right\}\\
&= \lambda_c(T)\mathrm{div}\left\{\mathrm{grad}\left[T(\boldsymbol{\xi},t)\right]\right\} + \frac{\partial \lambda_c(T)}{\partial T(\boldsymbol{\xi},t)}\left\|\mathrm{grad}\left[T(\boldsymbol{\xi},t)\right]\right\|_2^2
\end{aligned} \tag{A.2}$$

Appendix B

Circle-circle intersection

The area S of a circle-circle intersection depicted in Figure B.1 can be calculated as [Weisstein, 2014]

$$
\begin{aligned}
S = {} & r_1^2 \arccos\left(\frac{d^2 + r_1^2 - r_2^2}{2dr_1}\right) + r_2^2 \arccos\left(\frac{d^2 + r_2^2 - r_1^2}{2dr_2}\right) \\
& - \frac{1}{2}\sqrt{(-d + r_1 + r_2)(d + r_1 - r_2)(d - r_1 + r_2)(d + r_1 + r_2)}.
\end{aligned}
\tag{B.1}
$$

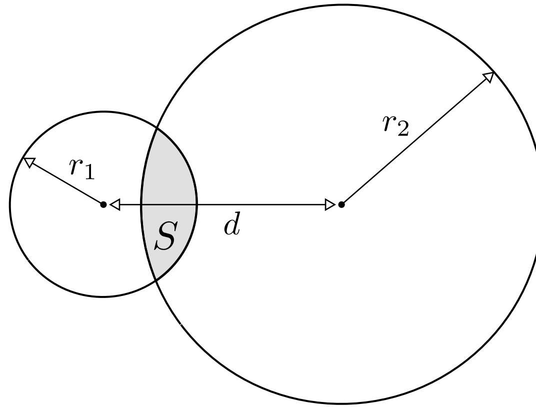

Figure B.1: Circle-circle intersection

Appendix C

Derivative of a matrix-vector-product by a vector

Given a matrix-vector-product dependent on a vector $\boldsymbol{x}$, i.e.

$$\begin{aligned}\boldsymbol{A}(\boldsymbol{x})\boldsymbol{v}(\boldsymbol{x}) &= \begin{bmatrix} a_{11}(\boldsymbol{x}) & a_{12}(\boldsymbol{x}) & \dots & a_{1m}(\boldsymbol{x}) \\ a_{21}(\boldsymbol{x}) & a_{22}(\boldsymbol{x}) & \dots & a_{2m}(\boldsymbol{x}) \\ \vdots & \vdots & & \vdots \\ a_{n1}(\boldsymbol{x}) & a_{n2}(\boldsymbol{x}) & \dots & a_{nm}(\boldsymbol{x}) \end{bmatrix} \begin{bmatrix} v_1(\boldsymbol{x}) \\ v_2(\boldsymbol{x}) \\ \vdots \\ v_m(\boldsymbol{x}) \end{bmatrix} \\ &= \begin{bmatrix} a_{11}(\boldsymbol{x})v_1(\boldsymbol{x}) + a_{12}(\boldsymbol{x})v_2(\boldsymbol{x}) + \ldots + a_{1m}(\boldsymbol{x})v_m(\boldsymbol{x}) \\ a_{21}(\boldsymbol{x})v_1(\boldsymbol{x}) + a_{22}(\boldsymbol{x})v_2(\boldsymbol{x}) + \ldots + a_{2m}(\boldsymbol{x})v_m(\boldsymbol{x}) \\ \vdots \\ a_{n1}(\boldsymbol{x})v_1(\boldsymbol{x}) + a_{n2}(\boldsymbol{x})v_2(\boldsymbol{x}) + \ldots + a_{nm}(\boldsymbol{x})v_m(\boldsymbol{x}) \end{bmatrix}. \end{aligned} \tag{C.1}$$

The derivative of (C.1) with respect to $\boldsymbol{x}$ can be calculated as

$$\begin{aligned} &\frac{\partial[\boldsymbol{A}(\boldsymbol{x})\boldsymbol{v}(\boldsymbol{x})]}{\partial \boldsymbol{x}} = \\ &= \begin{bmatrix} \sum_{\mu=1}^{m} \left[\frac{\partial a_{1\mu}(\boldsymbol{x})}{\partial x_1} v_\mu(\boldsymbol{x}) + a_{1\mu}(\boldsymbol{x})\frac{\partial v_\mu(\boldsymbol{x})}{\partial x_1}\right] & \dots & \sum_{\mu=1}^{m} \left[\frac{\partial a_{1\mu}(\boldsymbol{x})}{\partial x_n} v_\mu(\boldsymbol{x}) + a_{1\mu}(\boldsymbol{x})\frac{\partial v_\mu(\boldsymbol{x})}{\partial x_n}\right] \\ \vdots & & \vdots \\ \sum_{\mu=1}^{m} \left[\frac{\partial a_{n\mu}(\boldsymbol{x})}{\partial x_1} v_\mu(\boldsymbol{x}) + a_{n\mu}(\boldsymbol{x})\frac{\partial v_\mu(\boldsymbol{x})}{\partial x_1}\right] & \dots & \sum_{\mu=1}^{m} \left[\frac{\partial a_{n\mu}(\boldsymbol{x})}{\partial x_n} v_\mu(\boldsymbol{x}) + a_{n\mu}(\boldsymbol{x})\frac{\partial v_\mu(\boldsymbol{x})}{\partial x_n}\right] \end{bmatrix} \\ &= \begin{bmatrix} \sum_{\mu=1}^{m} \frac{\partial a_{1\mu}(\boldsymbol{x})}{\partial x_1} v_\mu(\boldsymbol{x}) & \dots & \sum_{\mu=1}^{m} \frac{\partial a_{1\mu}(\boldsymbol{x})}{\partial x_n} v_\mu(\boldsymbol{x}) \\ \vdots & & \vdots \\ \sum_{\mu=1}^{m} \frac{\partial a_{n\mu}(\boldsymbol{x})}{\partial x_1} v_\mu(\boldsymbol{x}) & \dots & \sum_{\mu=1}^{m} \frac{\partial a_{n\mu}(\boldsymbol{x})}{\partial x_n} v_\mu(\boldsymbol{x}) \end{bmatrix} + \begin{bmatrix} \sum_{\mu=1}^{m} a_{1\mu}(\boldsymbol{x})\frac{\partial v_\mu(\boldsymbol{x})}{\partial x_1} & \dots & \sum_{\mu=1}^{m} a_{1\mu}(\boldsymbol{x})\frac{\partial v_\mu(\boldsymbol{x})}{\partial x_n} \\ \vdots & & \vdots \\ \sum_{\mu=1}^{m} a_{n\mu}(\boldsymbol{x})\frac{\partial v_\mu(\boldsymbol{x})}{\partial x_1} & \dots & \sum_{\mu=1}^{m} a_{n\mu}(\boldsymbol{x})\frac{\partial v_\mu(\boldsymbol{x})}{\partial x_n} \end{bmatrix}. \end{aligned} \tag{C.2}$$

Remark 1: For

$$\boldsymbol{v}(\boldsymbol{x}) = \begin{bmatrix} x_1 \\ x_2 \\ \vdots \\ x_m \end{bmatrix} \tag{C.3}$$

equation (C.2) reduces to

$$\frac{\partial[\boldsymbol{A}(\boldsymbol{x})\boldsymbol{v}(\boldsymbol{x})]}{\partial \boldsymbol{x}} = \begin{bmatrix} \sum_{\mu=1}^{m} \frac{\partial a_{1\mu}(\boldsymbol{x})}{\partial x_1} x_\mu & \dots & \sum_{\mu=1}^{m} \frac{\partial a_{1\mu}(\boldsymbol{x})}{\partial x_n} x_\mu \\ \vdots & & \vdots \\ \sum_{\mu=1}^{m} \frac{\partial a_{n\mu}(\boldsymbol{x})}{\partial x_1} x_\mu & \dots & \sum_{\mu=1}^{m} \frac{\partial a_{n\mu}(\boldsymbol{x})}{\partial x_n} x_\mu \end{bmatrix} + \boldsymbol{A}(\boldsymbol{x}). \tag{C.4}$$

Remark 2: For

$$\boldsymbol{v}(\boldsymbol{x}) = \begin{bmatrix} x_1^4 \\ x_2^4 \\ \vdots \\ x_m^4 \end{bmatrix} \tag{C.5}$$

equation (C.2) reduces to

$$\begin{aligned} \frac{\partial[\boldsymbol{A}(\boldsymbol{x})\boldsymbol{v}(\boldsymbol{x})]}{\partial \boldsymbol{x}} = & \begin{bmatrix} \sum_{\mu=1}^{m} \frac{\partial a_{1\mu}(\boldsymbol{x})}{\partial x_1} x_\mu^4 & \dots & \sum_{\mu=1}^{m} \frac{\partial a_{1\mu}(\boldsymbol{x})}{\partial x_n} x_\mu^4 \\ \vdots & & \vdots \\ \sum_{\mu=1}^{m} \frac{\partial a_{n\mu}(\boldsymbol{x})}{\partial x_1} x_\mu^4 & \dots & \sum_{\mu=1}^{m} \frac{\partial a_{n\mu}(\boldsymbol{x})}{\partial x_n} x_\mu^4 \end{bmatrix} \\ & + \boldsymbol{A}(\boldsymbol{x}) \begin{bmatrix} 4x_1^3 & & & 0 \\ & 4x_2^3 & & \\ & & \ddots & \\ 0 & & & 4x_m^3 \end{bmatrix}. \end{aligned} \tag{C.6}$$

Remark 3: For a constant vector

$$\boldsymbol{v}(\boldsymbol{x}) = \boldsymbol{v} = \begin{bmatrix} v_1 \\ v_2 \\ \vdots \\ v_m \end{bmatrix} \tag{C.7}$$

equation (C.2) reduces to

$$\frac{\partial[\boldsymbol{A}(\boldsymbol{x})\boldsymbol{v}(\boldsymbol{x})]}{\partial\boldsymbol{x}} = \begin{bmatrix} \sum_{\mu=1}^{m} \frac{\partial a_{1\mu}(\boldsymbol{x})}{\partial x_1} v_\mu & \cdots & \sum_{\mu=1}^{m} \frac{\partial a_{1\mu}(\boldsymbol{x})}{\partial x_n} v_\mu \\ \vdots & & \vdots \\ \sum_{\mu=1}^{m} \frac{\partial a_{n\mu}(\boldsymbol{x})}{\partial x_1} v_\mu & \cdots & \sum_{\mu=1}^{m} \frac{\partial a_{n\mu}(\boldsymbol{x})}{\partial x_n} v_\mu \end{bmatrix}. \tag{C.8}$$

Appendix D

Taylor series expansion

Given the nonlinear system

$$\dot{\tilde{\boldsymbol{x}}} = \boldsymbol{f}(\tilde{\boldsymbol{x}}, \boldsymbol{u}) = \begin{bmatrix} \boldsymbol{f}_1(\tilde{\boldsymbol{x}}, \boldsymbol{u}) \\ f_2(\tilde{\boldsymbol{x}}, \boldsymbol{u}) \end{bmatrix} = \left[\begin{array}{c} \boldsymbol{A}_1(\boldsymbol{x})\boldsymbol{x} - \varepsilon \boldsymbol{A}_2(\boldsymbol{x}) \begin{bmatrix} x_1^4 \\ x_2^4 \\ \vdots \\ x_n^4 \end{bmatrix} \\ \hdashline 0 \end{array}\right] + \begin{bmatrix} \boldsymbol{B}(\boldsymbol{x}, \varepsilon) \\ \boldsymbol{0}^T \end{bmatrix} \boldsymbol{u} \tag{D.1}$$

with

$$\tilde{\boldsymbol{x}} = \begin{bmatrix} \boldsymbol{x} \\ \varepsilon \end{bmatrix} \in \mathbb{R}^{n+1}, \;\; \boldsymbol{u} \in \mathbb{R}^m \tag{D.2}$$

and matrices $\boldsymbol{A}_1(\boldsymbol{x})$, $\boldsymbol{A}_2(\boldsymbol{x})$, $\boldsymbol{B}(\boldsymbol{x}, \varepsilon)$ with appropriate dimension. The Taylor series of (D.1) truncated after the linear term calculates as

$$\boldsymbol{f}(\tilde{\boldsymbol{x}}, \boldsymbol{u}) \approx \boldsymbol{f}(\hat{\tilde{\boldsymbol{x}}}, \boldsymbol{u}) + \left. \frac{\partial \boldsymbol{f}(\tilde{\boldsymbol{x}}, \boldsymbol{u})}{\partial \tilde{\boldsymbol{x}}} \right|_{\tilde{\boldsymbol{x}} = \hat{\tilde{\boldsymbol{x}}}} (\tilde{\boldsymbol{x}} - \hat{\tilde{\boldsymbol{x}}}) \tag{D.3}$$

and furthermore

$$\dot{\tilde{\boldsymbol{x}}} \approx \left[\begin{array}{c} \boldsymbol{A}_1(\hat{\boldsymbol{x}})\hat{\boldsymbol{x}} - \hat{\varepsilon} \boldsymbol{A}_2(\hat{\boldsymbol{x}}) \begin{bmatrix} \hat{x}_1^4 \\ \hat{x}_2^4 \\ \vdots \\ \hat{x}_n^4 \end{bmatrix} + \boldsymbol{B}(\hat{\boldsymbol{x}}, \hat{\varepsilon})\boldsymbol{u} \\ \hdashline 0 \end{array}\right] + \left. \left[\begin{array}{c:c} \frac{\partial \boldsymbol{f}_1(\tilde{\boldsymbol{x}}, \boldsymbol{u})}{\partial \boldsymbol{x}} & \frac{\partial \boldsymbol{f}_1(\tilde{\boldsymbol{x}}, \boldsymbol{u})}{\partial \varepsilon} \\ \hdashline \boldsymbol{0}^T & 0 \end{array}\right] \right|_{\tilde{\boldsymbol{x}} = \hat{\tilde{\boldsymbol{x}}}} \begin{bmatrix} \boldsymbol{x} - \hat{\boldsymbol{x}} \\ \varepsilon - \hat{\varepsilon} \end{bmatrix} \tag{D.4}$$

with

$$\frac{\partial \boldsymbol{f}_1(\tilde{\boldsymbol{x}}, \boldsymbol{u})}{\partial \boldsymbol{x}} = \frac{\partial}{\partial \boldsymbol{x}} \boldsymbol{A}_1(\boldsymbol{x})\boldsymbol{x} - \frac{\partial}{\partial \boldsymbol{x}} \varepsilon \boldsymbol{A}_2(\boldsymbol{x}) \begin{bmatrix} x_1^4 \\ x_2^4 \\ \vdots \\ x_n^4 \end{bmatrix} \tag{D.5}$$

and

$$\frac{\partial \boldsymbol{f}_1(\tilde{\boldsymbol{x}}, \boldsymbol{u})}{\partial \varepsilon} = -\frac{\partial}{\partial \varepsilon} \varepsilon \boldsymbol{A}_2(\boldsymbol{x}) \begin{bmatrix} x_1^4 \\ x_2^4 \\ \vdots \\ x_n^4 \end{bmatrix} + \frac{\partial}{\partial \varepsilon} \boldsymbol{B}(\boldsymbol{x}, \varepsilon) \boldsymbol{u}. \tag{D.6}$$

In case the elements of the matrices $\boldsymbol{A}_1(\boldsymbol{x})$, $\boldsymbol{A}_2(\boldsymbol{x})$ and $\boldsymbol{B}(\boldsymbol{x}, \varepsilon)$ differentiated with respect to the elements in $\boldsymbol{x}$ as well as the elements of the matrix $\boldsymbol{B}(\boldsymbol{x}, \varepsilon)$ differentiated with respect to ε are zero, i.e.

- $$\frac{\partial a_{1,\mu\nu}}{\partial x_i} = \frac{\partial a_{2,\mu\nu}}{\partial x_i} = 0, \ \forall \mu, \nu, i \in [1, n], \tag{D.7}$$
- $$\frac{\partial b_{\mu\nu}}{\partial x_i} = \frac{\partial b_{\mu\nu}}{\partial \varepsilon} = 0, \ \forall \mu, i \in [1, n]; \ \nu \in [1, m], \tag{D.8}$$

equations (D.5) and (D.6) reduce according to Appendix C to

$$\frac{\partial \boldsymbol{f}_1(\tilde{\boldsymbol{x}}, \boldsymbol{u})}{\partial \boldsymbol{x}} = \boldsymbol{A}_1(\boldsymbol{x}) - 4\varepsilon \boldsymbol{A}_2(\boldsymbol{x}) \begin{bmatrix} x_1^3 & & & 0 \\ & x_2^3 & & \\ & & \ddots & \\ 0 & & & x_n^3 \end{bmatrix} \tag{D.9}$$

and

$$\frac{\partial \boldsymbol{f}_1(\tilde{\boldsymbol{x}}, \boldsymbol{u})}{\partial \varepsilon} = -\boldsymbol{A}_2(\boldsymbol{x}) \begin{bmatrix} x_1^4 \\ x_2^4 \\ \vdots \\ x_n^4 \end{bmatrix}. \tag{D.10}$$

The linearized system can then be written as

$$= \left[\begin{array}{c} \boldsymbol{A}_1(\hat{\boldsymbol{x}})\hat{\boldsymbol{x}} - \hat{\varepsilon}\boldsymbol{A}_2(\hat{\boldsymbol{x}}) \begin{bmatrix} \hat{x}_1^4 \\ \hat{x}_2^4 \\ \vdots \\ \hat{x}_n^4 \end{bmatrix} + \boldsymbol{B}(\hat{\boldsymbol{x}}, \hat{\varepsilon})\boldsymbol{u} \\ \hdashline 0 \end{array}\right]$$

$$+ \left[\begin{array}{c:c} \boldsymbol{A}_1(\boldsymbol{x}) - 4\varepsilon\boldsymbol{A}_2(\boldsymbol{x}) \begin{bmatrix} x_1^3 & & & 0 \\ & x_2^3 & & \\ & & \ddots & \\ 0 & & & x_n^3 \end{bmatrix} & -\boldsymbol{A}_2(\boldsymbol{x}) \begin{bmatrix} x_1^4 \\ x_2^4 \\ \vdots \\ x_n^4 \end{bmatrix} \\ \hdashline \boldsymbol{0}^T & 0 \end{array}\right]\Bigg|_{\tilde{\boldsymbol{x}}=\hat{\tilde{\boldsymbol{x}}}} \begin{bmatrix} \boldsymbol{x} - \hat{\boldsymbol{x}} \\ \varepsilon - \hat{\varepsilon} \end{bmatrix}$$

$$= \left[\begin{array}{c} \boldsymbol{A}_1(\hat{\boldsymbol{x}})\boldsymbol{x} - 4\hat{\varepsilon}\boldsymbol{A}_2(\hat{\boldsymbol{x}}) \begin{bmatrix} \hat{x}_1^3 & & & 0 \\ & \hat{x}_2^3 & & \\ & & \ddots & \\ 0 & & & \hat{x}_n^3 \end{bmatrix} \boldsymbol{x} + 4\hat{\varepsilon}\boldsymbol{A}_2(\hat{\boldsymbol{x}}) \begin{bmatrix} \hat{x}_1^4 \\ \hat{x}_2^4 \\ \vdots \\ \hat{x}_n^4 \end{bmatrix} - \varepsilon\boldsymbol{A}_2(\hat{\boldsymbol{x}}) \begin{bmatrix} \hat{x}_1^4 \\ \hat{x}_2^4 \\ \vdots \\ \hat{x}_n^4 \end{bmatrix} \\ \hdashline 0 \end{array}\right]$$

$$+ \begin{bmatrix} \boldsymbol{B}(\hat{\boldsymbol{x}}, \hat{\varepsilon}) \\ \boldsymbol{0}^T \end{bmatrix} \boldsymbol{u}$$

$$= \left[\begin{array}{c:c} \boldsymbol{A}_1(\hat{\boldsymbol{x}}) - 4\hat{\varepsilon}\boldsymbol{A}_2(\hat{\boldsymbol{x}}) \begin{bmatrix} \hat{x}_1^3 & & & 0 \\ & \hat{x}_2^3 & & \\ & & \ddots & \\ 0 & & & \hat{x}_n^3 \end{bmatrix} & -\boldsymbol{A}_2(\hat{\boldsymbol{x}}) \begin{bmatrix} \hat{x}_1^4 \\ \hat{x}_2^4 \\ \vdots \\ \hat{x}_n^4 \end{bmatrix} \\ \hdashline \boldsymbol{0}^T & 0 \end{array}\right] \begin{bmatrix} \boldsymbol{x} \\ \varepsilon \end{bmatrix}$$

$$+ \begin{bmatrix} \boldsymbol{B}(\hat{\boldsymbol{x}}, \hat{\varepsilon}) \\ \boldsymbol{0}^T \end{bmatrix} \boldsymbol{u} + \left[\begin{array}{c} 4\hat{\varepsilon}\boldsymbol{A}_2(\hat{\boldsymbol{x}}) \begin{bmatrix} \hat{x}_1^4 \\ \hat{x}_2^4 \\ \vdots \\ \hat{x}_n^4 \end{bmatrix} \\ \hdashline 0 \end{array}\right].$$

Appendix E

Standard deviation of a uniformly distributed random variable

The probability density function of a uniformly distributed random variable x is depicted in Figure E.1.

The mean of x calculates as

$$\begin{aligned} \eta_x &= \int_{-\infty}^{\infty} \alpha f_x(\alpha)\,\mathrm{d}\alpha = \int_a^b \frac{\alpha}{b-a}\,\mathrm{d}\alpha = \left.\frac{\alpha^2}{2(b-a)}\right|_a^b \\ &= \frac{(b^2-a^2)}{2(b-a)} = \frac{(b-a)(b+a)}{2(b-a)} = \frac{(a+b)}{2}. \end{aligned} \tag{E.1}$$

With (E.1), the variance of x can be computed as

$$\begin{aligned} \sigma_x^2 &= \int_{-\infty}^{\infty} (\alpha-\eta_x)^2 f_x(\alpha)\,\mathrm{d}\alpha = \int_a^b \left[\frac{2\alpha-(a+b)}{2}\right]^2 \frac{1}{b-a}\,\mathrm{d}\alpha \\ &= \frac{1}{4(b-a)} \int_a^b \left[4\alpha^2 - 4\alpha(a+b) + (a+b)^2\right]\,\mathrm{d}\alpha \\ &= \frac{1}{4(b-a)} \left.\left[\frac{4\alpha^3}{3} - 2\alpha^2(a+b) + \alpha(a+b)^2\right]\right|_a^b \\ &= \ldots = \frac{1}{4(b-a)}\frac{(b-a)^3}{3} = \frac{(b-a)^2}{12} \end{aligned} \tag{E.2}$$

and accordingly the standard deviation reads as

$$\sigma_x = \frac{(b-a)}{\sqrt{12}}. \tag{E.3}$$

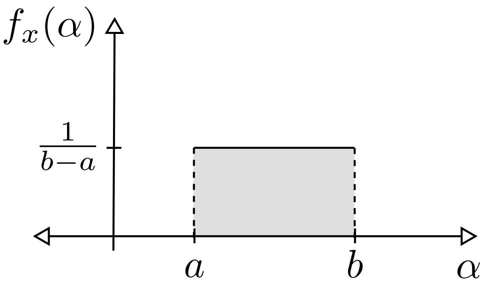

Figure E.1: Uniform distribution

Appendix F

Eigenvalues of linear differential operators

To calculate the eigenvalues of the linear operators introduced in Section 2.5, the method of separation of variables is applied. Therefor, the simplified[1] form of the heat equation in cylindrical coordinates

$$\partial_t T_i(r,t) = \mathcal{A}_i T_i(r,t), \quad i = 1,2 \tag{F.1}$$

with operators

$$\mathcal{A}_i = \partial_{rr} + \frac{1}{r}\partial_r \tag{F.2}$$

and boundary conditions

$$\partial_r T_1(r,t)\Big|_{r=0} = T_1(r,t)\Big|_{r=\zeta} = 0, \tag{F.3a}$$

$$T_2(r,t)\Big|_{r=\zeta} = \partial_r T_2(r,t)\Big|_{r=R} = 0 \tag{F.3b}$$

is considered. Using the ansatz [Cain and Meyer, 2006]

$$T_i(r,t) = v_i(r) w_i(t) \tag{F.4}$$

for (F.1) and skipping the arguments leads to

$$v_i \partial_t w_i = \mathcal{A}_i v_i w_i. \tag{F.5}$$

Dividing equation (F.5) by v_i and w_i results in

$$\frac{\partial_t w_i}{w_i} = \frac{\mathcal{A}_i v_i}{v_i}, \tag{F.6}$$

[1]See (2.9) with $\kappa(T) = 1$ and $q(r,t) = 0$.

where its left-hand side only depends on t and its right-hand side only depends on r. Since t and r vary independent from each other, both sides are equal to some constant value λ, i.e.

$$\frac{\partial_t w_i}{w_i} = \lambda_i \quad \Rightarrow \quad \partial_t w_i = \lambda w_i, \tag{F.7a}$$

$$\frac{\mathcal{A}_i v_i}{v_i} = \lambda_i \quad \Rightarrow \quad \mathcal{A}_i v_i = \lambda v_i. \tag{F.7b}$$

From this it follows that λ_i is the eigenvalue of the differential operator. Furthermore, v_i and w_i are the corresponding eigenfunctions. To calculate the eigenvalues of the operator $\mathcal{A}_i$, equation (F.7b) is evaluated, i.e.

$$\begin{aligned} &\partial_{rr} v_i(r) + \frac{1}{r}\partial_r v_i(r) = \lambda_i v_i(r) \\ &\partial_{rr} v_i(r) + \frac{1}{r}\partial_r v_i(r) - \lambda_i v_i(r) = 0 \\ &r^2 \partial_{rr} v_i(r) + r\partial_r v_i(r) - \lambda_i r^2 v_i(r) = 0. \end{aligned} \tag{F.8}$$

Eigenvalues of the operator $\mathcal{A}_1$: The solution of the ordinary differential equation (F.8) with non-constant coefficients for $i = 1$ depends on the value of λ_1. To show that (F.8) has no nontrivial solutions for $\lambda_1 \geq 0$, three cases are considered in the following.

Case 1 ($\lambda_1 = 0$): For $\lambda_1 = 0$, the differential equation reduces to the so-called Euler equation, which has the general solution

$$v_1(r) = C_1 + C_2 \ln r, \tag{F.9}$$

where C_1, C_2 are arbitrary constants. The derivative of (F.9) with respect to r is given as

$$\partial_r v_1(r) = C_2 \frac{1}{r}. \tag{F.10}$$

Since (F.10) is unbounded at $r = 0$, inserting the first boundary condition of (F.3a) yields $C_2 = 0$. Due to the second boundary condition of (F.3a), also $C_1 = 0$ must hold. Since (F.9) then reduces to the trivial solution, $\lambda_1 = 0$ is not an eigenvalue of $\mathcal{A}_1$.

Case 2 ($\lambda_1 > 0$): In case λ_1 is positive, equation (F.8) is the so-called modified Bessel equation which has the solution

$$v_1(r) = C_1 I_0(\sqrt{\lambda_1} r) + C_2 K_0(\sqrt{\lambda_1} r), \tag{F.11}$$

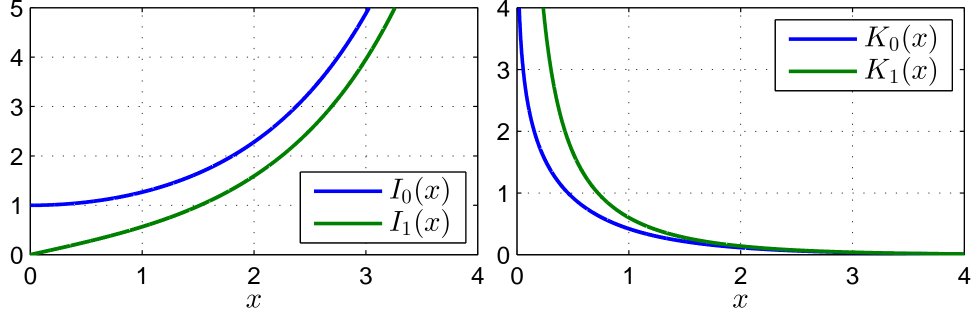

(a) Modified Bessel functions of the first kind for orders 0 and 1

(b) Modified Bessel functions of the second kind for orders 0 and 1

Figure F.1: Modified Bessel functions of the first and second kind

where C_1, C_2 are arbitrary constants and I_0, K_0 are the modified Bessel functions of the first and second kind [Kamke, 1977; Zaitsev and Polyanin, 2002]. Differentiating (F.11) with respect to r yields

$$\partial_r v_1(r) = \sqrt{\lambda_1} C_1 I_1(\sqrt{\lambda_1} r) - \sqrt{\lambda_1} C_2 K_1(\sqrt{\lambda_1} r). \tag{F.12}$$

Since $K_1(\sqrt{\lambda_1} r)$ diverges at $r = 0$ and $I_1(\sqrt{\lambda_1} r)$ vanishes at $r = 0$, the first boundary condition of (F.3a) yields $C_2 = 0$. As Figure F.1a indicates, the modified Bessel function $I_0(\sqrt{\lambda_1} r)$ with $\lambda_1 > 0$ is unequal to zero for $r \neq 0$. Thus, the second boundary condition of (F.3a) points out that also $C_1 = 0$ must hold, which in turn means that $\mathcal{A}_1$ has no positive eigenvalues.

Case 3 ($\lambda_1 < 0$): For $\lambda_1 < 0$, the differential equation (F.8) has the general solution

$$v_1(r) = C_1 J_0(\sqrt{-\lambda_1} r) + C_2 Y_0(\sqrt{-\lambda_1} r), \tag{F.13}$$

where C_1, C_2 are arbitrary constants and I_0, K_0 are the Bessel functions of the first and second kind [Kamke, 1977; Zaitsev and Polyanin, 2002]. The derivative of (F.13) with respect to r is given as

$$\partial_r v_1(r) = -\sqrt{-\lambda_1} C_1 J_1(\sqrt{-\lambda_1} r) - \sqrt{-\lambda_1} C_2 Y_1(\sqrt{-\lambda_1} r). \tag{F.14}$$

Figures F.2a and F.2b depict the Bessel functions of the first and second kind. Figure F.2a points out that $J_1(\sqrt{-\lambda_1} r)$ vanishes for $r = 0$ and Figure F.2b shows a singularity of $Y_1(\sqrt{-\lambda_1} r)$ at $r = 0$. Thus, the first boundary condition of (F.3a) yields $C_2 = 0$. With $C_2 = 0$ and inserting the second boundary condition of (F.3a) into (F.13) leads to

$$v_1(\zeta) = C_1 J_0(\sqrt{-\lambda_1} \zeta) \stackrel{!}{=} 0. \tag{F.15}$$

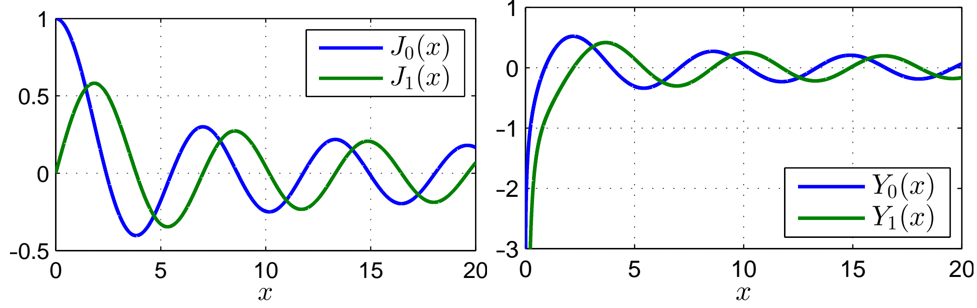

(a) Bessel functions of the first kind for orders 0 and 1 **(b)** Bessel functions of the second kind for orders 0 and 1

Figure F.2: Bessel functions of the first and second kind

The first five positive zeros of the Bessel function of the first kind of order zero are given as 2.4048, 5.5201, 8.6537, 11.7915 and 14.9309. Thus, the maximal eigenvalue of $\mathcal{A}_1$ calculates as

$$\sqrt{-\lambda_{1,max}}\zeta \overset{!}{=} 2.4048$$
$$\lambda_{1,max} = -\left(\frac{2.4048}{\zeta}\right)^2 = -\left(\frac{2.4048}{0.04}\right)^2 = -3614. \tag{F.16}$$

To verify this result, the MATLAB® function `bvp4c` is used, which solves a boundary value problem for ordinary differential equations [Shampine, Gladwell, and Thompson, 2003]. Furthermore, it is possible to involve unknown parameters, i.e. in our case eigenvalues, in the differential equation. Rewriting (F.8) for the first domain and splitting the latter in a set of two first-order differential equations yields

$$\partial_r v_1(r) = \partial_{rr} v_1(r), \tag{F.17a}$$
$$\partial_{rr} v_1(r) = \lambda_1 v_1(r) - \frac{1}{r}\partial_r v_1(r). \tag{F.17b}$$

Due to the usage of cylindrical coordinates, equation (F.17b) shows a singularity at $r = 0$. Extracting the singular term and rewriting (F.17) in matrix notation leads to

$$\begin{bmatrix} \partial_r v_1(r) \\ \partial_{rr} v_1(r) \end{bmatrix} = \frac{1}{r}\begin{bmatrix} 0 & 0 \\ 0 & -1 \end{bmatrix}\begin{bmatrix} v_1(r) \\ \partial_r v_1(r) \end{bmatrix} + \begin{bmatrix} \partial_{rr} v_1(r) \\ \lambda_1 v_1(r) \end{bmatrix} \tag{F.18}$$

The function `bvp4c` requires two functions: one providing the boundary conditions and one implementing the differential equations.

Listing F.1: Matlab functions evaluating the boundary conditions as well as the differential equations disregarding the singularity

```
function res = bcs(ya, yb, lambda)
    res = [ya(2); yb(1); ya(1)-1];
end
function dydx = odes(x, y, lambda)
    dydx = [y(2); lambda*y(1)];
end
```

Note that the function `bcs` needs to return three boundary conditions. Therefor, the third boundary condition is chosen without influencing the eigenvalues as

$$v_1(0) = 1. \tag{F.19}$$

The next step is to provide a structure containing the initial guess for the boundary value solver `bvp4c`. This can be easily handled with the help of the function `bvpinit`, which needs to get an initial mesh on the interval $[0, \zeta]$ as well as an initial guess for the solution. The latter can either be a vector, or as used here, a function, which returns guesses for the solution. The code of the function is given in Listing F.2.

Listing F.2: Matlab function providing guesses for the solution

```
function v = guess(x)
    zeta = 0.04;
    v = [cos(pi/(2*zeta)*x);
        -pi/(2*zeta)*sin(pi/(2*zeta)*x)];
end
```

Please note that the initial guess, i.e.

$$v_{1,guess}(r) = \cos\left(\frac{\pi}{2\zeta} r\right), \tag{F.20}$$

and

$$\partial_r v_{1,guess}(r) = -\frac{\pi}{2\zeta} \sin\left(\frac{\pi}{2\zeta} r\right) \tag{F.21}$$

respectively, is chosen such that it fulfils the three boundary conditions. The problem can then be solved as shown in Listing F.3.

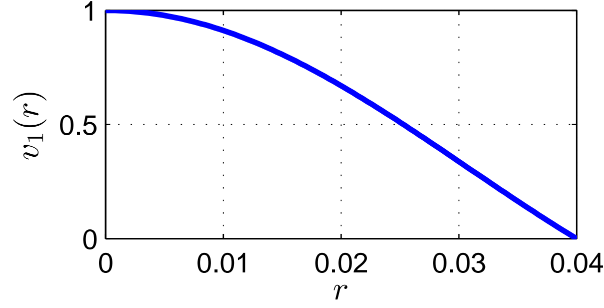

Figure F.3: Eigenvalue calculation of the operator $\mathcal{A}_1$ using the MATLAB® function `bvp4c`, numerical solution

Listing F.3: Matlab code to solve the given boundary problem for the operator $\mathcal{A}_1$ using the function `bvpinit`

```
S = [0 0; 0 -1];
options = bvpset('SingularTerm', S);
zeta = 0.04; % Sensor position
lambda = 0; % Initial guess for the eigenvalue
solinit = bvpinit(linspace(0, zeta, 10), @guess,
   lambda);
sol = bvp4c(@odes, @bcs, solinit, options);
fprintf('Eigenvalue: %f\n', sol.parameters);
```

Executing the MATLAB® script verifies that the eigenvalue approximately equals −3614. The evaluated numerical solution is plotted in Figure F.3, where it is easy to see that the obtained solution fulfils the two boundary conditions.

Eigenvalues of the operator $\mathcal{A}_2$: The calculation of the eigenvalues λ_2 of the operator $\mathcal{A}_2$ defined on the domain (F.3b) is carried out in a similar manner as done for the operator $\mathcal{A}_1$. Applying the method of separation of variables here leads to the ordinary differential spatial equation

$$r^2\partial_{rr}v_2(r) + r\partial_r v_2(r) - \lambda_2 r^2 v_2(r) = 0. \tag{F.22}$$

The solution of (F.22) again depends on the value of λ_2. The case-by-case analysis in the following shows that (F.22) has no nontrivial solutions for $\lambda_2 \geq 0$.

Case 1 ($\lambda_2 = 0$): The general solution of the differential equation for $\lambda_2 = 0$ is

$$v_2(r) = C_1 + C_2 \ln r \tag{F.23}$$

with arbitrary constants C_1 and C_2. Its derivative calculates as

$$\partial_r v_2(r) = C_2 \frac{1}{r}. \tag{F.24}$$

Inserting the second boundary condition of (F.3b), i.e. $\partial_r v_2(R) = 0$, into (F.24) yields $C_2 = 0$. Due to the first boundary condition of (F.3b), also $C_1 = 0$ must hold. Thus, $\lambda_2 = 0$ is not an eigenvalue of $\mathcal{A}_2$.

Case 2 ($\lambda_2 > 0$): In case λ_2 is positive, equation (F.22) has the solution

$$v_2(r) = C_1 I_0(\sqrt{\lambda_2} r) + C_2 K_0(\sqrt{\lambda_2} r) \tag{F.25}$$

with arbitrary constants C_1, C_2 and the modified Bessel functions I_0, K_0. Differentiating (F.25) yields

$$\partial_r v_2(r) = \sqrt{\lambda_2} C_1 I_1(\sqrt{\lambda_2} r) - \sqrt{\lambda_2} C_2 K_1(\sqrt{\lambda_2} r). \tag{F.26}$$

Inserting the second boundary condition of (F.3b) into (F.26) yields

$$C_1 I_1(\sqrt{\lambda_2} R) - C_2 K_1(\sqrt{\lambda_2} R) = 0. \tag{F.27}$$

Since $I_1(\sqrt{\lambda_2} R)$ as well as $K_1(\sqrt{\lambda_2} R)$ are non-negative for positive arguments, it can be concluded that C_1 and C_2 must have the same sign. On the other hand, inserting the first boundary condition of (F.3b) into (F.25) yields

$$C_1 I_0(\sqrt{\lambda_2} \zeta) + C_2 K_0(\sqrt{\lambda_2} \zeta) = 0. \tag{F.28}$$

Again, $I_0(\sqrt{\lambda_2} \zeta)$ as well as $K_0(\sqrt{\lambda_2} \zeta)$ are non-negative for positive arguments, which would now require that C_1 and C_2 have an opposite sign. This is a contradiction to the previous conclusion, meaning that the only solution is the trivial solution, i.e. $C_1 = C_2 = 0$. Thus, $\mathcal{A}_2$ has no positive eigenvalues.

Case 3 ($\lambda_2 < 0$): For $\lambda_2 < 0$, the differential equation (F.22) has the general solution

$$v_2(r) = C_1 J_0(\sqrt{-\lambda_2} r) + C_2 Y_0(\sqrt{-\lambda_2} r) \tag{F.29}$$

with constants C_1, C_2 and Bessel functions I_0, K_0. Its derivative calculates as

$$\partial_r v_2(r) = -\sqrt{-\lambda_2} C_1 J_1(\sqrt{-\lambda_2} r) - \sqrt{-\lambda_2} C_2 Y_1(\sqrt{-\lambda_2} r). \tag{F.30}$$

Inserting the boundary conditions of (F.3b) into (F.29) and (F.30) respectively yields

$$v_2(\zeta) = C_1 J_0(\sqrt{-\lambda_2} \zeta) + C_2 Y_0(\sqrt{-\lambda_2} \zeta) \stackrel{!}{=} 0, \tag{F.31}$$

$$\partial_r v_2(R) = -\sqrt{-\lambda_2} C_1 J_1(\sqrt{-\lambda_2} R) - \sqrt{-\lambda_2} C_2 Y_1(\sqrt{-\lambda_2} R) \stackrel{!}{=} 0. \tag{F.32}$$

We now have three unknowns (C_1, C_2, λ_2), but only two equations. Without loss of generality a third boundary condition can be introduced as[2]

$$v_2(R) = C_1 J_0(\sqrt{-\lambda_2} R) + C_2 Y_0(\sqrt{-\lambda_2} R) \stackrel{!}{=} 1. \tag{F.33}$$

The set of the nonlinear equations composed of (F.31), (F.32) and (F.33) can be easily solved numerically (e.g. with the help of the MATLAB® function `fsolve`). Again, we will find infinitely many solutions. Solving for the maximal value of λ_2 yields

$$\begin{aligned} C_1 &= 0.8405, \\ C_2 &= 1.4669, \\ \lambda_2 &= -118.1668, \end{aligned} \tag{F.34}$$

i.e. the maximal eigenvalue of $\mathcal{A}_2$ is

$$\lambda_{2,max} \approx -118. \tag{F.35}$$

The obtained result can be again verified with the help of the MATLAB® function `bvp4c`. The corresponding source code is given in Listings F.4 and F.5. The initial guess for $v_2(r)$ is again chosen such that it fulfills the boundary conditions, i.e.

$$v_{2,guess}(r) = \sin\left(\frac{\pi}{2(R-\zeta)}(r-\zeta)\right). \tag{F.36}$$

Listing F.4: Matlab code to solve the given boundary problem for the operator $\mathcal{A}_2$ using the function `bvpinit`

```
zeta = 0.04;
R = 0.15;
lambda = 0; % Initial guess for the eigenvalue
solinit = bvpinit(linspace(zeta, R, 10), @guess,
   lambda);
sol = bvp4c(@odes, @bcs, solinit);
fprintf('Eigenvalue: %f\n', sol.parameters);
```

[2]The boundary condition $v_2(R) = 1$ does not influence the zeros of the solution $v_2(r)$.

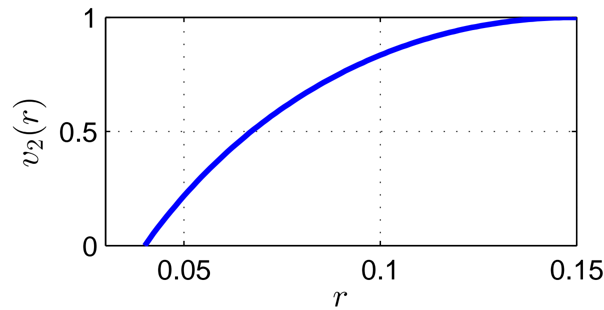

Figure F.4: Eigenvalue calculation of the operator $\mathcal{A}_2$ using the MATLAB® function `bvp4c`, numerical solution

Listing F.5: Matlab functions evaluating the boundary conditions as well as the differential equations and the initial guess

```
function res = bcs(ya, yb, lambda)
    res = [ya(1); yb(2); yb(1)-1];
end
function dydx = odes(x, y, lambda)
    dydx = [y(2); lambda*y(1)-1/x*y(2)];
end
function v = guess(x)
    zeta = 0.04;
    R = 0.15;
    v = [sin(pi/(2*(R-zeta))*(x-zeta));
         pi/(2*(R-zeta))*cos(pi/(2*(R-zeta))
            *(x-zeta))];
end
```

The obtained numerical solution is plotted in Figure F.4, which shows that the boundary conditions are fulfilled.

Appendix G

Controllability inheritance for PI state feedback controller

Given the linear, time-invariant system

$$\begin{aligned} \boldsymbol{x}_{k+1} &= \boldsymbol{\Phi}\boldsymbol{x}_k + \boldsymbol{H}\boldsymbol{u}_k, \\ \boldsymbol{y}_k &= \boldsymbol{C}\boldsymbol{x}_k \end{aligned} \tag{G.1}$$

with $\boldsymbol{u}_k$, $\boldsymbol{y}_k \in \mathbb{R}^m$. Furthermore, the pair ($\boldsymbol{\Phi}$, $\boldsymbol{H}$) is assumed to be controllable. Then, the pair ($\tilde{\boldsymbol{\Phi}}$, $\tilde{\boldsymbol{H}}$) with

$$\tilde{\boldsymbol{\Phi}} = \begin{bmatrix} \boldsymbol{\Phi} & \boldsymbol{0} \\ -\boldsymbol{C} & \boldsymbol{I} \end{bmatrix} \text{ and } \tilde{\boldsymbol{H}} = \begin{bmatrix} \boldsymbol{H} \\ \boldsymbol{0} \end{bmatrix} \tag{G.2}$$

is controllable if $\boldsymbol{\Phi}$ has no eigenvalue at 1 and no component of the transfer function[1] from $\boldsymbol{u}_k$ to $\boldsymbol{y}_k$ given as

$$\begin{aligned} \boldsymbol{G}(z) &= \boldsymbol{C}(z\boldsymbol{I} - \boldsymbol{\Phi})^{-1}\boldsymbol{H} = -\boldsymbol{C}(\boldsymbol{\Phi} - z\boldsymbol{I})^{-1}\boldsymbol{H} \\ &= \begin{bmatrix} G_{11}(z) & G_{12}(z) & \dots & G_{1m}(z) \\ G_{21}(z) & G_{22}(z) & \dots & G_{2m}(z) \\ \vdots & \vdots & \ddots & \vdots \\ G_{m1}(z) & G_{m2}(z) & \dots & G_{mm}(z) \end{bmatrix} \end{aligned} \tag{G.3}$$

has a zero at 1, i.e.

$$\boldsymbol{G}_{ij}(z)|_{z=1} \neq 0, \quad \forall i,j \in [1,m]. \tag{G.4}$$

This can be proved by applying the Hautus criterion to the pair ($\tilde{\boldsymbol{\Phi}}$, $\tilde{\boldsymbol{H}}$), i.e. the latter is controllable if and only if every left eigenvector $\boldsymbol{v}_i^T$ corresponding to the eigenvalue λ_i of $\tilde{\boldsymbol{\Phi}}$ fulfills

$$\boldsymbol{v}_i^T \tilde{\boldsymbol{H}} \neq \boldsymbol{0}^T. \tag{G.5}$$

[1] The discrete-time transfer function from $\boldsymbol{u}_k$ to $\boldsymbol{y}_k$ is given as $\boldsymbol{G}(z) = \frac{\bar{\boldsymbol{y}}(z)}{\bar{\boldsymbol{u}}(z)}$, where $\bar{\boldsymbol{u}}(z)$ and $\bar{\boldsymbol{y}}(z)$ denote the z-transform of $\boldsymbol{u}_k$ and $\boldsymbol{y}_k$.

According to the division of the matrix $\tilde{\boldsymbol{H}}$, the left eigenvector can also be decomposed as

$$\boldsymbol{v}_i^T = \begin{bmatrix} \boldsymbol{v}_{1,i}^T & \boldsymbol{v}_{2,i}^T \end{bmatrix} \tag{G.6}$$

and equation (G.5) can be rewritten as

$$\begin{bmatrix} \boldsymbol{v}_{1,i}^T & \boldsymbol{v}_{2,i}^T \end{bmatrix} \begin{bmatrix} \boldsymbol{H} \\ \boldsymbol{0} \end{bmatrix} = \boldsymbol{v}_{1,i}^T \boldsymbol{H} \neq \boldsymbol{0}^T. \tag{G.7}$$

The eigenvalue equation for calculating $\boldsymbol{v}_i^T$ reads as

$$\begin{bmatrix} \boldsymbol{v}_{1,i}^T & \boldsymbol{v}_{2,i}^T \end{bmatrix} \begin{bmatrix} \boldsymbol{\Phi} & \boldsymbol{0} \\ -\boldsymbol{C} & \boldsymbol{I} \end{bmatrix} = \lambda_i \begin{bmatrix} \boldsymbol{v}_{1,i}^T & \boldsymbol{v}_{2,i}^T \end{bmatrix}. \tag{G.8}$$

Expanding (G.8) yields the two equations

$$\begin{aligned} \underline{\text{I}}: \quad & \boldsymbol{v}_{1,i}^T(\boldsymbol{\Phi} - \lambda_i \boldsymbol{I}) - \boldsymbol{v}_{2,i}^T \boldsymbol{C} = \boldsymbol{0}^T, \\ \underline{\text{II}}: \quad & \boldsymbol{v}_{2,i}^T = \lambda_i \boldsymbol{v}_{2,i}^T. \end{aligned} \tag{G.9}$$

For eigenvalues that are unequal to 1, $\boldsymbol{v}_{2,i}^T$ must be zero due to the second equation of (G.9). The first equation of (G.9) then reduces to the eigenvalue equation with respect to $\boldsymbol{\Phi}$ and due to the controllability of the pair $(\boldsymbol{\Phi}, \boldsymbol{H})$ it can be concluded that equation (G.7) is fulfilled.

The eigenvalues of $\tilde{\boldsymbol{\Phi}}$ that are equal to 1 result from adding integrators. In this case $\boldsymbol{v}_{1,i}^T$ calculates as

$$\boldsymbol{v}_{1,i}^T = \boldsymbol{v}_{2,i}^T \boldsymbol{C}(\boldsymbol{\Phi} - \boldsymbol{I})^{-1}. \tag{G.10}$$

Please note that $\boldsymbol{v}_{2,i}^T$ has to be non-zero, otherwise this would lead to the trivial solution. Furthermore, the inverse of $(\boldsymbol{\Phi} - \boldsymbol{I})$ exists, since $\boldsymbol{\Phi}$ has no eigenvalues equal to 1. Multiplying (G.10) with $\boldsymbol{H}$ from the right side yields

$$\boldsymbol{v}_{1,i}^T \boldsymbol{H} = \boldsymbol{v}_{2,i}^T \boldsymbol{C}(\boldsymbol{\Phi} - \boldsymbol{I})^{-1} \boldsymbol{H} = -\boldsymbol{v}_{2,i}^T \boldsymbol{G}(z)|_{z=1}. \tag{G.11}$$

Since $\boldsymbol{v}_{2,i}^T$ is non-zero and due to assumption (G.4), the right-hand side of (G.11) is unequal to zero. Thus also

$$\boldsymbol{v}_{1,i}^T \boldsymbol{H} = \boldsymbol{v}_i^T \tilde{\boldsymbol{H}} \neq \boldsymbol{0} \tag{G.12}$$

holds and it can be concluded that the pair $(\tilde{\boldsymbol{\Phi}}, \tilde{\boldsymbol{H}})$ is controllable.

Bibliography

Ahmed-Ali, T., F. Giri, and M. Krstic (May 2017). "Observer design for triangular nonlinear systems in the presence of arbitrarily large output delay - a PDE based approach." In: *American Control Conference (ACC)*, pp. 481–486 (cit. on p. 53).

Baehr, H. D. and K. Stephan (2011). *Heat and Mass Transfer*. 3rd. Berlin; Heidelberg: Springer. ISBN: 978-3-642-20020-5 (cit. on p. 10).

Banks, H. T., B. M. Lewis, and H. T. Tran (2007). "Nonlinear feedback controllers and compensators: a state-dependent Riccati equation approach." English. In: *Computational Optimization and Applications* 37.2, pp. 177–218. ISSN: 0926-6003 (cit. on p. 29).

Cain, G. and G. H. Meyer (2006). *Separation of Variables for Partial Differential Equations - An Eigenfunction Approach*. CRC Press (cit. on p. 108).

Ching-An, L. and J. Yaw-Kuen (Jan. 2001). "Control system design for a rapid thermal processing system." In: *Control Systems Technology, IEEE Transactions on* 9.1, pp. 122–129. ISSN: 1063-6536 (cit. on p. 7).

Choi, J. Y., H. M. Do, and H. S. Choi (Nov. 2003). "Adaptive control approach of rapid thermal processing." In: *Semiconductor Manufacturing, IEEE Transactions on* 16.4, pp. 621–632. ISSN: 0894-6507 (cit. on p. 7).

Ebert, J. L. et al. (June 2004). "Model-based control of rapid thermal processing for semiconductor wafers." In: *American Control Conference, 2004. Proceedings of the 2004*. Vol. 5, 3910–3921 vol.5 (cit. on p. 7).

Franklin, G. F., M. L. Workman, and D. Powell (1997). *Digital Control of Dynamic Systems*. 3rd. Boston, MA, USA: Addison-Wesley Longman Publishing Co., Inc. ISBN: 0201820544 (cit. on pp. 32, 33).

Grewal, M. S. and A. P. Andrews (2001). *Kalman Filtering: Theory and Practice with MATLAB*. Second Edition. Wiley Press. ISBN: 0-471-26638-8 (cit. on pp. 38, 40).

Hanus, R., M. Kinnaert, and J.-L. Henrotte (1987). "Conditioning technique, a general anti-windup and bumpless transfer method." In: *Automatica* 23.6, pp. 729–739. ISSN: 0005-1098 (cit. on pp. 65, 67, 69).

Hardy, G., J. E. Littlewood, and G. Pólya (1952). *Inequalities*. Cambridge University Press. ISBN: 9780521358804 (cit. on p. 50).

Hippe, P. (2006). *Windup in Control - Its Effects and Their Prevention*. 1st. London: Springer. ISBN: 978-1-84628-322-2 (cit. on p. 72).

Horn, M. and N. Dourdoumas (2004). *Regelungstechnik: Rechnerunterstuetzter Entwurf zeitkontinuierlicher und zeitdiskreter Regelkreise*. Elektrotechnik: Regelungstechnik. Pearson Studium. ISBN: 9783827372604 (cit. on p. 32).

Jantzen, J. (2013). *Foundations of Fuzzy Control: A Practical Approach*. 2nd. Wiley Publishing. ISBN: 1118506227, 9781118506226 (cit. on p. 85).

Kamke, E. (1977). *Differentialgleichungen: Loesungsmethoden und Loesungen*. Bd. 1. Vieweg+Teubner Verlag. ISBN: 9780828402774 (cit. on p. 110).

Kern, W. (1990). "The Evolution of Silicon Wafer Cleaning Technology." In: *Journal of The Electrochemical Society* 137.6, pp. 1887–1892 (cit. on p. 2).

Kleindienst, M. (2013). "Design of a Model-based Liquid Flow Controller." MA thesis. University of Klagenfurt, Institute of Smart System Technologies (cit. on p. 79).

Lam Research Corporation (2017). *Products* (cit. on pp. 2, 3).

Lin, S. and H.-S. Chu (May 2001). "Thermal uniformity of 12-in silicon wafer in linearly ramped-temperature transient rapid thermal processing." In: *Semiconductor Manufacturing, IEEE Transactions on* 14.2, pp. 143–151. ISSN: 0894-6507 (cit. on p. 7).

Maxwell, J. D., Q. Yan, and J.R. Howell (May 2007). "Full Field Temperature Measurement of Specular Wafers During Rapid Thermal Processing." In: *Semiconductor Manufacturing, IEEE Transactions on* 20.2, pp. 137–142. ISSN: 0894-6507 (cit. on p. 7).

Meurer, T. (July 2013). "On the Extended Luenberger-Type Observer for Semilinear Distributed-Parameter Systems." In: *IEEE Transactions on Automatic Control* 58.7, pp. 1732–1743. ISSN: 0018-9286 (cit. on p. 45).

Miranda, R. et al. (Jan. 2012). "Observer design for a class of hyperbolic PDE equation based on a Distributed Super Twisting Algorithm." In: *12th International Workshop on Variable Structure Systems*, pp. 367–372 (cit. on p. 53).

Patil, S. K. R. et al. (May 2017). "Reduction, reclaim and reuse of sulfuric acid in piranha cleans: GF: Green factory." In: *28th Annual SEMI Advanced Semiconductor Manufacturing Conference (ASMC)*, pp. 376–379 (cit. on p. 5).

Philit, G. et al. (2003). "Advanced Photo Resist Removal using O3 and moist UPW in Semiconductor Production." In: *Cleaning Technology in Semiconductor Device Manufacturing VIII* (cit. on p. 5).

Phillips, C. L. and T. Nagle (2015). *Digital Control System Analysis & Design*. 4th. Pearson. ISBN: 978-0-13-349676-5 (cit. on p. 33).

Reinhardt, K. A. and W. Kern (2008). *Handbook of Silicon Wafer Cleaning Technology (Second Edition)*. Norwich, NY: William Andrew Publishing. ISBN: 978-0-8155-1554-8 (cit. on p. 5).

Sato, T. (1967). "Spectral Emissivity of Silicon." In: *Japanese Journal of Applied Physics* 6.3, p. 339 (cit. on p. 19).

Schaum, A., J. A. Moreno, and J. Alvarez (Dec. 2008). "Spectral dissipativity observer for a class of tubular reactors." In: *47th IEEE Conference on Decision and Control*, pp. 5656–5661 (cit. on p. 53).

Schaum, A., J. A. Moreno, J. Alvarez, and T. Meurer (July 2015). “A simple observer scheme for a class of 1-D semi-linear parabolic distributed parameter systems.” In: *Control Conference (ECC), 2015 European*, pp. 49–54 (cit. on pp. 7, 45, 46).

Schaum, A., J. A. Moreno, E. Fridman, et al. (2014). “Matrix inequality-based observer design for a class of distributed transport-reaction systems.” In: *International Journal of Robust and Nonlinear Control* 24.16, pp. 2213–2230. ISSN: 1099-1239 (cit. on p. 51).

Schaum, A., J. A. Moreno, and T. Meurer (2017). “Observer design for a quasi-linear heat equation” (cit. on p. 47).

Schiesser, W. E. and G. W. Griffiths (2009). *A Compendium of Partial Differential Equation Models: Method of Lines Analysis with Matlab*. New York, NY, USA: Cambridge University Press. ISBN: 0521519861, 9780521519861 (cit. on p. 12).

Schlake, J. C. and U. Konigorski (Aug. 2009). “A new approach to the design of distributed parameter systems based on approximation models.” In: *2009 European Control Conference (ECC)*, pp. 288–293 (cit. on p. 45).

Shampine, L. F., I. Gladwell, and S. Thompson (2003). *Solving ODEs with MATLAB*. Cambridge Books Online. Cambridge University Press. ISBN: 9780511615542 (cit. on p. 111).

Smith, O. J. M. (1959). “A Controller to Overcome Dead Time.” In: *ISA Journal* 6, pp. 28–33 (cit. on p. 91).

Takagi, T. and M. Sugeno (Jan. 1985). “Fuzzy identification of systems and its applications to modeling and control.” In: *IEEE Transactions on Systems, Man, and Cybernetics* SMC-15.1, pp. 116–132. ISSN: 0018-9472 (cit. on p. 85).

Vandenabeele, P. and K. Maex (1991). “Emissivity of silicon wafers during rapid thermal processing.” In: *Proceedings of SPIE* 1393, pp. 316–336 (cit. on p. 19).

Walgama, K. S., S. Ronnback, and J. Sternby (Mar. 1992). “Generalisation of conditioning technique for anti-windup compensators.” In: *IEE Proceedings D - Control Theory and Applications* 139.2, pp. 109–118. ISSN: 0143-7054 (cit. on pp. 67, 69).

Weisstein, E.W. (2014). “Circle-Circle Intersection.” In: *MathWorld - A Wolfram Web Resource* (cit. on p. 99).

Williams, R. S. (Mar. 2017). “What’s Next? [The end of Moore’s law].” In: *Computing in Science Engineering* 19.2, pp. 7–13. ISSN: 1521-9615 (cit. on p. 1).

Zaitsev, V. F. and A. D. Polyanin (2002). *Handbook of Exact Solutions for Ordinary Differential Equations*. CRC Press. ISBN: 9781420035339 (cit. on p. 110).